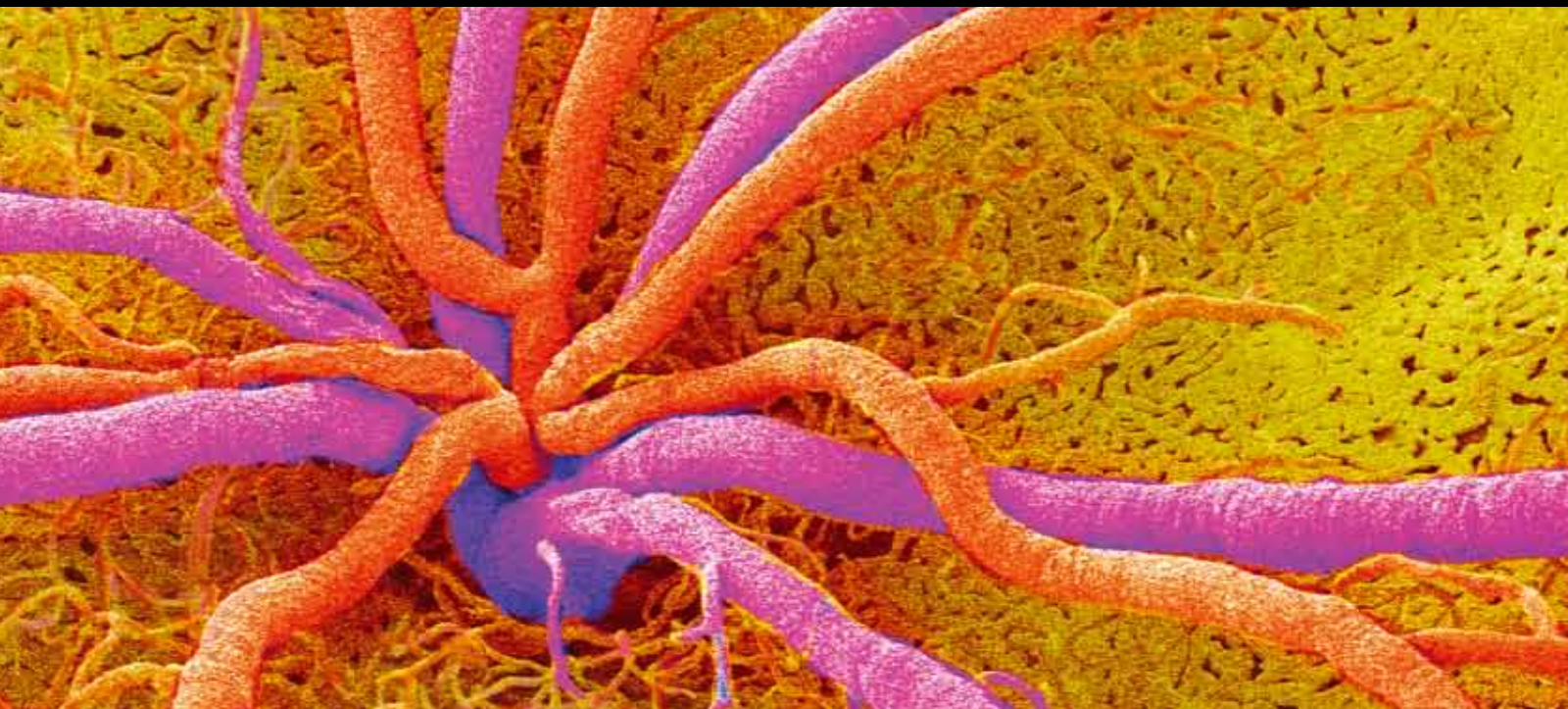


# New Technologies for Glaucoma Imaging

Guest Editors: Christopher K. S. Leung, Felipe A. Medeiros,  
David Garway-Heath, David S. Greenfield, and Robert N. Weinreb





---

# **New Technologies for Glaucoma Imaging**

Journal of Ophthalmology

---

## **New Technologies for Glaucoma Imaging**

Guest Editors: Christopher K. S. Leung, Felipe A. Medeiros,  
David Garway-Heath, David S. Greenfield,  
and Robert N. Weinreb



---

Copyright © 2011 Hindawi Publishing Corporation. All rights reserved.

This is a special issue published in volume 2011 of “Journal of Ophthalmology.” All articles are open access articles distributed under the Creative Commons Attribution License, which permits unrestricted use, distribution, and reproduction in any medium, provided the original work is properly cited.

## Editorial Board

Usha P. Andley, USA  
Susanne Binder, Austria  
Anthony J. Bron, UK  
Chi-Chao Chan, USA  
David K. Coats, USA  
Lucian Del Priore, USA  
Eric Eggenberger, USA  
Michel Eid Farah, Brazil  
Peter J. Francis, USA  
Ian Grierson, UK

Alon Harris, USA  
Pierre Lachapelle, Canada  
Andrew G. Lee, USA  
Christopher Leung, Hong Kong  
Edward Manche, USA  
M. Mochizuki, Japan  
Lawrence S. Morse, USA  
Darius M. Moshfeghi, USA  
Kathy T. Mullen, Canada  
Kristina Narfström, USA

Neville Osborne, UK  
Cynthia Owsley, USA  
Mansoor Sarfarazi, USA  
Naj Sharif, USA  
Torben Lykke Sørensen, Denmark  
G. L. Spaeth, USA  
Denis Wakefield, Australia  
David A. Wilkie, USA  
Terri L. Young, USA

## Contents

**New Technologies for Glaucoma Imaging**, Christopher K. S. Leung, Felipe A. Medeiros, David Garway-Heath, David S. Greenfield, and Robert N. Weinreb  
Volume 2011, Article ID 608975, 2 pages

**Macular Retinal Ganglion Cell Complex Thickness and Its Relationship to the Optic Nerve Head Topography in Glaucomatous Eyes with Hemifield Defects**, Seiji T. Takagi, Yoshiyuki Kita, Asuka Takeyama, and Goji Tomita  
Volume 2011, Article ID 914250, 5 pages

**Measurement of Photoreceptor Layer in Glaucoma: A Spectral-Domain Optical Coherence Tomography Study**, Ning Fan, Nina Huang, Dennis Shun Chiu Lam, and Christopher Kai-shun Leung  
Volume 2011, Article ID 264803, 5 pages

**Comparison of Photopic Negative Response of Full-Field and Focal Electroretinograms in Detecting Glaucomatous Eyes**, Shigeki Machida, Kunifusa Tamada, Taku Oikawa, Yasutaka Gotoh, Tomoharu Nishimura, Muneyoshi Kaneko, and Daijiro Kurosaka  
Volume 2011, Article ID 564131, 11 pages

**Evaluation of Hemodynamic Parameters as Predictors of Glaucoma Progression**, Ingrida Janulevičienė, Rita Ehrlich, Brent Siesky, Irena Nedzelskienė, and Alon Harris  
Volume 2011, Article ID 164320, 9 pages

**Multiphoton Microscopy for Ophthalmic Imaging**, Emily A. Gibson, Omid Masihzadeh, Tim C. Lei, David A. Ammar, and Malik Y. Kahook  
Volume 2011, Article ID 870879, 11 pages

## Editorial

# New Technologies for Glaucoma Imaging

**Christopher K. S. Leung,<sup>1</sup> Felipe A. Medeiros,<sup>2</sup> David Garway-Heath,<sup>3</sup>  
David S. Greenfield,<sup>4</sup> and Robert N. Weinreb<sup>5</sup>**

<sup>1</sup> Department of Ophthalmology and Visual Sciences, The Chinese University of Hong Kong, Kowloon, Hong Kong

<sup>2</sup> Hamilton Glaucoma Center, University of California, San Diego, La Jolla, CA 92093, USA

<sup>3</sup> Moorfields Eye Hospital, London, UK

<sup>4</sup> Bascom Palmer Eye Institute, University of Miami Miller School of Medicine, FL, USA

<sup>5</sup> Shiley Eye Center, University of California, San Diego, La Jolla, CA 92093, USA

Correspondence should be addressed to Robert N. Weinreb, rweinreb@ucsd.edu

Received 8 June 2011; Accepted 8 June 2011

Copyright © 2011 Christopher K. S. Leung et al. This is an open access article distributed under the Creative Commons Attribution License, which permits unrestricted use, distribution, and reproduction in any medium, provided the original work is properly cited.

The evolution of imaging technologies over the past decade has reshaped our landscape in diagnosing and managing patients with glaucoma. Adopting technological advances and translating new information into clinical practice pose new challenges to both clinicians and research scientists. This special issue includes five papers covering some of the recent advances in ocular imaging and electrophysiology technologies and demonstrates how such advancement augments our understanding of glaucoma.

Since its introduction in 2005, the spectral-domain optical coherence tomography (SD-OCT) has received considerable attention for retinal nerve fiber layer (RNFL) and optic disc imaging. With improved axial resolution to discern individual retinal layers, new parameters such as the ganglion cell complex (GCC) and the photoreceptor layer thicknesses can now be measured reliably with SD-OCT. S. T. Takagi and et al. demonstrate that macular GCC thickness could serve as a biomarker for early detection of glaucoma. With a high density of retinal ganglion cells in the macula, it is conceivable that measuring macular GCC thickness would be valuable for glaucoma assessment. By contrast, the outer retina would be expected to be unaffected. Unexpectedly, N. Fan et al. show that the outer nuclear layer is thicker in mild glaucomatous eyes than in normal eyes. This finding suggests glaucomatous damage may involve structural change in the photoreceptors.

Full-field electroretinogram (ERG) has been considered less useful for glaucoma evaluation. S. Machida et al. show that a photopic negative response (PhNR) (a negative deflection following the photopic b-wave) obtained from a focal

ERG system could indicate functional abnormality of retinal ganglion cells and has a high diagnostic performance to detect early glaucoma. While the potential of focal ERG PhNR for objective functional assessment appears promising, prospective longitudinal studies are needed to validate its use in glaucoma patients.

Intraocular pressure (IOP) is a major risk factor for glaucoma progression. Yet, it has long been recognized that there are factors other than IOP that could modify the course of the disease. In a randomized double-masked study comparing dorzolamide/timolol and latanoprost/timolol fixed combination for treatment in glaucoma patients, I. Janulevičienė et al. report that a number of hemodynamic parameters including blood pressure, ocular perfusion pressure, and ophthalmic and central retinal artery vascular resistance are associated with RNFL and/or visual field progression independent of IOP reduction. Although this study is limited by a small sample size (15 patients in each arm) and a high progression rate (40% and 47% of patients progressed, resp.), the result could stimulate more research investigating the roles of ocular and systemic hemodynamics in glaucoma progression.

Multiphoton microscopy is a relatively new modality for ophthalmic imaging. E. A. Gibson et al. summarize the applications of multiphoton microscopy for retinal and transscleral imaging and demonstrate the feasibility to visualize the collagen fibers in human trabecular meshwork *ex vivo*. The exciting development of multiphoton imaging will undoubtedly provide new data for potential application in the clinic in the near future.

The improvement in patient care depends upon continued research and development of new tools and new techniques to unfold the pathobiology of glaucoma for early diagnosis and treatment. It is sufficient to say that glaucoma imaging forms one of the cornerstones in the advancement of glaucoma care.

*Christopher K. S. Leung  
Felipe A. Medeiros  
David Garway-Heath  
David S. Greenfield  
Robert N. Weinreb*

## Clinical Study

# Macular Retinal Ganglion Cell Complex Thickness and Its Relationship to the Optic Nerve Head Topography in Glaucomatous Eyes with Hemifield Defects

Seiji T. Takagi, Yoshiyuki Kita, Asuka Takeyama, and Goji Tomita

Department of Ophthalmology, Ohashi Medical Center, Toho University, 2-17-6 Ohashi, Meguro-ku, Tokyo 153-8515, Japan

Correspondence should be addressed to Goji Tomita, gtom-gif@umin.ac.jp

Received 4 June 2010; Revised 12 August 2010; Accepted 15 October 2010

Academic Editor: Christopher Leung

Copyright © 2011 Seiji T. Takagi et al. This is an open access article distributed under the Creative Commons Attribution License, which permits unrestricted use, distribution, and reproduction in any medium, provided the original work is properly cited.

**Purpose.** To evaluate the relationship between the macular ganglion cell complex (mGCC) thickness, which is the sum of the retinal nerve fiber, ganglion cell, and inner plexiform layers, measured with a spectral-domain optical coherence tomograph and the optic nerve head topography measured with a confocal scanning laser ophthalmoscope in glaucomatous eyes with visual field defects localized predominantly to either hemifield. **Materials and Methods.** The correlation between the mGCC thickness in hemispheres corresponding to hemifields with and without defects (damaged and intact hemispheres, respectively) and the optic nerve head topography corresponding to the respective hemispheres was evaluated in 18 glaucomatous eyes. **Results.** The mGCC thickness was significantly correlated with the rim volume, mean retinal nerve fiber layer thickness, and cross-sectional area of the retinal nerve fiber layer in both the intact and the damaged hemispheres ( $P < .05$ ). **Discussion.** For detecting very early glaucomatous damage of the optic nerve, changes in the thicknesses of the inner retina in the macular area and peripapillary RNFL as well as rim volume changes in the optic nerve head are target parameters that should be carefully monitored.

## 1. Introduction

The macular thickness is reduced in glaucomatous eyes compared with normal eyes [1–3]. This reduction is attributable mainly to the loss of retinal ganglion cells and retinal nerve fibers [3–5]. Using a newly developed software for automatic measurements of macular ganglion cell complex (mGCC) thickness, which is the sum of the thicknesses of the retinal nerve fiber, ganglion cell, and inner plexiform layers, Tan et al. demonstrated that automatic mGCC measurements with a spectral-domain optical coherence tomograph (SD-OCT) have better diagnostic accuracy and repeatability than macular retinal thickness measurements with a time-domain (TD) OCT [6]. On the other hand, topographic measurements of the optic nerve head with a confocal scanning laser ophthalmoscope (CSLO) have demonstrated a high correlation with clinical estimates of the optic nerve by expert assessment at an independent reading center after correcting for the optic disc size [7]. Nowadays, a CSLO is the standard tool to evaluate the optic nerve head topography. However,

the relationship between macular structural changes and topographic changes in the optic nerve head in glaucoma is not clear. For combined application of mGCC thickness and optic nerve head topographic measurements to detect glaucoma, the correlation between the optic nerve head topography and the mGCC thickness should be clarified.

In this study, we aimed to elucidate the relationship between the mGCC thickness measured with an automatic measurement algorithm of an SD-OCT and the optic nerve head topography measured with a CSLO in glaucomatous eyes with hemifield defects.

## 2. Subjects and Methods

**2.1. Subjects and Examinations.** Participants were recruited at the Department of Ophthalmology, Toho University Ohashi Medical Center, Tokyo, Japan. The Toho University Ohashi Medical Center Institutional Review Board approved all protocols, and the study adhered to the tenets of the Declaration of Helsinki. The study protocols were thoroughly

explained to all participants and their written informed consent was obtained.

All subjects underwent complete ophthalmologic examination, including assessment of medical and family history, visual acuity testing with refraction, slit-lamp biomicroscopy including gonioscopy, intraocular pressure (IOP) measurement with Goldmann applanation tonometry, and dilated stereoscopic fundus examination. Their visual field sensitivity was tested by using Humphrey field analyzer (model 750i, Carl Zeiss Meditec, Inc., Dublin, CA) 30-2 with Swedish interactive threshold algorithm (SITA) standard automated perimetry (SAP). All subjects underwent the Humphrey visual field (HVF), OCT, and CSLO tests within a 3-month time window.

**2.2. Inclusion and Exclusion Criteria.** The inclusion criteria were as follows: normal open anterior chamber angles on slit-lamp biomicroscopic and gonioscopic examinations of both eyes; glaucomatous optic nerve head appearance on stereoscopic evaluation (i.e., focal or generalized narrowing or disappearance of the neuroretinal rim with a vertical cup-to-disc area ratio of  $>0.7$  or retinal nerve fiber layer [RNFL] defects indicating glaucoma) and corresponding visual field abnormalities in either the superior or the inferior hemifield exclusively by repeatable SAP results; and best-corrected visual acuity of  $\geq 15/20$  with no media opacities, refractive errors in the spherical equivalent not exceeding  $-6$  or  $+3$  diopters, and cylindrical correction within 3.0 diopters.

In addition, the subjects had to be familiar with SAP testing from at least two previous visual field examinations and have a reliable HVF with SITA 30-2 standard tests (fixation loss  $<20\%$ , false-positive and false-negative rates  $<33\%$ ). They were also required to have at least one eye meeting the following criteria for hemifield defects: a cluster of three or more contiguous points in the pattern deviation plot of the HVF with a probability of  $<5\%$  in either the superior or the inferior hemifield, with at least one point having a probability level of  $<1\%$ ; the opposite hemifield not having a point with a probability level equal to or worse than  $2\%$ , or a cluster of three or more contiguous points with a probability of  $<5\%$ ; glaucoma hemifield test results outside the normal limits.

The exclusion criteria were a history of intraocular surgery, presence of other intraocular eye diseases or other diseases affecting the visual fields (e.g., pituitary lesions, demyelinating diseases, diabetic retinopathy), and treatment with medications known to affect visual field sensitivity. If both eyes met all the criteria, one eye was randomly selected.

**2.3. Measurements of mGCC Thickness.** The selected eyes were scanned by using RTVue-100 (Optovue, Inc., Fremont, CA) with software version 2.0.4.0, which uses a scanning laser diode to emit a scan beam with a wavelength of  $840 \pm 10$  nm to provide images of ocular microstructures. In this study, the GCC scanning protocol was used for the mGCC thickness measurements. The GCC protocol is a  $7 \text{ mm} \times 7 \text{ mm}$  raster scan composed of one horizontal B scan with 800 A scans, and 17 vertical B scans with 934 A scans. The mean GCC thickness of the superior and

inferior hemispheres was calculated. A well-trained operator obtained good-quality OCT images with pupillary dilation. The criteria for determining scan quality were signal strength of at least 50 or more (as suggested by the manufacturer), a clear fundus image allowing a foveal pit, even and dense color saturation throughout all retinal layers with red color visible in the retinal pigment epithelium without interruptions, and a continuous scan pattern without missing or blank areas.

**2.4. Optic Nerve Head Measurements.** The parameters of the optic nerve head topography were measured with Heidelberg Retina Tomograph II (HRT-II, software version 3.1.2.4; Heidelberg Engineering GmbH, Heidelberg, Germany) [8–10]. HRT-II uses a diode laser (670-nm wavelength) to scan the retinal surface sequentially in the horizontal and vertical directions at multiple focal planes. By using confocal scanning principles, a three-dimensional topographic image is constructed from a series of optical image sections at consecutive focal planes. The topographic image determined from the acquired three-dimensional image consists of  $384 \times 384$  (147,456) pixels, each of which is a measure of the retinal height at its corresponding location. For every subject in this study, images were obtained through dilated pupils with a 15-degree field of view.

Three topographic images were obtained, combined, and automatically aligned to create a single mean topographic image for analysis. A contour line of the optic disc margin was drawn around the inner margin of the peripapillary scleral ring by a well-trained operator, while viewing non-stereo color fundus photographs. The contour line was reviewed in the topographic and reflectance images and the height profile graph included in the instrument by the same operator. Twelve HRT-II parameters were analyzed: disc area, cup area, rim area, cup-to-disc area ratio, cup volume, rim volume, mean cup depth, maximum cup depth, height variation contour, cup shape measure, mean RNFL thickness, and RNFL cross-sectional area. Magnification errors were corrected by using the subjective refractive status and corneal curvature measurements. The analysis was restricted to the eyes that had valid optic disc measurements with HRT-II. Good image quality was defined by appropriate focus, brightness, and clarity; minimal eye movement; optic disc centered in the image; a standard deviation (SD) of the mean topographic image less than  $50 \mu\text{m}$ . The eyes for which good-quality images could not be obtained were excluded from the analysis.

**2.5. Statistical Analysis.** The correlation between the mGCC thickness measurements in the hemispheres corresponding to the hemifields with and without visual field defects (damaged and intact hemispheres, resp.) and the HRT-II parameters corresponding to the respective hemispheres (90 degrees superior or inferior to the optic nerve head topography) was evaluated. For example, when an eye had superior hemifield defects, the inferior hemisphere was the damaged hemisphere and the superior hemisphere was the intact hemisphere. In this case, the damaged hemisphere comprised 90 degrees in the inferior optic nerve head

TABLE 1: Background data of the patients ( $n = 18$ ).

Male/female	8/10
Age (years)	$53.6 \pm 14.6$
Refraction (diopters)*	$-3.75 \pm 3.56$
Intraocular pressure (mmHg)	$14.4 \pm 1.8$
Humphrey visual field	
Mean deviation (dB)	$-6.57 \pm 3.91$
Pattern standard deviation (dB)	$9.35 \pm 3.80$
Mean of the total deviation (dB)	
Hemifield corresponding to the damaged hemisphere	$-10.94 \pm 7.24$
Hemifield corresponding to the intact hemisphere	$-2.70 \pm 2.64$
Mean of the pattern deviation (dB)	
Hemifield corresponding to the damaged hemisphere	$-10.41 \pm 6.45$
Hemifield corresponding to the intact hemisphere	$-2.30 \pm 1.96$

Values are expressed as the mean + SD. \*: spherical equivalents.

TABLE 2: The mGCC thickness and HRT-II parameters of the intact and damaged hemispheres.

Parameters	Damaged hemisphere	Intact hemisphere	<i>P</i>
Macular area			
mGCC ( $\mu\text{m}$ )	$75.67 \pm 10.16$	$85.11 \pm 10.03$	.005
HRT-II parameters			
Disc area ( $\text{mm}^2$ )	$0.53 \pm 0.13$	$0.54 \pm 0.11$	.329
Cup area ( $\text{mm}^2$ )	$0.29 \pm 0.14$	$0.25 \pm 0.12$	.205
Rim area ( $\text{mm}^2$ )	$0.22 \pm 0.09$	$0.27 \pm 0.12$	.058
Cup area/disc area	$0.59 \pm 0.17$	$0.46 \pm 0.22$	.032
Cup volume ( $\text{mm}^3$ )	$0.09 \pm 0.07$	$0.08 \pm 0.08$	.254
Rim volume ( $\text{mm}^3$ )	$0.05 \pm 0.03$	$0.08 \pm 0.05$	.009
Mean cup depth (mm)	$0.34 \pm 0.15$	$0.38 \pm 0.20$	.211
Maximum cup depth (mm)	$0.66 \pm 0.19$	$0.79 \pm 0.46$	.153
Height variation contour (mm)	$0.34 \pm 0.14$	$0.26 \pm 0.11$	.068
Cup shape measure	$0.04 \pm 0.08$	$0.04 \pm 0.15$	.811
Mean RNFL thickness (mm)	$0.18 \pm 0.10$	$0.31 \pm 0.17$	.012
RNFL cross-sectional area ( $\text{mm}^2$ )	$0.21 \pm 0.19$	$0.40 \pm 0.22$	.005

Values are expressed as the mean + SD; *P* values by paired *t*-test ( $n = 18$ ). mGCC = macular ganglion cell complex, HRT-II = Heidelberg Retina Tomograph II, RNFL = retinal nerve fiber layer.

topography and the intact hemisphere was 90 degrees in the superior optic nerve head topography.

Statistical analyses were performed by using SPSS version 17.0 (SPSS, Inc., Chicago, IL). Data are presented as the mean  $\pm$  SD. The two-tailed paired *t*-test was performed to evaluate the difference in the parameters between the damaged and the intact hemispheres. When the mean difference (mean of the difference between individual eyes) is 10 and its SD is 10, or the mean difference is 0.1 and the SD is 0.1, 18 subjects provide 99% power with alpha = 0.05, two tails, in the paired *t*-test. Linear regression analysis and Pearson's correlation coefficients (*R*) were used to assess the relationship between the OCT and the HRT-II parameters. A correlation coefficient of 0.55 has 80% power with alpha = 0.05, with 18 subjects (Fisher Z approximation). A *P* value of  $< .05$  was considered statistically significant.

### 3. Results

In total, 18 eyes with primary open-angle glaucoma (superior hemifield defects: 13 eyes; inferior hemifield defects: five eyes) were studied (Table 1).

The mGCC thickness in the damaged hemisphere was significantly thinner than that in the intact hemisphere (Table 2). The cup-to-rim area ratio, rim volume, mean RNFL thickness, and RNFL cross-sectional area in the damaged hemisphere were also significantly worse than that in the intact hemisphere (Table 2).

The mGCC thickness was significantly correlated with the cup-to-disc area ratio, rim area, rim volume, mean RNFL thickness, and RNFL cross-section area in the damaged hemisphere. In the intact hemisphere, the mGCC thickness was significantly correlated with the rim volume, mean RNFL thickness, and RNFL cross-sectional area (Table 3).

TABLE 3: Correlations between the mGCC thickness and the HRT-II parameters.

HRT-II parameters	Damaged hemisphere		Intact hemisphere	
	<i>R</i>	<i>P</i>	<i>R</i>	<i>P</i>
Disc area	0.15	.561	0.22	.378
Cup area	-0.35	.152	0.003	.990
Rim area	0.58	.013	0.24	.343
Cup area/disc area	-0.56	.013	-0.13	.622
Cup volume	-0.20	.450	0.05	.857
Rim volume	0.64	.004	0.54	.021
Mean cup depth	-0.10	.683	0.26	.294
Maximum cup depth	0.08	.745	0.25	.310
Height variation contour	-0.11	.349	-0.14	.593
Cup shape measure	-0.35	.126	0.16	.520
Mean RNFL thickness	0.58	.012	0.66	.003
RNFL cross-sectional area	0.57	.014	0.70	.001

mGCC = macular ganglion cell complex, HRT-II = Heidelberg Retina Tomograph II, RNFL = retinal nerve fiber layer,  $n = 18$ .

#### 4. Discussion

In this study, after measuring the mGCC thickness by using an SD-OCT and the topographic parameters of the optic nerve head by using a CSLO in glaucomatous eyes with hemifield-localized visual field loss, we found that the mGCC thickness is correlated with the rim volume, mean RNFL thickness, and RNFL cross-sectional area even in the intact hemisphere corresponding to the hemifield without apparent visual field defects.

There are reports of diffuse RNFL damage in eyes with localized visual field abnormalities [11–15]. Grewall et al. reported that the HRT-derived cup-to-disc area ratio is significantly correlated with the mean RNFL thickness in a normal hemifield measured by using an SD-OCT [16]. However, knowledge on the structural changes in the macular area of glaucomatous eyes and their correlation with the optic nerve head topography in a normal visual hemifield is still limited. We found that the diffuse structural damage observed in glaucoma also includes the macular area, particularly the inner retinal structure (GCC thickness). Our observation of the correlation between the mGCC thickness and the RNFL-related HRT-II parameters in the intact hemisphere is reasonable because the mGCC thickness can be considered to represent damage mainly of the ganglion cells and their axons.

In our study, the cup area-to-disc area ratio and rim area were correlated with the mGCC thickness in the damaged hemisphere but not in the intact hemisphere. The reason for this discrepancy is not clear. Considering the significant correlation in the rim volume in the damaged and intact hemispheres, a three-dimensional parameter such as volume might provide more precise information on ganglion cell damage than a two-dimensional parameter such as area does. Another possible explanation is the influence of the size of the optic nerve head on the cup area-to-disc area ratio. As the cup area is significantly correlated with the size of the optic nerve head, a difference in this size between the damaged

and the intact hemispheres could influence the measurement of the cup area. However, in the present study, there was no significant difference in the size of the optic nerve head between the hemispheres.

Regarding the reproducibility of the mGCC thickness measurements, Tan et al. showed good reproducibility by using RTVue [6]. However, our study has several limitations. First, the sample size is small; therefore, although a correlation coefficient of 0.55 has 80% power ( $\alpha = 0.05$ ) with 18 subjects, a significant correlation between parameters with a smaller correlation coefficient can be detected with a larger sample. Second, we used only 90 degrees superior and inferior in the optic nerve head topographic measurements; this may underrepresent the changes seen in the mGCC thickness. However, in the GCC scanning protocol of the RTVue, to cover the peripheral areas most affected by glaucoma, the center of the GCC map is placed at 1 mm temporal to the foveal center for better coverage of the temporal region. Therefore, the mGCC thickness seems to reflect the thickness of the peripapillary RNFL located in the more superior or inferior portion of the optic nerve head rather than just the temporal region. The relationship of the temporal topographic parameters of the optic nerve head with the mGCC thickness should be analyzed by another study. Third, correction for ocular magnification due to refraction, axial length, and camera parameters is unavailable in the current RTVue system, although HRT corrects its magnification errors before analysis. Therefore, in our study, the scanning area for the mGCC thickness measurements might have been affected by refractive errors or axial length of the eye. Recently, Kang et al. reported that after adjusting ocular magnification, the average peripapillary RNFL thickness measured by an SD-OCT has no correlation with the spherical equivalent and only a weak positive correlation with axial length [16]. It is still not clear whether mGCC thickness measurements are influenced by ocular magnification or not. Further study to investigate ocular magnification effects on mGCC measurements is needed.

In conclusion, of the 12 HRT-II parameters assessed in glaucomatous eyes with visual field defects restricted to hemifields, most were not significantly associated with the mGCC thickness. Of the three parameters that showed significant correlations in both the damaged and the intact hemispheres, two are related to the RNFL thickness and only one is an actual topographical measurement of the optic nerve head. Particularly in the intact hemisphere, the mGCC thickness is significantly correlated with the RNFL-related HRT parameters. For detecting very early glaucomatous damage of the optic nerve, changes in the thicknesses of the inner retina in the macular area and peripapillary RNFL as well as rim volume changes in the optic nerve head are target parameters that should be carefully monitored.

## Acknowledgment

This study was supported in part by Grant-in-Aid for Scientific Research (C) 21592247 from the Ministry of Education, Culture, Sports, and Technology of Japan.

## References

- [1] M. Tanito, N. Itai, A. Ohira, and E. Chihara, "Reduction of posterior pole retinal thickness in glaucoma detected using the Retinal Thickness Analyzer," *Ophthalmology*, vol. 111, no. 2, pp. 265–275, 2004.
- [2] D. S. Greenfield, H. Bagga, and R. W. Knighton, "Macular thickness changes in glaucomatous optic neuropathy detected using optical coherence tomography," *Archives of Ophthalmology*, vol. 121, no. 1, pp. 41–46, 2003.
- [3] C. K. S. Leung, W.-M. Chan, W.-H. Yung et al., "Comparison of macular and peripapillary measurements for the detection of glaucoma: an optical coherence tomography study," *Ophthalmology*, vol. 112, no. 3, pp. 391–400, 2005.
- [4] Y. Glovinsky, H. A. Quigley, and M. E. Pease, "Foveal ganglion cell loss is size dependent in experimental glaucoma," *Investigative Ophthalmology and Visual Science*, vol. 34, no. 2, pp. 395–400, 1993.
- [5] L. J. Frishman, F. F. Shen, L. Du et al., "The scotopic electroretinogram of macaque after retinal ganglion cell loss from experimental glaucoma," *Investigative Ophthalmology and Visual Science*, vol. 37, no. 1, pp. 125–141, 1996.
- [6] O. Tan, V. Chopra, A. T.-H. Lu et al., "Detection of macular ganglion cell loss in glaucoma by Fourier-domain optical coherence tomography," *Ophthalmology*, vol. 116, no. 12, pp. 2305–2314, 2009.
- [7] L. M. Zangwill, R. N. Weinreb, C. C. Berry et al., "The confocal scanning laser ophthalmoscopy ancillary study to the ocular hypertension treatment study: study design and baseline factors," *American Journal of Ophthalmology*, vol. 137, no. 2, pp. 219–227, 2004.
- [8] S. A. Vernon, M. J. Hawker, G. Ainsworth, J. G. Hillman, H. K. MacNab, and H. S. Dua, "Laser scanning tomography of the optic nerve head in a normal elderly population: the Bridlington eye assessment project," *Investigative Ophthalmology and Visual Science*, vol. 46, no. 8, pp. 2823–2828, 2005.
- [9] C. A. Girkin, G. McGwin Jr., S. F. McNeal, and J. DeLeon-Ortega, "Racial differences in the association between optic disc topography and early glaucoma," *Investigative Ophthalmology and Visual Science*, vol. 44, no. 8, pp. 3382–3387, 2003.
- [10] F. A. Medeiros, L. M. Zangwill, C. Bowd, and R. N. Weinreb, "Comparison of the GDx VCC scanning laser polarimeter, HRT II confocal scanning laser ophthalmoscope, and stratus OCT optical coherence tomograph for the detection of glaucoma," *Archives of Ophthalmology*, vol. 122, no. 6, pp. 827–837, 2004.
- [11] C. Matsumoto, S. Shirato, M. Haneda, H. Yamashiro, and M. Saito, "Study of retinal nerve fiber layer thickness within normal hemivisual field in primary open-angle glaucoma and normal-tension glaucoma," *Japanese Journal of Ophthalmology*, vol. 47, no. 1, pp. 22–27, 2003.
- [12] M. S. Kook, K.-R. Sung, S. Kim, R. Park, and W. Kang, "Study of retinal nerve fibre layer thickness in eyes with high tension glaucoma and hemifield defect," *British Journal of Ophthalmology*, vol. 85, no. 10, pp. 1167–1170, 2001.
- [13] R. D. C. Reyes, G. Tomita, and Y. Kitazawa, "Retinal nerve fiber layer thickness within the area of apparently normal visual field in normal-tension glaucoma with hemifield defect," *Journal of Glaucoma*, vol. 7, no. 5, pp. 329–335, 1998.
- [14] H. Bagga and D. S. Greenfield, "Quantitative assessment of structural damage in eyes with localized visual field abnormalities," *American Journal of Ophthalmology*, vol. 137, no. 5, pp. 797–805, 2004.
- [15] H. Bagga, D. S. Greenfield, and R. W. Knighton, "Macular symmetry testing for glaucoma detection," *Journal of Glaucoma*, vol. 14, no. 5, pp. 358–363, 2005.
- [16] D. S. Grewal, M. Sehi, and D. S. Greenfield, "Diffuse glaucomatous structural and functional damage in the hemifield without significant pattern loss," *Archives of ophthalmology*, vol. 127, no. 11, pp. 1442–1448, 2009.

## Clinical Study

# Measurement of Photoreceptor Layer in Glaucoma: A Spectral-Domain Optical Coherence Tomography Study

Ning Fan,<sup>1,2</sup> Nina Huang,<sup>2</sup> Dennis Shun Chiu Lam,<sup>1</sup> and Christopher Kai-shun Leung<sup>1</sup>

<sup>1</sup>Department of Ophthalmology and Visual Sciences, Hong Kong Eye Hospital, The Chinese University of Hong Kong, 147K Argyle Street, Kowloon, Hong Kong

<sup>2</sup>Shenzhen Eye Hospital, Jinan University, Shenzhen 518001, China

Correspondence should be addressed to Christopher Kai-shun Leung, cksleung@cuhk.edu.hk

Received 7 March 2011; Accepted 29 April 2011

Academic Editor: R. N. Weinreb

Copyright © 2011 Ning Fan et al. This is an open access article distributed under the Creative Commons Attribution License, which permits unrestricted use, distribution, and reproduction in any medium, provided the original work is properly cited.

**Objective.** To measure and compare photoreceptor layer thickness between normal and glaucomatous eyes using spectral-domain optical coherence tomography (OCT). **Methods.** Thirty-eight healthy normal volunteers and 47 glaucoma patients were included in the analysis. One eye from each participant was randomly selected for macula imaging by a spectral-domain OCT (3D OCT-1000, Topcon, Tokyo, Japan). The foveal and parafoveal (1.5 mm from the fovea) outer nuclear layer (ONL) and inner and outer segments (IS+OS) layer thicknesses were measured by a single masked observer. The measurements were repeated 3 times in a random sample of 30 normal eyes to determine the repeatability coefficient and intraclass correlation coefficient. **Results.** The measurement variabilities of photoreceptor thickness were low. The respective intraclass correlation coefficients of ONL and IS+OS thicknesses were 0.96 (95% confidence interval: 0.94–0.98) and 0.82 (95% confidence interval 0.70–0.90). While there were no differences in parafoveal ONL and IS+OS thicknesses between normal and glaucoma groups ( $P \leq .410$ ), the foveal ONL thickness was greater in glaucomatous eyes ( $P = .011$ ) than in normal eyes. **Conclusions.** Glaucomatous damage may involve structural change in the photoreceptor layer.

## 1. Introduction

Glaucoma is characterized by progressive loss of retinal ganglion cells. However, it remains controversial whether the photoreceptor layer is involved. Kendell et al. examined the number and density of photoreceptors in postmortem eyes and found no significant difference between glaucoma and age-matched control groups [1]. By contrast, Panda and Jonas showed that the photoreceptor count was significantly lower in enucleated eyes with secondary angle-closure glaucoma [2]. In the study by Nork et al., they observed swelling of red- and green-sensitive cones in deceased donors who had a clinical diagnosis of chronic glaucoma [3]. In these studies, measurements of photoreceptors were performed in histological sections. Tissue autolysis before fixation and tissue processing may disrupt the density and architecture of the photoreceptor layer rendering assessment of the photoreceptors inaccurate.

Optical coherence tomography (OCT) is an imaging technology that allows noninvasive in vivo measurement of the retinal layers. While the resolution of time-domain OCT has been largely limited to measuring the retinal and retinal nerve fiber layer (RNFL) thicknesses, the recent availability of spectral-domain OCT has permitted visualization of multiple intraretinal layers [4, 5]. With an axial resolution of approximately 5  $\mu\text{m}$ , the spectral-domain OCT distinctively discriminates the outer plexiform layer, the outer nuclear layer, the external limiting membrane, the junction of inner and outer segments of the photoreceptors, and the retinal pigment epithelium. In vivo measurement of photoreceptor layer thickness is thus possible. Investigating the involvement of photoreceptor is pertinent to understanding the extent of retinal damage in glaucoma patients and developing new psychophysical tests for glaucoma detection. The objective of this study was to measure and compare the photoreceptor layer thickness between normal and glaucomatous eyes.

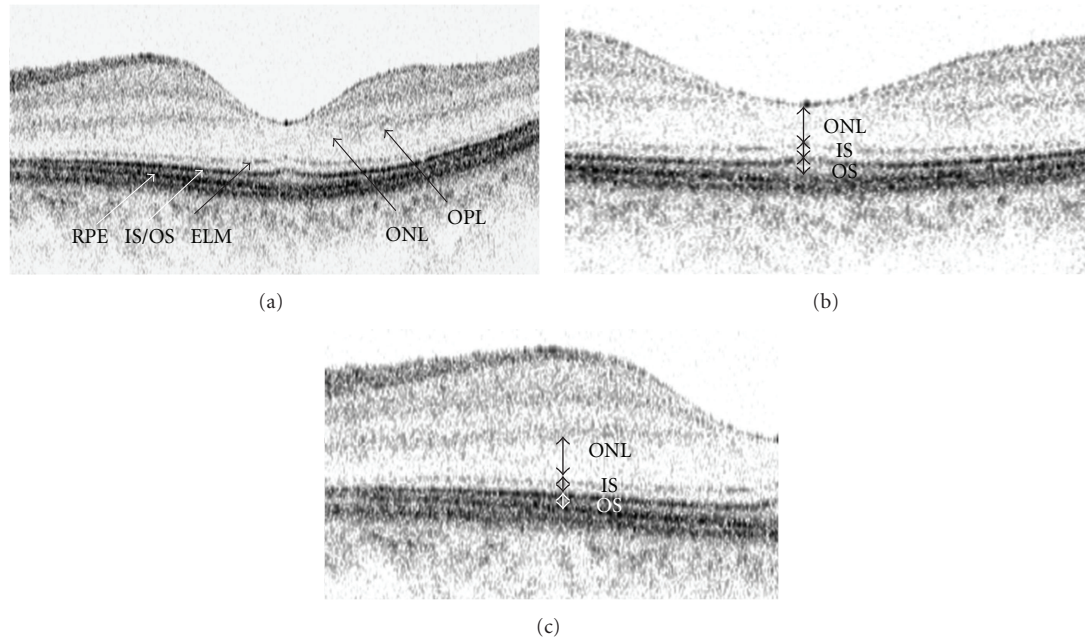


FIGURE 1: Macular imaging with spectral-domain optical coherence tomography (a). The outer nuclear layer (ONL) thickness is defined as the distance between the posterior boundary of outer plexiform layer and external limiting membrane. The inner and outer segments (IS + OS) are defined as the distance between the external limiting membrane and the RPE. Measurements were obtained at the foveola (b) and 1.5 mm from the fovea (c). OPL: outer plexiform layer; ONL: outer nuclear layer; ELM: external limiting membrane; IS + OS: inner and outer segments; RPE: retinal pigment epithelium.

## 2. Methods

**2.1. Subjects.** Thirty-eight healthy normal Chinese volunteers and 47 glaucoma patients were consecutively recruited. They underwent a full ophthalmic examination including visual acuity, refraction, intraocular pressure measurement, and gonioscopy and fundus examination. All subjects had visual acuity of at least 20/40, spherical error within the range between +3.0 and -6.0 diopters. Subjects with clinical evidence of macular edema, retinal disease, previous refractive or retinal surgery, neurological disease, or diabetes were excluded. Normal subjects had no visual field defect, no structural optic disc abnormalities, no history of intraocular pressure >21 mmHg, and no history of ocular or neurological diseases. Glaucoma patients were defined based on the presence of visual field defects (see below) and glaucomatous optic disc changes including narrowing of neuroretinal rim and/or retinal nerve fiber layer (RNFL) defect. Only one eye was randomly selected from each subject for analysis. The study was conducted in accordance with the ethical standards stated in the 1964 Declaration of Helsinki with approval obtained from the local ethics committee. Informed consent was obtained.

**2.2. Measurement of Photoreceptor Layer Thickness.** Spectral-domain OCT imaging was performed with the 3D OCT-1000 (Topcon, Tokyo, Japan). The details of the principle of spectral-domain OCT have been described [6, 7]. The OCT used a superluminescent diode laser with a center wavelength of 840 nm and a bandwidth of 50 nm as a light source. The

acquisition rate of the 3D OCT was 18,000 A scans per second. The transverse and axial resolutions were 20  $\mu\text{m}$  and 5  $\mu\text{m}$ , respectively. In the selected eye, the macula was imaged by 6 radial lines centered at the fovea spaced 30° apart. Each scan line was 6 mm long consisting of 2048 A scans. All images were obtained with a signal strength of at least 60 as recommended by the manufacturer. Three subjects were excluded because of the presence of drusen at the macula.

Since the built-in software only provided automatic delineation and measurement of the retinal and retinal nerve fiber layer thicknesses, macular images were exported and analyzed with an image analysis software (SigmaScan Pro version 5.0; Systat software Inc., Point Richmond, Calif, USA). The outer plexiform layer, the external limiting membrane, the junction of inner and outer segments, and the retinal pigment epithelium were identified in the OCT image (Figure 1(a)). The outer nuclear layer (defined as the distance between the posterior boundary of outer plexiform layer and external limiting membrane), the inner and outer segments (the distance between the external limiting membrane and the RPE), and the total photoreceptor layer (outer nuclear layer + inner and outer segments of photoreceptors) thicknesses were manually measured in each scan. Measurements were obtained at the fovea, and at 1.5 mm away from the fovea (Figures 1(b) and 1(c)). A total of 6 images captured at different meridians were analyzed in each eye. The central foveal photoreceptor thickness was calculated by taking the average of the 6 linear scans whereas the 1.5 mm parafoveal photoreceptor thicknesses were calculated by taking the

TABLE 1: Subject characteristics.

	Normal ( $n = 38$ )	Glaucoma ( $n = 47$ )	$P$
Gender (male/female)	13/25	27/20	.055*
Age (years) mean $\pm$ SD	53.6 $\pm$ 14.5	56.4 $\pm$ 12.9	.348 <sup>†</sup>
Refraction (D) mean $\pm$ SD	-0.35 $\pm$ 2.65	-1.15 $\pm$ 2.65	.172 <sup>†</sup>
Visual field MD (dB) mean $\pm$ SD	-0.26 $\pm$ 1.21	-9.91 $\pm$ 8.29	<.001 <sup>†</sup>

D: diopters; MD: mean deviation; SD: standard deviation.

\*Chi-square test.

<sup>†</sup>Independent sample  $t$ -test.

TABLE 2: Mean  $\pm$  standard deviation (SD), repeatability coefficient, within-subject coefficient of variation ( $CV_w$ ), and intraclass correlation coefficient (ICC) of outer nuclear layer (ONL) and inner and outer segments (IS/OS) thicknesses in a random sample of 30 normal subjects.

	Mean $\pm$ SD ( $\mu\text{m}$ )	Repeatability coefficient ( $\mu\text{m}$ ) (95% CI)	$CV_w$ (%) (95% CI)	ICC (95% CI)
ONL Thickness	98.22 $\pm$ 15.47	8.470 (7.296–9.644)	3.11 (2.56–3.67)	0.964 (0.936–0.982)
IS/OS thickness	59.60 $\pm$ 7.22	8.134 (7.007–9.262)	4.93 (4.05–5.81)	0.821 (0.701–0.903)

95% CI: 95% confidence interval.

average of the 12 measurements from the 6 linear scans. All measurements were obtained by a masked observer. Thirty images from 30 normal subjects were randomly selected to determine the measurement repeatability. The foveal ONL and IS+OS layer thicknesses in each image were measured by the same observer for 3 times in 3 separate occasions.

**2.3. Visual Field Examination.** Standard visual field testing was performed using static automated white-on-white threshold perimetry (SITA Standard 24-2, Humphrey Field Analyzer II, Carl Zeiss Meditec, Dublin, Calif, USA). A visual field was defined as reliable when fixation losses were less than 20% false positive and false negative errors were less than 15%. Visual field sensitivity was expressed in MD (mean deviation) and PSD (pattern standard deviation), as calculated by the perimetry software. A field defect was defined as having three or more significant ( $P < .05$ ) nonedge contiguous points with at least one at the  $P < .01$  level on the same side of horizontal meridian in the pattern deviation plot, classified as outside normal limits in the glaucoma hemifield test and confirmed with at least two visual field tests. None of the normal subjects had a visual field defect.

**2.4. Statistical Analysis.** Statistical analyses were performed using SPSS version 15.0 (SPSS Inc., Chicago, Ill, USA). Foveal and parafoveal (1.5 mm) photoreceptor thicknesses were compared with independent  $t$ -test. The differences of photoreceptor thicknesses among normal, mild (MD  $> -6$  dB), and moderate to advanced (MD  $\leq -6$  dB) glaucoma groups were compared with analysis of variance with Bonferroni correction for multiple comparisons. The repeatability coefficient (2.77x within subject standard deviation ( $Sw$ )), coefficient of variation  $CV_w$  (100x  $Sw$ /overall mean) and intraclass correlation coefficient (ICC) were computed. The  $Sw$  was calculated as the square root of the within-subject mean square of error (the unbiased estimator of the component of variance due to random error) in a

one-way random effects model [8]. The ICC is the ratio of the intersubject component of variance to the total variance (intersubject variance + within subject variance).

### 3. Results

The demographics and visual field MD of the normal and glaucoma groups are shown in Table 1. There was no difference in age ( $P = .35$ ) and refraction ( $P = .17$ ) between the groups. The visual field MD of the normal group ( $-0.26 \pm 1.21$  dB) was greater than that of the glaucoma group ( $-9.91 \pm 8.29$  dB) ( $P < .01$ ). Table 2 shows the intraobserver measurement repeatability of the outer nuclear layer (ONL) and the inner and outer segments (IS+OS) layer thicknesses. The intraclass correlation coefficients of the ONL and IS+OS thicknesses were 0.964 (95% confidence interval: 0.936–0.982) and 0.821 (95% confidence interval: 0.701–0.903), respectively.

For the normal eyes, the foveal ONL, IS+OS and total photoreceptor thicknesses were  $96.7 \pm 10.7 \mu\text{m}$ ,  $59.3 \pm 5.5 \mu\text{m}$ , and  $155.6 \pm 12.6 \mu\text{m}$ , respectively (Table 3). These measurements were smaller compared to those obtained in glaucomatous eyes ( $103.7 \pm 13.3 \mu\text{m}$ ,  $59.5 \pm 5.5 \mu\text{m}$ , and  $162.9 \pm 15.9 \mu\text{m}$ , resp.) with significant differences found in the foveal ONL ( $P = .01$ ) and total photoreceptor ( $P = .03$ ) thicknesses. The parafoveal (1.5 mm) photoreceptor measurements were smaller than the foveal measurements for both normal and glaucoma subjects (all with  $P < .01$ ). There were no detectable differences in the parafoveal (1.5 mm) photoreceptor measurements between the normal and glaucoma groups ( $P \geq .23$ ) (Table 4).

The ONL thickness was significantly greater in mild glaucomatous compared with normal eyes ( $P = .02$ ) whereas no difference was found comparing normal and moderate to advanced glaucomatous eyes ( $P = .35$ ). The IS+OS layer thickness was comparable among the three diagnostic groups ( $P \geq .72$ ).

TABLE 3: Mean foveal outer nuclear layer, inner and outer segments, and photoreceptor layer thicknesses in the normal and glaucoma groups.

	ONL thickness ( $\mu\text{m}$ )	IS/OS thickness ( $\mu\text{m}$ )	Photoreceptor layer thickness ( $\mu\text{m}$ )
Normal ( $n = 38$ )	$96.7 \pm 10.7$	$59.3 \pm 5.5$	$155.6 \pm 12.6$
Glaucoma ( $n = 47$ )	$103.7 \pm 13.3$	$59.5 \pm 5.5$	$162.9 \pm 15.9$
* $P$	.011	.890	.025

\* Independent-sample  $t$ -test.

TABLE 4: Mean parafoveal (1.5 mm) outer nuclear layer, inner and outer segments and photoreceptor layer thicknesses in the normal and glaucoma groups.

	ONL thickness ( $\mu\text{m}$ )	IS/OS thickness ( $\mu\text{m}$ )	Photoreceptor layer thickness ( $\mu\text{m}$ )
Normal ( $n = 38$ )	$70.9 \pm 14.0$	$45.2 \pm 6.4$	$116.1 \pm 18.7$
Glaucoma ( $n = 47$ )	$68.7 \pm 10.7$	$43.6 \pm 5.5$	$112.3 \pm 14.4$
* $P$	.410	.228	.295

\* Independent-sample  $t$ -test.

#### 4. Discussion

There are only a few histological studies investigating the involvement of photoreceptor layer in human glaucoma. The largest series was reported by Nork et al. [3]. In their study, the maculas from 128 human eyes with a diagnosis of chronic glaucoma and 90 control eyes were examined histologically. They showed that, in a subset of glaucomatous eyes, the cone nuclei at the outer portion of ONL were enlarged and the somata were swollen. Although they did not mention the severity of glaucomatous damage, their result concurs with our observation that the foveal ONL thickness was increased in a subset of patients with mild glaucoma. Cone density is the highest at the fovea (central one degree of the macula). Swollen cone perikarya could be manifested as increase in ONL thickness. In the study by Kendell, they did not find significant difference in ONL height or photoreceptor nuclei density between 9 normal and 14 glaucoma eyes [1]. However, it is notable that the photoreceptor measurements were largely based on the peripheral retina where rods dominate. Wagnanski et al. also showed that there was no cone loss in the parafoveal area (4.5 to 6 degrees eccentricity above and below the fovea) in experimental glaucoma [9]. Likewise, we did not find any significant difference in photoreceptor thicknesses between normal and glaucomatous eyes at the parafoveal (1.5 mm) region where rods outnumber cones. Panda and Jonas reported that the number of photoreceptors was reduced in 23 eyes with angle-closure glaucoma secondary to perforating corneal injuries in comparison to 14 control eyes with malignant choroidal melanoma [2]. All the eyes had high intraocular pressure resulting in painful bullous keratopathy not amenable to anti-glaucoma treatments. Loss of photoreceptors might be a result of retinal ischemia, not glaucoma. Ocular trauma per se could also result in loss of photoreceptors [10, 11]. Collectively, our finding of increased foveal, but not the parafoveal (1.5 mm), photoreceptor thickness in glaucoma is in agreement with the existing histological studies in human eyes.

Increased photoreceptor thickness in glaucoma has been reported by Ishikawa et al. [12]. They developed a software

algorithm to perform segmentation of retinal layers at the macula imaged by a time-domain OCT (Stratus OCT, Carl Zeiss Meditec, Dublin, Calif, USA). Since it was difficult to delineate the photoreceptor layer, the OCT images were pre-processed to improve the segmentation performance. They demonstrated that the outer retinal complex (comprising the ONL and the IS+OS layer) was significantly increased in glaucoma ( $100.4 \mu\text{m}$ ) compared with the normal control ( $93.8 \mu\text{m}$ ,  $P = .035$ ). This serendipitous result, however, was attributed by potential inaccurate definition of the outer retinal complex on the OCT A-scan profile. Two recent case series, however, showed losses in cone density and thinning of the photoreceptor outer segments in patients with glaucoma [13, 14].

Two hypotheses were proposed by Nork et al. to explain the swelling of photoreceptors in glaucoma [3, 15]. In the anterograde hypothesis, reduced choroidal blood flow causes ischemia and swelling of the photoreceptors resulting in a decrease in reuptake of glutamate. The retinal ganglion cells undergo apoptosis because of glutamate overload. In the retrograde hypothesis, the photoreceptors are directly involved as a consequence of degenerating retinal ganglion cells. If this hypothesis is correct, it is expected that there would be no photoreceptors swelling in eyes with advanced glaucoma. Nork et al. considered that the anterograde hypothesis was more plausible because they found that 5 out of the 20 eyes (25%) with severe glaucoma in their study exhibited definite photoreceptor swelling [3]. Nevertheless, our in vivo measurement, which was devoid of the effect of tissue autolysis and fixation artifact, demonstrated that, while thickening of the ONL was observed in patients with mild glaucoma (visual field MD  $> -6$  dB), the ONL thickness was comparable between the normal and the moderate to advanced glaucoma (visual field MD  $< -6$  dB) groups. These findings align with the anterograde hypothesis. Prospective studies are needed to characterize the longitudinal profile of photoreceptor changes in glaucoma patients.

The involvement of photoreceptors in glaucoma is supported by a number of functional studies with electroretinogram (ERG) [16–18]. In the study by Vaegan et al., they demonstrated reduction and delay of ERG a and b waves

in glaucomatous eyes [16], which were comparable to those observed in early cone-rod dystrophy. Likewise, Weiner et al. showed that foveal cone ERG amplitude was subnormal in a significant proportion of glaucoma patients [17]. These studies suggest that the outer retina could be functionally abnormal in glaucoma.

In this study, the foveola was measured because this location has the highest density of cones. In fact, 80% of the retinal ganglion cells connect exclusively to cones making the foveola a strategic location studying the involvement of photoreceptors in glaucoma [19]. It is interesting to note that there were no significant differences in parafoveal photoreceptor thicknesses between the normal and glaucoma groups. This concurs with the observation that cone (but not rod) swelling is associated with glaucoma [3]. While evaluation of cellular density or morphology would be a much more sensitive approach to detect photoreceptor changes, it has not been possible to visualize individual photoreceptors with spectral-domain OCT. Nevertheless, thickness measurement could serve as a reasonable surrogate to evaluate the integrity of photoreceptors.

In summary, in vivo measurement of photoreceptors provides a unique approach to study the association between photoreceptors and glaucoma. Although cone swelling observed in the previous histological studies offers a probable explanation for the increased foveal ONL thickness in glaucoma, infiltration of glial cells or inflammatory cells and increased extracellular matrix deposition may also contribute to the thickening. Further investigations are needed to unfold the mechanisms and functional consequences of increased photoreceptor thickness in glaucoma.

## Acknowledgment

C. K. Leung has received speaker honoraria and research support from Topcon and Carl Zeiss Meditec.

## References

- [1] K. R. Kendell, H. A. Quigley, L. A. Kerrigan, M. E. Pease, and E. N. Quigley, "Primary open-angle glaucoma is not associated with photoreceptor loss," *Investigative Ophthalmology and Visual Science*, vol. 36, no. 1, pp. 200–205, 1995.
- [2] S. Panda and J. B. Jonas, "Decreased photoreceptor count in human eyes with secondary angle-closure glaucoma," *Investigative Ophthalmology and Visual Science*, vol. 33, no. 8, pp. 2532–2536, 1992.
- [3] T. M. Nork, J. N. Ver Hoeve, G. L. Poulsen et al., "Swelling and loss of photoreceptors in chronic human and experimental glaucomas," *Archives of Ophthalmology*, vol. 118, no. 2, pp. 235–245, 2000.
- [4] M. Ota, A. Tsujikawa, T. Murakami et al., "Foveal photoreceptor layer in eyes with persistent cystoid macular edema associated with branch retinal vein occlusion," *American Journal of Ophthalmology*, vol. 145, no. 2, pp. 273–280, 2008.
- [5] N. Yamaike, A. Tsujikawa, M. Ota et al., "Three-dimensional imaging of cystoid macular edema in retinal vein occlusion," *Ophthalmology*, vol. 115, no. 2, pp. 355–362, 2008.
- [6] N. Nassif, B. Cense, B. H. Park et al., "In vivo human retinal imaging by ultrahigh-speed spectral domain optical coherence tomography," *Optics Letters*, vol. 29, no. 5, pp. 480–482, 2004.
- [7] M. A. Choma, M. V. Sarunic, C. H. Yang, and J. A. Izatt, "Sensitivity advantage of swept source and Fourier domain optical coherence tomography," *Optics Express*, vol. 11, no. 18, pp. 2183–2189, 2003.
- [8] J. M. Bland and D. G. Altman, "Measurement error," *British Medical Journal*, vol. 312, article 744, 1996.
- [9] T. Wygnanski, H. Desatnik, H. A. Quigley, and Y. Glovinsky, "Comparison of ganglion cell loss and cone loss in experimental glaucoma," *American Journal of Ophthalmology*, vol. 120, no. 2, pp. 184–189, 1995.
- [10] H. A. Quigley, "Selective citation of evidence regarding photoreceptor loss in glaucoma," *Archives of Ophthalmology*, vol. 119, no. 9, pp. 1390–1391, 2001.
- [11] J. O. Sipperley, H. A. Quigley, and D. M. Gass, "Traumatic retinopathy in primates: the explanation of commotio retinae," *Archives of Ophthalmology*, vol. 96, no. 12, pp. 2267–2273, 1978.
- [12] H. Ishikawa, D. M. Stein, G. Wollstein, S. Beaton, J. G. Fujimoto, and J. S. Schuman, "Macular segmentation with optical coherence tomography," *Investigative Ophthalmology and Visual Science*, vol. 46, no. 6, pp. 2012–2017, 2005.
- [13] S. S. Choi, R. J. Zawadzki, M. C. Lim et al., "Evidence of outer retinal changes in glaucoma patients as revealed by ultrahigh-resolution in vivo retinal imaging," *British Journal of Ophthalmology*, vol. 95, no. 1, pp. 131–141, 2011.
- [14] J. S. Werner, J. L. Keltner, R. J. Zawadzki, and S. S. Choi, "Outer retinal abnormalities associated with inner retinal pathology in nonglaucomatous and glaucomatous optic neuropathies," *Eye*, vol. 25, no. 3, pp. 279–289, 2011.
- [15] T. M. Nork, "Acquired color vision loss and a possible mechanism of ganglion cell death in glaucoma," *Transactions of the American Ophthalmological Society*, vol. 98, pp. 331–363, 2000.
- [16] Vaegan, S. L. Graham, I. Goldberg, L. Buckland, and F. C. Hollows, "Flash and pattern electroretinogram changes with optic atrophy and glaucoma," *Experimental Eye Research*, vol. 60, no. 6, pp. 697–706, 1995.
- [17] A. Weiner, D. J. Ripkin, S. Patel, S. R. Kaufman, H. D. Kohn, and D. T. Weidenthal, "Foveal dysfunction and central visual field loss in glaucoma," *Archives of Ophthalmology*, vol. 116, no. 9, pp. 1169–1174, 1998.
- [18] I. M. Velten, M. Korth, and F. K. Horn, "The a-wave of the dark adapted electroretinogram in glaucomas: are photoreceptors affected?" *British Journal of Ophthalmology*, vol. 85, no. 4, pp. 397–402, 2001.
- [19] V. H. Perry, R. Oehler, and A. Cowey, "Retinal ganglion cells that project to the dorsal lateral geniculate nucleus in the macaque monkey," *Neuroscience*, vol. 12, no. 4, pp. 1101–1123, 1984.

## Clinical Study

# Comparison of Photopic Negative Response of Full-Field and Focal Electroretinograms in Detecting Glaucomatous Eyes

Shigeki Machida, Kunifusa Tamada, Taku Oikawa, Yasutaka Gotoh, Tomoharu Nishimura, Muneyoshi Kaneko, and Daijiro Kurosaka

Department of Ophthalmology, School of Medicine, Iwate Medical University, 19-1 Uchimaru Morioka, Iwate 020-8505, Japan

Correspondence should be addressed to Shigeki Machida, smachida@iwate-med.ac.jp

Received 29 April 2010; Revised 24 June 2010; Accepted 22 August 2010

Academic Editor: Christopher Leung

Copyright © 2011 Shigeki Machida et al. This is an open access article distributed under the Creative Commons Attribution License, which permits unrestricted use, distribution, and reproduction in any medium, provided the original work is properly cited.

**Purpose.** To compare the photopic negative response (PhNR) of the full-field electroretinogram (ERG) to the PhNR of the focal ERGs in detecting glaucoma. **Methods.** One hundred and three eyes with glaucoma and 42 normal eyes were studied. Full-field ERGs were elicited by red stimuli on a blue background. The focal ERGs were elicited by a 15° white stimulus spot centered on the macula, the superotemporal or the inferotemporal areas of the macula. **Results.** In early glaucoma, the areas under the receiver operating characteristic curves (AUCs) were significantly larger for the focal PhNR (0.863–0.924) than those for the full-field PhNR (0.666–0.748) ( $P < .05$ ). The sensitivity was significantly higher for the focal PhNR than for the full-field PhNR in early ( $P < .01$ ) and intermediate glaucoma ( $P < .05$ ). In advanced glaucoma, there was no difference in the AUCs and sensitivities between the focal and full-field PhNRs. **Conclusions.** The focal ERG has the diagnostic ability with higher sensitivity in detecting early and intermediate glaucoma than the full-field ERG.

## 1. Introduction

It has been generally believed that the activity of retinal ganglion cells (RGCs) contributes little to shaping the corneal electroretinogram (ERG) elicited by Ganzfeld stimuli (full-field ERG). However, a response has been newly identified to originate from RGCs that receive signals from cones [1]. This response was termed the photopic negative response (PhNR) [2], and it consists of a negative-going wave that follows the photopic cone b-wave.

The PhNR is strongly attenuated in primate's eyes with experimentally induced glaucoma and also in eyes intravitreally injected with tetrodotoxin [2], a blocker of the neural activity of retinal ganglion cells, their axons, and amacrine cells [3, 4]. In addition to this experimental evidence, it has been demonstrated that the PhNR was reduced in patients with optic nerve and retinal diseases that affect mainly the RGCs and retinal nerve fiber layer [5–16]. We have shown that the amplitudes of the PhNR of the full-field cone ERG (full-field PhNR) were correlated with

visual sensitivity, disc topography, and retinal nerve fiber layer thickness in eyes with open angle glaucoma (OAG) [16]. These results indicate that the full-field PhNR can be used as an objective functional measure of the RGCs in glaucomatous eyes.

When the full-field PhNR amplitude was used as a diagnostic tool, the sensitivity and specificity to discriminate glaucomatous from normal eyes were 77% and 90%, respectively [16]. However, at the early stage of glaucoma, the sensitivity was reduced to 57%, indicating that the full-field PhNR is not suitable for diagnosing early glaucoma. This is not surprising because the early glaucomatous changes begin with localized neuronal loss in the retina and optic nerve head that could not be detected by the full-field ERG.

The focal ERG system originally developed by Miyake et al. [17] is now commercially available in Japan. Recently, we have recorded focal ERGs from patients with glaucoma [18–20] and optic nerve diseases [21]. We found that the PhNR of the focal ERG (focal PhNR) was also selectively attenuated in patients with OAG. In addition, we investigated

correlation between the focal PhNR and corresponding retinal sensitivity obtained by standard automated perimetry (SAP). A curvilinear relationship was found between the focal PhNR amplitude and retinal sensitivity (decibel), in which a reduction of the focal PhNR amplitude was associated with a small decrease of retinal sensitivity at the early stage of glaucoma [18]. This suggests that the focal PhNR may be used for detecting functional loss at the early stage of glaucoma. This focal ERG system allows us to record focal retinal responses from the paramacular regions of the retina that are preferentially affected at the early stage of glaucoma. In our recent study, we recorded focal ERGs from three retinal loci including the macular region, the supero-temporal and infero-temporal areas of the macula. The sensitivity and specificity of the focal PhNR to discriminate early glaucoma were >90%. These findings were made with the combined criterion in which eyes were classified as being glaucomatous when the focal PhNR amplitudes were less than the optimal cut-off values in either retinal locus [19].

From these results, it appeared that the focal PhNR is better than the full-field PhNR to discriminate glaucomatous from normal eyes. However, a direct comparative study comparing the diagnostic values of full-field and focal PhNRs obtained from the same eyes has not been reported although studies using different patient populations for the full-field and focal PhNRs have been done [16, 18, 19].

Thus, the purpose of this study was to compare the ability of the full-field and focal PhNRs to detect glaucomatous eyes at different stages. Importantly, the full-field and focal PhNRs were recorded from the same eyes.

## 2. Methods

**2.1. Patients.** One hundred and three eyes of 103 patients with OAG were studied. Their ages ranged from 37 to 83 years with a mean  $\pm$  standard deviation of  $68.2 \pm 9.1$  years. The diagnosis of OAG was based on the presence of a glaucomatous optic disc associated with visual field defects measured by SAP. The presence of glaucomatous optic disc was determined by the guideline of Japanese Society of Glaucoma developed in 2005 (<http://www.nichigan.or.jp/member/guideline/glaucoma2.jsp>). According to the diagnostic criterion for minimal abnormality of the visual field [22], the visual field defect was determined to be glaucomatous when it met one of three criteria. (1) The pattern deviation plot showed a cluster of three or more nonedge points that had lower sensitivities than those in 5% of the normal population ( $P < .05$ ), and one of the points had a sensitivity that was lower than 1% of the population ( $P < .01$ ), (2) the value of the corrected pattern standard deviation was lower than that of 5% of the normal visual field ( $P < .05$ ), or (3) the Glaucoma Hemifield Test showed that the field was outside the normal limits.

Forty-two eyes of 42 age-matched normal volunteers, ranging in age from 53 to 78 years with a mean of  $67.6 \pm 7.3$  years, were studied. We selected normal eyes from patients with macular hole in the fellow eye which was treated by vitrectomy. They underwent comprehensive

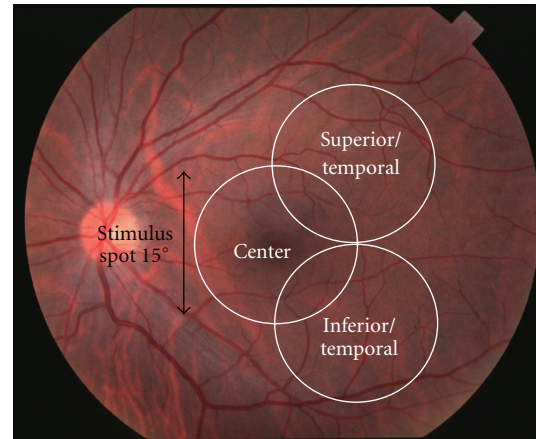


FIGURE 1: Ocular fundus photograph showing retinal areas which were stimulated by focal spots with a diameter of 15 degrees.

ophthalmological examinations including measuring visual acuity by a Snellen chart and observing the ocular fundus by an indirect ophthalmoscope as well as a biomicroscopic slit lamp. In addition, we performed optical coherence tomography and SAP to rule out macular and optic nerve diseases.

This research was conducted in accordance with the Institutional Guidelines of Iwate Medical University, and the procedures conformed to the tenets of the Declaration of Helsinki. An informed consent was obtained from all subjects after a full explanation of the nature of the experiments.

**2.2. ERG Recordings.** The pupils were maximally dilated to approximately 8 mm in diameter following topical application of a mixture of 0.5% tropicamide and 0.5% phenylephrine HCL. The recordings of the full-field and focal ERGs were made on the same eye on the same day. The stimulus conditions for the recordings of the full-field cone ERGs and focal ERGs have been reported in detail [16, 18].

The full-field cone ERGs were elicited by red stimuli of  $1\ 600\ \text{cd/m}^2$  ( $\lambda_{\text{max}} = 644\ \text{nm}$ , half-amplitude bandwidth = 35 nm) on a blue background of  $40\ \text{cd/m}^2$  ( $\lambda_{\text{max}} = 470\ \text{nm}$ , half-amplitude bandwidth = 18 nm). The duration of the stimulus was 3 msec. The stimulus and background lights were produced by light emitting diodes (LEDs) embedded in the contact lens.

Focal ERGs were recorded from the macular area and from the supero-temporal and infero-temporal areas of the macula. Responses from these areas are designated as the center, superior/temporal, and inferior/temporal responses, respectively (Figure 1). The stimulus system was integrated into the infrared fundus camera (Mayo Co., Nagoya, Japan), which had been developed by Miyake et al. [17]. The stimulus spot was 15 degrees in diameter and was placed on the retinal area of interest, and the position was confirmed by viewing the ocular fundus on a monitor. The intensity of the white stimulus and background lights was  $165\ \text{cd/m}^2$  and  $6.9\ \text{cd/m}^2$ , respectively. The stimulus duration was 10 ms. The focal ERGs were recorded with a Burian-Allen bipolar

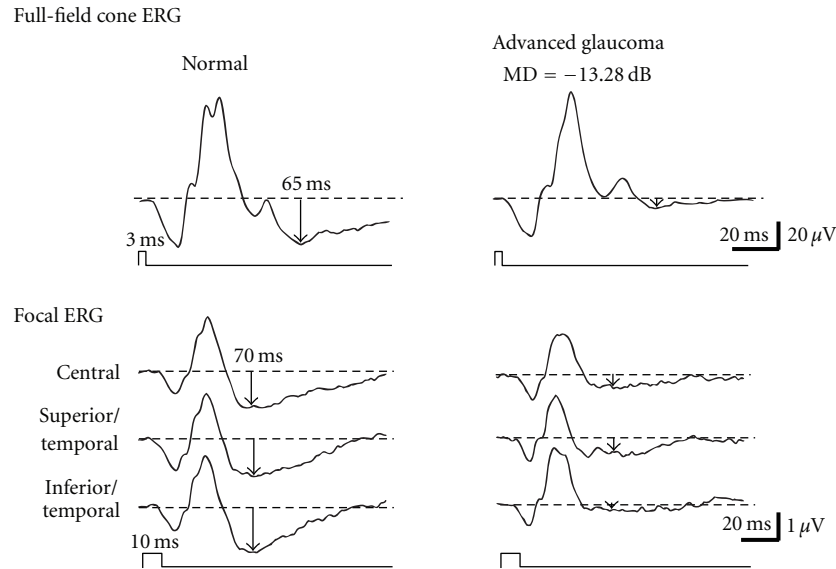


FIGURE 2: Representative full-field cone and focal electroretinograms recorded from a normal subject and a glaucoma patient with advanced visual field defects.

contact lens electrode (Hansen Ophthalmic Laboratories, Iowa City, IA).

The responses were digitally band-pass filtered from 0.5 to 1000 Hz for the full-field ERG and from 5 to 500 Hz for the focal ERG. It is often difficult to determine the negative trough of the PhNR especially in cases with reduced PhNR amplitudes. Therefore, we measured the PhNR amplitude at the fixed time points. We determined the time of the maximum amplitude of the PhNR in normal subjects according to the method of Rangaswamy et al. [9]. We found that the full-field and focal PhNRs were the largest at 65 ms and 70 ms after the flash, respectively. Therefore, we measured PhNR amplitudes at 65 ms for the full-field PhNR and 70 ms for the focal PhNR throughout the study (Figure 2).

**2.3. Visual Field Analyses.** The Humphrey Visual Field Analyzer (Model 750, Humphrey Instruments, San Leandro, CA, USA) was used for SAP. The SITA Standard strategy was applied to program 24-2. From the mean deviation (MD) of the 24-2 program, we classified patients with glaucomatous visual fields into three groups: early ( $MD > -6$  dB;  $n = 41$ , mean age and SD:  $68.6 \pm 9.8$  years), intermediate ( $-6$  dB  $\geq$  MD  $\geq -12$  dB;  $n = 28$ ,  $69.5 \pm 8.1$  years), and advanced (MD  $< -12$  dB;  $n = 34$ ,  $69.4 \pm 7.4$  years) defects of the visual field. There was no significant difference in the mean age among the three groups. The intraocular pressures (IOPs) of all patients were controlled under 21 mmHg by eye drops, and there was no significant difference in the IOPs among the groups. The averaged MDs were  $-3.31 \pm 1.58$ ,  $-8.88 \pm 1.67$ , and  $-17.37 \pm 4.46$  dB for the early, intermediate, and advanced groups, respectively.

When the fixation loss rate is higher than 20%, the field examination was determined to be unreliable and excluded from the analysis. In addition, when the false-positive or

false-negative error rates exceeded 33%, the visual field was not used for the analysis. The interval between the visual field testing and ERG recording was less than 1 month.

**2.4. Statistic Analyses.** We used receiver operating characteristic (ROC) curves to determine the optimal cut-off values that yielded the highest likelihood ratio. The area under the curve (AUC) was used to compare the ROC curves. The comparison between AUCs was made according to the method reported by DeLong et al. [23]. The sensitivity and specificity of the focal PhNR were compared to that of the PhNR of the full-field ERGs using Fisher's exact test. Unpaired *t* tests were used to compare data between groups with different degrees of the visual field defect. One-way ANOVA was used to determine the statistical significance of the ERG changes in eyes with the stage of glaucoma. These analyses were performed using commercial software MedCalc 11.3.3 (MedCalc Software, Mariakerke, Belgium) and Prism 5.1 (GraphPad Software Inc., San Diego, CA).

### 3. Results

**3.1. Representative ERG Waveforms from Normal and Glaucomatous Eyes.** The full-field and focal ERGs recorded from a normal control and a patient that had advanced glaucoma with a mean deviation  $-13.28$  dB are shown in Figure 2. Both the full-field and focal PhNRs were reduced in the patient compared to the normal control although there was no change in the amplitudes of the a- and b-waves in the full-field and focal ERGs (Figure 2).

**3.2. Averaged PhNR Amplitudes and PhNR/b-Wave Amplitude Ratios for Different Degrees of Visual Field Defects.** We have plotted the PhNR amplitudes and PhNR/b-wave amplitude

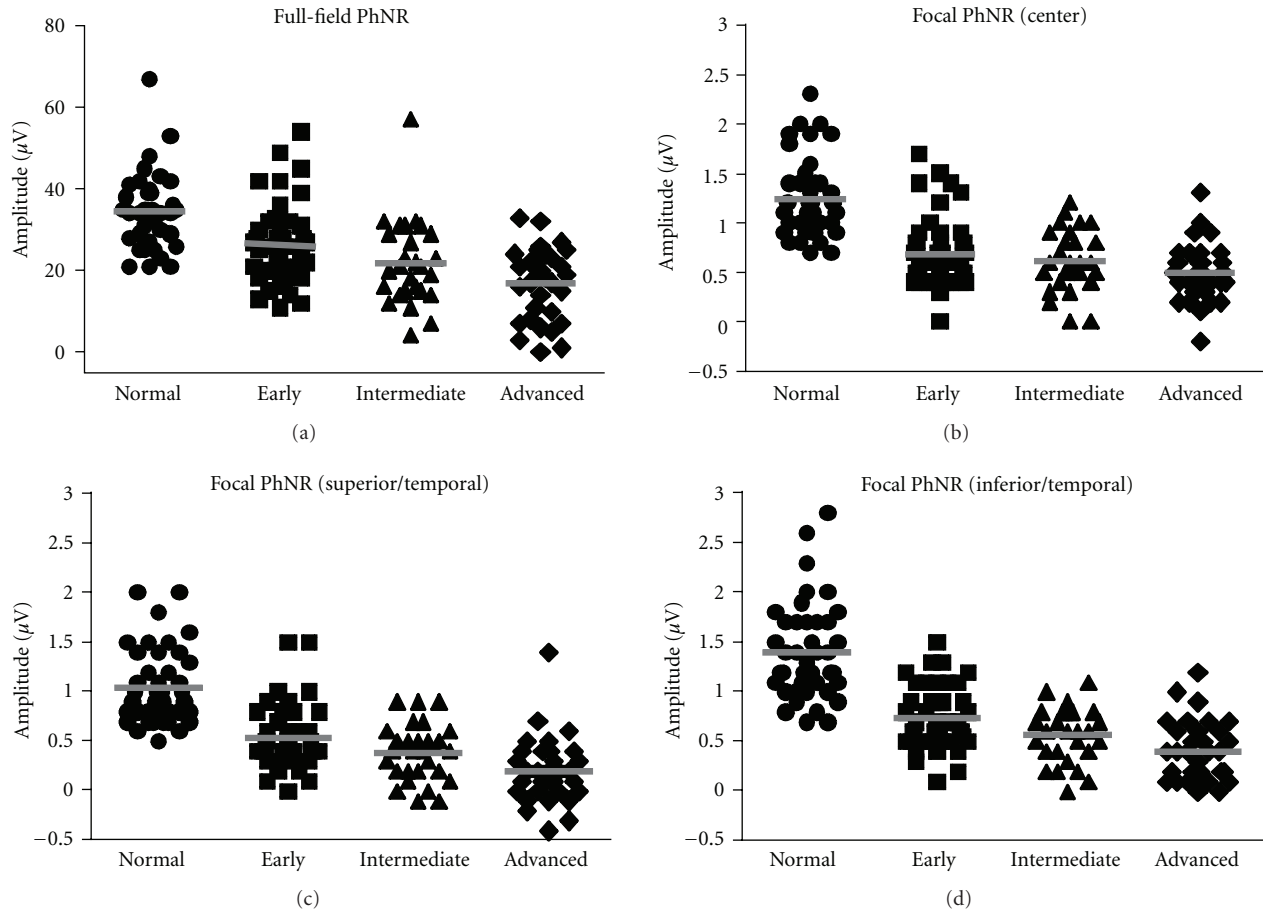


FIGURE 3: The PhNR amplitudes of the full-field (a) and focal ERGs (b) center, (c) superior/temporal, and (d) inferior/temporal are plotted for the normal controls (●) and glaucomatous eyes at early (■), intermediate (▲), and advanced stages (◆). Bars represent means of the PhNR amplitudes.

ratios against stages of glaucoma in Figures 3 and 4, respectively. In both the full-field and focal ERGs, the PhNR amplitudes and the PhNR/b-wave amplitude ratios were significantly and progressively reduced with an advance in the stage of glaucoma ( $P < .0001$ ). Even at the early stage of glaucoma, the PhNR amplitude and PhNR/b-wave amplitude ratio were significantly reduced compared to that in the normal controls for the full-field (PhNR amplitude:  $P < .004$ ) and focal ERGs (all retinal areas:  $P < .0001$ ). However, for the PhNR/b-wave amplitude ratio of the full-field ERGs, the data of the normal control considerably overlapped those from the early glaucoma group resulting in no significant differences (Figure 4(a)).

The PhNR amplitude and PhNR/b-wave amplitude ratio of the full-field ERGs gradually decreased as the stage of glaucoma advanced. On the other hand, the greatest loss of the PhNR amplitude and PhNR/b-wave amplitude ratio of the focal ERG was seen at the early stage of glaucoma. For example, the mean of the focal PhNR amplitude recorded from the center was reduced from  $1.24 \mu\text{V}$  to  $0.69 \mu\text{V}$  at the early stage of glaucoma. Then, it slightly decreased to  $0.50 \mu\text{V}$  at the advanced stage of glaucoma despite considerable loss of the visual sensitivity of SAP (Figure 3(b)).

The full-field PhNR amplitude fell outside the normal range in 29, 48, and 56% of patients of the early, intermediate, and advanced groups. The focal PhNR amplitudes of the central retinal area fell outside the normal range in 62, 61, and 76% of patients of the early, intermediate and advanced groups. The corresponding percentages for the superior/temporal and inferior/temporal focal PhNR amplitudes were 49 and 46% for the early, 59 and 57% for the intermediate, and 85 and 79% for the advanced groups, respectively. Thus, the focal PhNR amplitude showed abnormal values in more patients at any stages than the full-field PhNR amplitude. Similar results were obtained for the PhNR/b-wave amplitude ratio.

**3.3. ROC Curves of Full-Field and Focal ERGs.** The cut-off values were varied by  $1.0 \mu\text{V}$  steps for the full-field PhNR amplitude,  $0.1 \mu\text{V}$  for the focal PhNR amplitudes, and  $0.01 \mu\text{V}$  for the focal PhNR/b-wave amplitude ratio for the pooled data of glaucomatous and normal eyes. The sensitivity and specificity were obtained for each cut-off value and plotted to determine the ROC curves from which the AUC was obtained (Figures 5–7, Table 1).

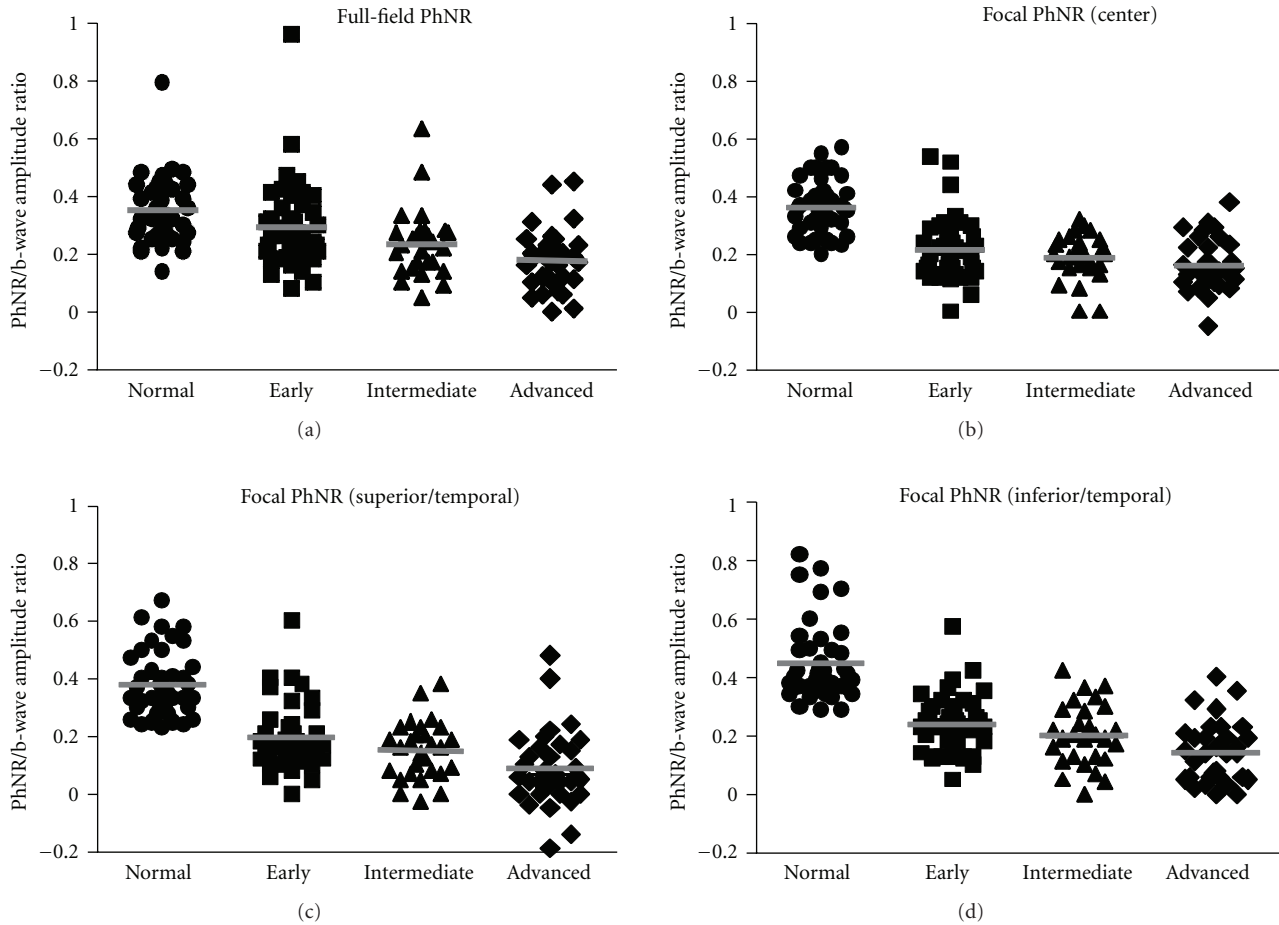


FIGURE 4: The PhNR/b-wave amplitude ratios of the full-field (a) and focal ERGs (b) center, (c) superior/temporal, and (d) inferior/temporal) are plotted for the normal controls (●) and glaucomatous eyes at early (■), intermediate (▲), and advanced stages (◆). Bars represent means of the PhNR/b-wave amplitude ratios.

In early glaucoma, the focal PhNR amplitude curves were always superior to the full-field PhNR amplitude curves. As a result, the AUC of the focal PhNR amplitude of the inferior/temporal area was significantly larger than that of the full-field PhNR amplitude (Figure 5(a),  $P < .05$ ). The AUCs of the focal PhNR/b-wave amplitude ratio obtained from all retinal areas were significantly larger than those of the full-field PhNR/b-wave amplitude ratio (Figure 5(b), Table 1,  $P = .01$  for the center,  $P = .001$  for the superior/temporal area, and  $P < .001$  for the inferior/temporal area).

For eyes with intermediate glaucoma, most parts of the ROC curves of the focal ERG amplitudes overlapped the curve of the PhNR amplitude of the full-field ERGs. Thus, there was no significant difference in the AUCs between the focal and full-field PhNR amplitudes (Figure 6(a)). For the PhNR/b-wave amplitude ratio, the curves of the focal PhNR/b-wave amplitude ratio were always higher than those of the full-field PhNR/b-wave amplitude ratio, resulting in significantly larger AUCs for the focal PhNR/b-wave amplitude ratio than for the full-field PhNR/b-wave amplitude ratio (Figure 6(b),  $P < .05$  for the center,  $P < .01$  for the inferior/temporal and superior/temporal areas).

In eyes with advanced glaucoma, the ROC curves for the PhNR amplitude and PhNR/b-wave amplitude ratio of the focal and full-field ERGs were overlapped (Figure 7). The differences in the AUCs between the full-field and focal PhNRs for both the PhNR amplitude and PhNR/b-wave amplitude ratio were not significant.

**3.4. Sensitivity and Specificity of Full-Field and Focal ERG PhNR.** The sensitivity and specificity were obtained with the optimal cut-off values for the PhNR amplitude (Table 2) and the PhNR/b-wave amplitude ratio (Table 3). Because the likelihood ratio reveals the sensitivity/false positive rate, the highest likelihood ratio indicates high sensitivity and specificity. Eyes were classified as being glaucomatous when their focal PhNR amplitudes or focal PhNR/b-wave amplitude ratio were less than the cut-off values in either retinal areas (combined criterion in Tables 2 and 3). In all patient groups with different degrees of visual field defects, no significant difference was found in the specificity between the full-field and focal PhNRs obtained from all retinal areas including the combined criteria.

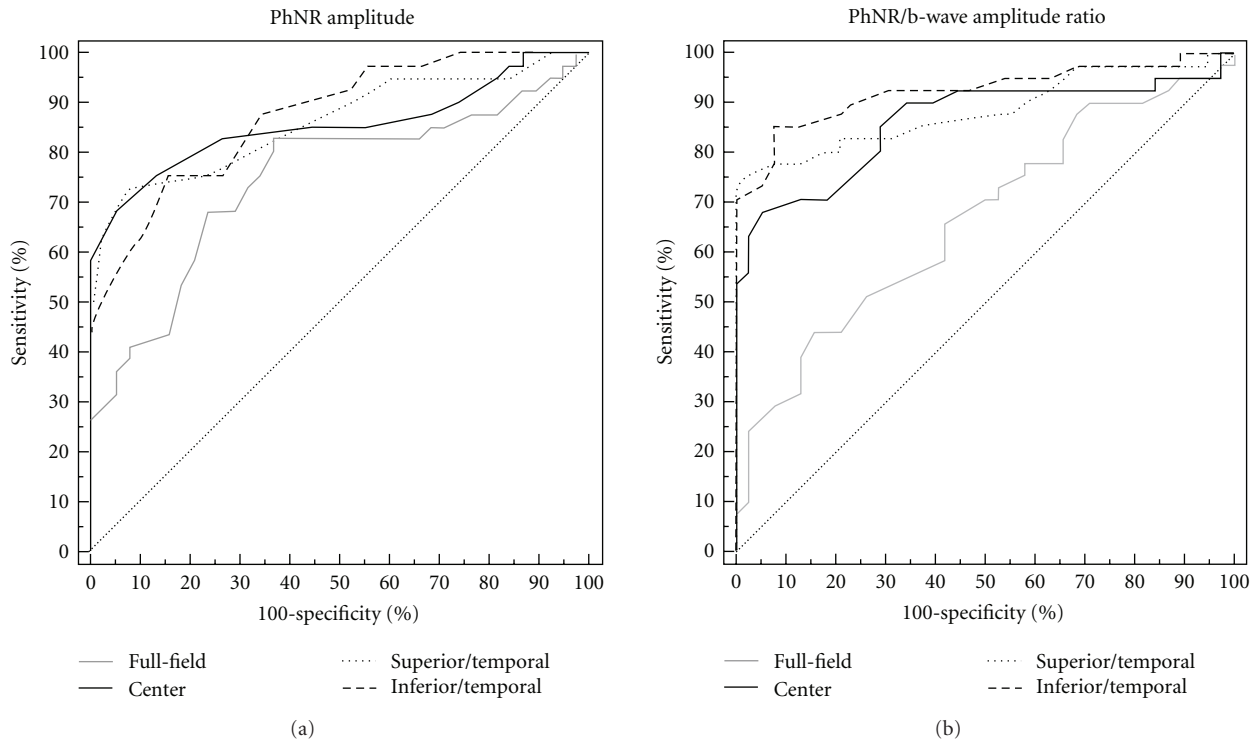


FIGURE 5: Receiver operating characteristic (ROC) curves for the PhNR amplitude (a) and PhNR/b-wave amplitude ratio (b) of the full-field and focal electroretinograms. Patients with early glaucoma ( $n = 41$ , mean deviation  $> -6$  dB). PhNR: photopic negative response.

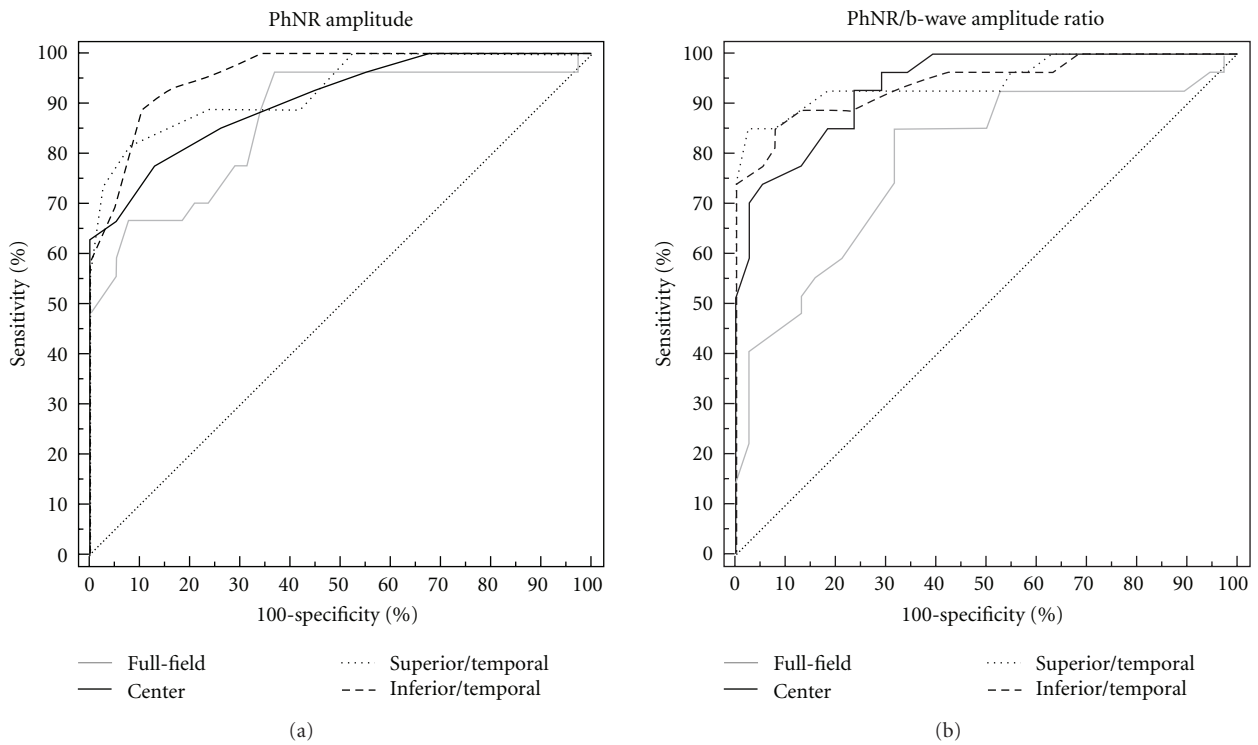


FIGURE 6: Receiver operating characteristic (ROC) curves for the PhNR amplitude (a) and PhNR/b-wave amplitude ratio (b) of the full-field and focal electroretinograms. Patients with intermediate glaucoma ( $n = 28$ ,  $-6$  dB  $\geq$  mean deviation  $\geq -12$  dB). PhNR: photopic negative response.

TABLE 1: Area under the curve of the PhNR amplitude and PhNR/b-wave amplitude ratio.

	PhNR amplitude		PhNR/b-wave amplitude ratio	
	AUC	95% CI	AUC	95% CI
<i>Early (n = 41)</i>				
Full-field ERG	0.748	0.638–0.839	0.666	0.551–0.768
Focal ERG				
Center	0.866	0.759–0.925	0.863	0.767–0.930
Sup/temp	0.863	0.767–0.930	0.886	0.795–0.947
Inf/temp	0.874	0.780–0.938	0.924	0.841–0.971
<i>Intermediate (n = 28)</i>				
Full-field ERG	0.865	0.758–0.937	0.789	0.670–0.880
Focal ERG				
Center	0.906	0.808–0.964	0.938	0.849–0.982
Sup/temp	0.929	0.838–0.978	0.946	0.860–0.987
Inf/temp	0.959	0.878–0.992	0.942	0.854–0.984
<i>Advanced (n = 34)</i>				
Full-field ERG	0.954	0.875–0.989	0.910	0.817–0.965
Focal ERG				
Center	0.951	0.871–0.988	0.930	0.842–0.977
Sup/temp	0.968	0.895–0.995	0.953	0.874–0.989
Inf/temp	0.972	0.902–0.996	0.972	0.901–0.996

PhNR: photopic negative response; AUC: area under the curve; CI: confidence interval; sup/temp: superior/temporal; inf/temp: inferior/temporal.

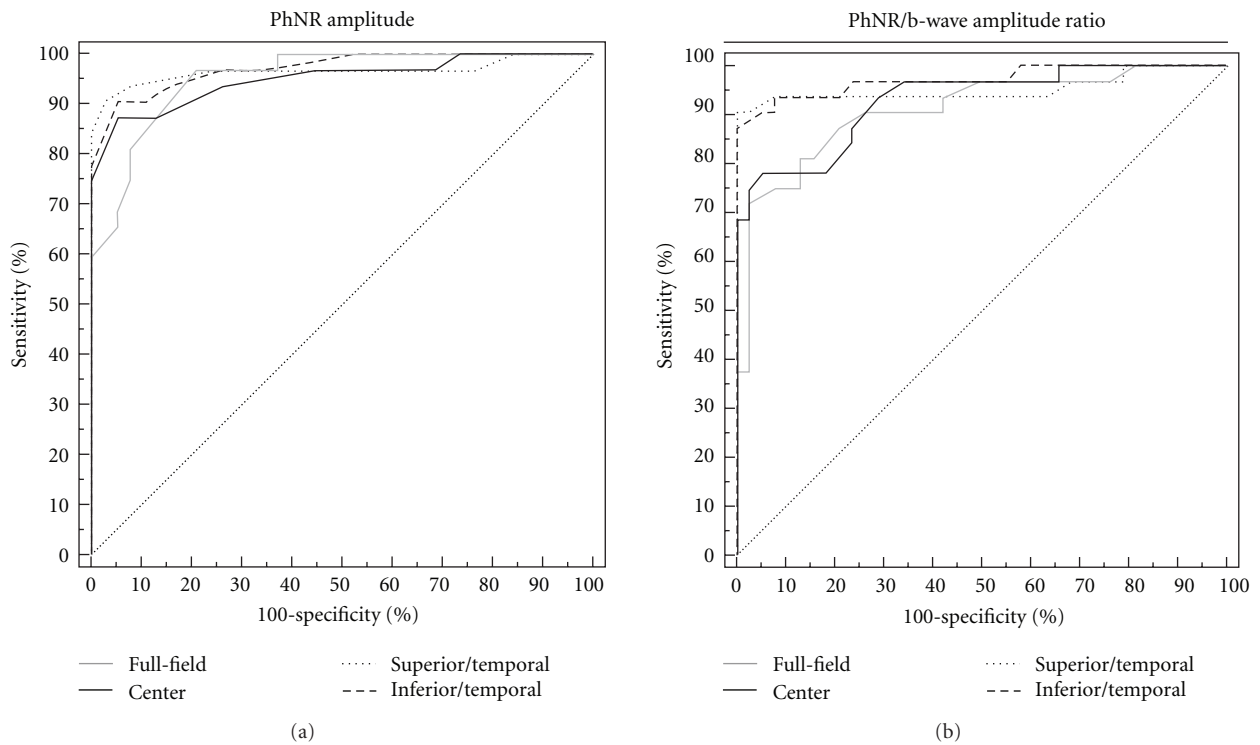


FIGURE 7: Receiver operating characteristic (ROC) curves for the PhNR amplitude (a) and PhNR/b-wave amplitude ratio (b) of the full-field and focal electroretinograms. Patients with *advanced* glaucoma ( $n = 34$ , mean deviation  $< -12$  dB). PhNR: photopic negative response.

TABLE 2: Sensitivity and specificity of the PhNR amplitude to discriminate glaucomatous eyes.

	Sensitivity (95%CI)	Specificity (95%CI)	Cut-off value ( $\mu$ V)
<i>Early (n = 41)</i>			
Full-field ERG	38.1 (23.6–54.4)	92.3 (79.1–98.3)	22
Focal ERG			
Center	69.1 (52.9–82.4)	95.2 (83.8–99.3)	0.7
Sup/temp	63.4 (46.9–77.9)	97.6 (87.1–99.6)	0.5
Inf/temp	56.1 (46.9–77.9)	95.2 (83.8–99.3)	0.7
Combined	88.1 (74.4–96.0)	90.5 (87.7–99.6)	
<i>Intermediate (n = 28)</i>			
Full-field ERG	59.3 (38.8–77.6)	92.3 (79.1–98.3)	22
Focal ERG			
Center	64.3 (44.1–81.3)	95.2 (83.8–99.3)	0.7
Sup/temp	75.0 (55.1–89.3)	97.6 (87.1–99.6)	0.5
Inf/temp	67.9 (47.7–84.1)	95.2 (83.8–99.3)	0.7
Combined	92.9 (87.7–99.6)	90.5 (87.7–99.6)	
<i>Advanced (n = 34)</i>			
Full-field ERG	66.7 (48.2–82.0)	92.3 (79.1–98.3)	22
Focal ERG			
Center	88.2 (72.5–96.6)	95.2 (83.8–99.3)	0.7
Sup/temp	90.9 (75.6–98.0)	97.6 (87.1–99.6)	0.5
Inf/temp	90.9 (75.6–98.0)	95.2 (83.8–99.3)	0.7
Combined	97.1 (87.7–99.6)	90.5 (87.7–99.6)	

PhNR: photopic negative response; CI: confidence interval; sup/temp: superior/temporal; inf/temp: inferior/temporal.

TABLE 3: Sensitivity and specificity of the PhNR/b-wave amplitude ratio to discriminate glaucomatous eyes.

	Sensitivity (95%CI)	Specificity (95%CI)	Cut-off value
<i>Early (n = 41)</i>			
Full-field ERG	23.8 (12.1–39.5)	97.4 (86.5–99.6)	0.19
Focal ERG			
Center	61.9 (45.6–76.4)	97.6 (87.4–99.6)	0.22
Sup/temp	75.6 (59.7–87.6)	97.6 (87.1–99.6)	0.23
Inf/temp	73.1 (57.1–85.3)	95.2 (83.8–99.3)	0.29
Combined	97.6 (87.7–99.6)	92.9 (87.7–99.6)	
<i>Intermediate (n = 28)</i>			
Full-field ERG	40.7 (22.4–61.2)	97.4 (86.5–99.6)	0.20
Focal ERG			
Center	67.9 (47.7–84.1)	97.6 (87.4–99.6)	0.22
Sup/temp	85.7 (67.3–95.9)	97.6 (87.1–99.6)	0.23
Inf/temp	78.6 (59.0–91.7)	95.2 (83.8–99.3)	0.29
Combined	96.4 (87.7–99.6)	92.9 (87.7–99.6)	
<i>Advanced (n = 34)</i>			
Full-field ERG	69.7 (51.3–84.4)	97.4 (86.5–99.6)	0.20
Focal ERG			
Center	70.6 (52.5–84.9)	97.6 (87.4–99.6)	0.22
Sup/temp	90.9 (75.6–98.0)	95.6 (87.1–99.6)	0.23
Inf/temp	90.9 (75.6–98.0)	95.2 (83.8–99.3)	0.29
Combined	97.1 (87.7–99.6)	92.9 (87.7–99.6)	

PhNR: photopic negative response; CI: confidence interval; sup/temp: superior/temporal; inf/temp: inferior/temporal.

In patients with mild defects of the visual field, the sensitivities of the focal PhNR amplitudes were significantly higher than those of the full-field PhNR amplitudes ( $P < .01$ ) except for the inferior/temporal area. For the PhNR/b-wave amplitude ratio, the sensitivities of the focal ERG in both retinal areas were significantly higher than those of the full-field ERGs ( $P < .001$  for the center,  $P < .00001$  for the superior/temporal and inferior/temporal areas). The sensitivities of the PhNR amplitude and PhNR/b-wave amplitude ratio increased to 88.1% and 97.6%, respectively, when the combined criterion was used, and they were significantly higher than the corresponding values of the full-field PhNR ( $P < .00001$ ).

In intermediate and advanced glaucoma, the sensitivities of the focal PhNRs were generally higher than those of the full-field PhNRs. A significant difference was found between the focal and full-field PhNRs in the PhNR/b-wave amplitude ratio obtained from the superior/temporal and inferior/temporal areas in intermediate glaucoma ( $P < .01$  for the superior/temporal retinal area,  $P < .05$  for the inferior/temporal area). The sensitivities of the focal PhNR obtained by the combined criteria were significantly higher than those of the full-field PhNR in intermediate glaucoma ( $P < .05$  for the PhNR amplitude,  $P < .005$  for the PhNR/b-wave amplitude ratio).

In advanced glaucoma, there was no significant difference in the sensitivity between the full-field and focal PhNRs.

#### 4. Discussion

We compared diagnostic abilities between the full-field and focal PhNRs in detecting glaucomatous eyes. Our results demonstrated that the AUCs and sensitivities were higher for the focal PhNR than for the full-field PhNR at the early and intermediate stages of glaucoma. This suggests that the focal PhNR is a good indicator to detect the functional loss in early and intermediate glaucoma.

*4.1. Diagnostic Ability of Full-Field and Focal PhNRs.* The AUCs of the focal PhNRs were better for identifying eyes with early and intermediate glaucoma than those of the full-field PhNRs. On the other hand, there was no significant difference in the AUCs between the focal and full-field PhNRs in advanced glaucoma. When the combined criterion for the focal PhNR was used, the sensitivity increased to 88.1% and 97.6% for the focal PhNR amplitude and PhNR/b-wave amplitude ratio, respectively, even in early glaucoma, while the sensitivities for the PhNR amplitude and amplitude ratio of the full-field ERG were 38.1% and 23.8%. These findings indicate that the focal PhNR is a better indicator than the full-field PhNR in detecting functional changes in early and intermediate glaucoma.

We selected the optimal cut-off value with the highest likelihood ratio which maximally reduces false positive cases. This then kept the specificity high for both PhNR parameters. The disadvantage of the combined criterion is that it lowers the specificity as reported although a high sensitivity was obtained [18]. However, the specificity of the

PhNR of the full-field and focal ERGs could be kept over 90% by using this method to select the optimal cut-off values. Our results indicated that, even in early glaucoma, the focal PhNR had high sensitivity and specificity attained by the combined criterion.

We have reported that a curvilinear relationship existed between the retinal sensitivity (in decibels) measured by perimetry and the focal PhNR amplitude [18]. This indicated that 3 dB loss in the retinal sensitivity is approximately associated with a fifty percent decrease in the focal PhNR amplitude at the early stage of glaucoma. In fact, the largest loss of the PhNR amplitude was seen at the early stage of glaucoma in the focal ERGs (Figures 3 and 4). On the other hand, the full-field PhNR amplitude gradually reduced with advance of glaucoma. Taken together, these findings indicate that the focal PhNR could be a better measure to detect functional abnormalities at the early stage of glaucoma than the full-field PhNR.

*4.2. Disadvantages of Focal PhNR.* It is essential that the ocular fundus is visible to be able to record the focal PhNRs reliably because the stimulus areas stimulated must be monitored during the recordings using an infrared fundus camera. It is impossible to record the focal ERG in patients with dense opacities of the ocular media, such as cataracts and vitreous opacities. Furthermore, opacities of the ocular media can produce stray-light that makes the focal stimulus larger. Therefore, we have excluded patients with clinically significant cataracts that affected vision. On the other hand, the stray-light effect is negligible for the full-field ERGs. In cases with severe opacity of the ocular media, the full-field PhNRs would be more reliable than the focal PhNR.

Intersession variability is represented by the coefficients of variation ( $CV = \text{standard deviation}/\text{mean} \times 100$ ), and it was higher for the focal PhNR than for the full-field PhNR [16, 18]. In addition, variations of the PhNR amplitude among individuals were greater for the focal PhNR amplitude than for the full-field PhNR amplitude [18]. However, this disadvantage of the focal PhNR can be reduced by using the amplitude ratio of the PhNR to the b-wave amplitude [18]. Therefore, the PhNR/b-wave amplitude ratio is recommended for measuring the effectiveness of the focal ERGs.

*4.3. Limitations of the Present Study.* The recording and stimulus conditions of the focal ERG were different from those of full-field ERG, which may explain why the focal PhNR was better than the full-field PhNR in diagnosing early or intermediate glaucoma. First, we set the low cut filters at 0.5 Hz and 5 Hz for the full-field and focal ERGs, respectively. The higher cut-off frequency (5 Hz) used to record the focal PhNR was necessary to eliminate the drifts in the baseline. Thus, some of the low frequency components of the PhNR were reduced as shown in monkeys [24, 25].

Second, the full-field ERGs were elicited by red stimuli on a blue background (R/B) while the focal ERGs were elicited by white stimuli on a white background (W/W). The R/B stimuli have been shown to be a very good combination to

elicit large and reliable PhNRs [26]. Furthermore, the results of our preliminary study demonstrated that the sensitivity and specificity to discriminate glaucoma were higher for the R/B than for the W/W stimulus conditions (Machida et al., *IOVS* 2007; 48: ARVO E-Abstract 215). Thus, the stimulus conditions used in this study are more advantageous to eliciting full-field PhNRs than focal PhNRs.

Therefore, the differences in the recording and stimulus conditions do not seem to be able to explain the current results in which the focal PhNR was more sensitive than the full-field PhNR in diagnosing early and intermediate glaucoma.

## 5. Conclusions

The results of this study indicate that the PhNRs of the full-field and focal ERGs represent functional loss of RGCs in glaucoma at different stages of glaucoma. The focal ERG has the diagnostic ability with high sensitivity and specificity in detecting glaucomatous eyes at the early and intermediate stages, especially when the combined criterion is used. There was no difference in the diagnostic value between the full-field and focal PhNRs in advanced glaucoma. Thus, the focal PhNR can be a good functional parameter to detect early or intermediate glaucoma.

## Acknowledgments

This paper was supported by a Grant-in-Aid for Scientific Research C from Ministry of Education, Science, and Culture in Japan no. 20592056, Grant from Keiryokai Research Foundation no. 102, grant from The Imai Memorial Fund for Research.

## References

- [1] W. Spileers, F. Falcao-Reis, R. Smith, C. Hogg, and G. B. Arden, "The human ERG evoked by a Ganzfeld stimulator powered by red and green light emitting diodes," *Clinical Vision Sciences*, vol. 8, no. 1, pp. 21–39, 1993.
- [2] S. Viswanathan, L. J. Frishman, J. G. Robson, R. S. Harwerth, and E. L. Smith III, "The photopic negative response of the macaque electroretinogram: reduction by experimental glaucoma," *Investigative Ophthalmology and Visual Science*, vol. 40, no. 6, pp. 1124–1136, 1999.
- [3] T. Narahashi, "Chemicals as tools in the study of excitable membranes," *Physiological Reviews*, vol. 54, no. 4, pp. 813–889, 1974.
- [4] S. A. Bloomfield, "Effect of spike blockade on the receptive-field size of amacrine and ganglion cells in the rabbit retina," *Journal of Neurophysiology*, vol. 75, no. 5, pp. 1878–1893, 1996.
- [5] A. Colotto, B. Falsini, T. Salgarello, G. Iarossi, M. E. Galan, and L. Scullica, "Photopic negative response of the human ERG: losses associated with glaucomatous damage," *Investigative Ophthalmology and Visual Science*, vol. 41, no. 8, pp. 2205–2211, 2000.
- [6] S. Viswanathan, L. J. Frishman, J. G. Robson, and J. W. Walters, "The photopic negative response of the flash electroretinogram in primary open angle glaucoma," *Investigative Ophthalmology and Visual Science*, vol. 42, no. 2, pp. 514–522, 2001.
- [7] N. Drasdo, Y. H. Aldebasi, Z. Chiti, K. E. Mortlock, J. E. Morgan, and R. V. North, "The S-cone PhNR and pattern ERG in primary open angle glaucoma," *Investigative Ophthalmology and Visual Science*, vol. 42, no. 6, pp. 1266–1272, 2001.
- [8] Y. Gotoh, S. Machida, and Y. Tazawa, "Selective loss of the photopic negative response in patients with optic nerve atrophy," *Archives of Ophthalmology*, vol. 122, no. 3, pp. 341–346, 2004.
- [9] N. V. Rangaswamy, L. J. Frishman, E. U. Dorotheo, et al., "Photopic ERGs in patients with optic neuropathies: comparison with primate ERGs after pharmacological blockade of inner retina," *Investigative Ophthalmology & Visual Science*, vol. 45, pp. 3827–3837, 2004.
- [10] S. Machida, Y. Gotoh, M. Tanaka, and Y. Tazawa, "Predominant loss of the photopic negative response in central retinal artery occlusion," *American Journal of Ophthalmology*, vol. 137, no. 5, pp. 938–940, 2004.
- [11] J. Kizawa, S. Machida, T. Kobayashi, Y. Gotoh, and D. Kurosaka, "Changes of oscillatory potentials and photopic negative response in patients with early diabetic retinopathy," *Japanese Journal of Ophthalmology*, vol. 50, no. 4, pp. 367–373, 2006.
- [12] S. Ueno, M. Kondo, C.-H. Piao, K. Ikenoya, Y. Miyake, and H. Terasaki, "Selective amplitude reduction of the PhNR after macular hole surgery: ganglion cell damage related to ICG-assisted ILM peeling and gas tamponade," *Investigative Ophthalmology and Visual Science*, vol. 47, no. 8, pp. 3545–3549, 2006.
- [13] H. Chen, D. Wu, S. Huang, and H. Yan, "The photopic negative response of the flash electroretinogram in retinal vein occlusion," *Documenta Ophthalmologica*, vol. 113, no. 1, pp. 53–59, 2006.
- [14] K. Miyata, M. Nakamura, M. Kondo et al., "Reduction of oscillatory potentials and photopic negative response in patients with autosomal dominant optic atrophy with OPA1 mutations," *Investigative Ophthalmology and Visual Science*, vol. 48, no. 2, pp. 820–824, 2007.
- [15] H. Chen, M. Zhang, S. Huang, and D. Wu, "The photopic negative response of flash ERG in nonproliferative diabetic retinopathy," *Documenta Ophthalmologica*, vol. 117, no. 2, pp. 129–135, 2008.
- [16] S. Machida, Y. Gotoh, Y. Toba, A. Ohtaki, M. Kaneko, and D. Kurosaka, "Correlation between photopic negative response and retinal nerve fiber layer thickness and optic disc topography in glaucomatous eyes," *Investigative Ophthalmology and Visual Science*, vol. 49, no. 5, pp. 2201–2207, 2008.
- [17] Y. Miyake, K. Yanagida, K. Yagasaki, et al., "Subjective scotometry and recording of local electroretinogram and visual evoked response. System with television monitor of the fundus," *Japanese Journal of Ophthalmology*, vol. 25, no. 4, pp. 438–448, 1981.
- [18] S. Machida, Y. Toba, A. Ohtaki, Y. Gotoh, M. Kaneko, and D. Kurosaka, "Photopic negative response of focal electroretinograms in glaucomatous eyes," *Investigative Ophthalmology & Visual Science*, vol. 49, no. 12, pp. 5636–5644, 2008.
- [19] S. Machida, K. Tamada, T. Oikawa, et al., "Sensitivity and specificity of photopic negative response of focal electroretinograms in detecting glaucomatous eyes," *British Journal of Ophthalmology*, vol. 94, pp. 202–208, 2010.

- [20] K. Tamada, S. Machida, T. Oikawa, et al., "Correlation between photopic negative response of focal electroretinograms and local loss of retinal neurons in glaucoma," *Current Eye Research*, vol. 35, pp. 155–164, 2010.
- [21] K. Tamada, S. Machida, D. Yokoyama, and D. Kurosaka, "Photopic negative response of full-field and focal electroretinograms in patients with optic nerve atrophy," *Japanese Journal of Ophthalmology*, vol. 53, pp. 608–614, 2009.
- [22] D. R. Anderson and V. M. Patella, *Automated Static Perimetry*, Mosby, St. Louis, Mo, USA, 2nd edition, 1999.
- [23] E. R. DeLong, D. M. DeLong, and D. L. Clarke-Pearson, "Comparing the areas under two or more correlated receiver operating characteristic curves: a nonparametric approach," *Biometrics*, vol. 44, no. 3, pp. 837–845, 1988.
- [24] M. Kondo, Y. Kurimoto, T. Sakai et al., "Recording focal macular photopic negative response (PhNR) from monkeys," *Investigative Ophthalmology and Visual Science*, vol. 49, no. 8, pp. 3544–3550, 2008.
- [25] Y. Kurimoto, M. Kondo, S. Ueno, T. Sakai, S. Machida, and H. Terasaki, "Asymmetry of focal macular photopic negative responses (PhNRs) in monkeys," *Experimental Eye Research*, vol. 88, no. 1, pp. 92–98, 2009.
- [26] N. V. Rangaswamy, S. Shirato, M. Kaneko, B. I. Digby, J. G. Robson, and L. J. Frishman, "Effects of spectral characteristics of ganzfeld stimuli on the photopic negative response (PhNR) of the ERG," *Investigative Ophthalmology and Visual Science*, vol. 48, no. 10, pp. 4818–4828, 2007.

## Clinical Study

# Evaluation of Hemodynamic Parameters as Predictors of Glaucoma Progression

Ingrida Janulevičienė,<sup>1</sup> Rita Ehrlich,<sup>2</sup> Brent Siesky,<sup>2</sup> Irena Nedzelskienė,<sup>3</sup> and Alon Harris<sup>2</sup>

<sup>1</sup> Eye Clinic, Kaunas University of Medicine, Eiveniu Street 2, 50009 Kaunas, Lithuania

<sup>2</sup> Department of Ophthalmology, Glaucoma Research and Diagnostic Center, Indiana University School of Medicine, 702 Rotary Circle, Room 137, Indianapolis, IN 46202, USA

<sup>3</sup> Biostatistician, Faculty of Odontology, Kaunas University of Medicine, 50106 Kaunas, Lithuania

Correspondence should be addressed to Ingrida Janulevičienė, ingrida.januleviciene@kmuk.lt

Received 3 June 2010; Revised 17 August 2010; Accepted 15 February 2011

Academic Editor: Christopher Kai-shun Leung

Copyright © 2011 Ingrida Janulevičienė et al. This is an open access article distributed under the Creative Commons Attribution License, which permits unrestricted use, distribution, and reproduction in any medium, provided the original work is properly cited.

**Purpose.** To evaluate hemodynamic parameters as possible predictors for glaucoma progression. **Methods.** An 18-month randomized double-masked cohort study including 30 open-angle glaucoma patients receiving fixed-combination treatment with Dorzolamide/Timolol (DTFC) or Latanoprost/Timolol (LTFC) ( $n = 15$  per group) was performed. Intraocular pressure (IOP), arterial blood pressure (BP), ocular and diastolic perfusion pressures (OPP, DPP), color Doppler imaging, pulsatile ocular blood flow analysis, scanning laser polarimetry, and Humphrey visual field evaluations were included. **Results.** Both treatments showed statistically similar IOP reduction. Six patients in DTFC and 7 in LTFC group met glaucoma progression criteria. DTFC group had higher OPP, DPP, and lower vascular resistivity indices as compared to the LTFC. Progressing patients had higher nerve fiber index, lower systolic BP, OPP, DPP, higher ophthalmic and central retinal artery vascular resistance, and lower pulse volume ( $P < .05$ ;  $t$ -test). **Conclusions.** Structural changes consistent with glaucoma progression correlate with non-IOP-dependent risk factors.

## 1. Introduction

The recent series of large, multicenter, randomized clinical trials examining glaucoma treatment provide some information regarding current management goals for maintaining a target intraocular pressure (IOP). However, in many cases, glaucoma progression occurs despite maintaining target IOP. For instance, in the Collaborative Normal-Tension Glaucoma (CNTG) study, 12 to 18% of glaucoma patients progressed despite a 30% IOP reduction [1]; in the Early Manifest Glaucoma Trial (EMGT), 45% progressed despite an average IOP reduction of 25% at 6-year followup [2]. Leske et al. [3] further reported that 67% of patients progressed over 11 years of followup despite IOP reduction.

Non-IOP factors have also been identified as contributing to open-angle glaucoma (OAG) progression, including lower ocular perfusion pressure (OPP), reduced ocular blood flow, cardiovascular disease, and low systolic blood pressure. Impaired optic nerve blood flow is considered a potential

causative factor in the development of glaucoma optic neuropathy [4, 5]. However, it remains unknown whether manipulation of perfusion pressure, blood pressure, and ocular blood flow will prevent glaucoma progression.

The European Glaucoma Guidelines of 2008 [6] set the preservation of visual function as the primary goal of glaucoma therapy. In cellular terms, this can be interpreted as prevention of retinal ganglion cell death. However, the exact factors contributing to retinal ganglion cell death remain speculative [7]. Although changes in ocular blood flow might be the consequence of IOP variations, they can also be a primary physiological event [8]. As IOP therapies may influence ocular perfusion [9], it is vital to investigate glaucoma therapies for vascular interactions in addition to IOP reduction. One possible therapy is dorzolamide hydrochloride, a potent vasoactive glaucoma topical treatment that many studies have shown to increase various measures of ocular blood flow [10–16]. Although not all studies are in full agreement [17, 18], a recent

meta-analysis of published studies found carbonic anhydrase inhibitors, such as dorzolamide, to be consistently effective at increasing the ocular circulation [19].

Much less research has been conducted to investigate the effects of a combination treatment on improving ocular circulation and reducing IOP, especially in relation to glaucoma progression. To our knowledge, there are no long-term prospective double-blind studies that investigated the IOP lowering effects of fixed combinations and the correlation between ocular hemodynamic and both functional and structural changes in glaucoma patients. This study investigates the fixed combinations of dorzolamide/timolol (DTFC) and latanoprost/timolol (LTFC) on IOP lowering and glaucoma progression while examining if baseline ocular blood flow parameters are predictive of glaucomatous progression as determined by visual field and/or structural changes.

## 2. Materials and Methods

Thirty OAG patients were followed for 18 months in an observational cohort study. All subjects read and signed an informed consent, and the study was approved by the Kaunas University of Medicine institutional review board. Inclusion criteria: OAG patients with characteristic glaucomatous visual field loss, optic nerve head damage, and IOP not adequately controlled with timolol maleate (BID). Exclusion criteria: mean deviation worse than or equal to  $-12$  dB in Humphrey Visual Fields (HVFA) central 24-2 SITA Standard, cup to disc ratio equal or greater than 0.9, history of eye disease other than refractive error, orbital or ocular trauma, history of renal or hepatic disease, asthma or respiratory disease, allergy to either of the study medications, and pregnant or nursing women. After timolol baseline examination, patients were randomly assigned to double masked fixed combination treatment: LTFC or DTFC. Examinations were carried out in both eyes and the study eye was chosen randomly. All study visits were scheduled at the same time of day  $\pm 1$  hour in order to avoid diurnal fluctuations in IOP and arterial BP.

Examinations were carried out at baseline, 1, 6, 12, and 18 months of treatment, including full ophthalmic examination, visual acuity, Goldmann IOP, central corneal thickness (CCT) (OcuScan PXP Alcon Labs. Inc), Humphrey visual field examination (24-2 SITA Standard), and scanning laser polarimetry (GDx VCC Laser Diagnostic Technologies Inc., San Diego, CA). In the scanning laser polarimetry scan printout each color represents a different probability of the parameter being outside normal limits, with red having the highest probability ( $P < .005$ ), followed by yellow ( $P < .01$ ), light blue ( $P < .02$ ), and dark blue ( $P < .05$ ); green ( $P < .05$ ) refers to normal limits.

All patients had 5 or more visual fields and scanning laser polarimetry scans for analysis. Glaucoma progression was identified by (1) standard automated perimetry (SAP) as a statistically significant decrease from baseline examination in the pattern deviation values. Deepening of an existing scotoma was considered if two points in an existing scotoma declined by  $\geq 10$  dB. Expansion of an existing scotoma was considered if two contiguous points adjacent to an

existing scotoma declined by  $\geq 10$  dB. A new scotoma was diagnosed if an alteration meeting the criteria for glaucomatous visual field defect occurred in previously normal visual field location. Three or more locations with  $P < .01$  constituted a change of threshold sensitivity. (2) Progressive optic disc change is determined by optic disc assessment by ophthalmoscopy and scanning laser polarimetry. Advanced Serial Analysis detected repeatable change on two consecutive scans compared with baseline images using thickness map, and deviation map, deviation from reference map, temporal-superior-nasal-inferior-temporal (TSNIT) graph or a significant change in slope of the summary parameter chart. Each slope represented the change in RNFL thickness per year, assuming a linear trend across the followup period [3, 20–22].

Ocular blood flow was evaluated with pulsatile ocular blood flow analyser POBF (Paradigm medical industries. Inc.) and Color Doppler imaging (CDI) (Accuvix XQ. Medison Co., LTD. Seoul, Republic of Korea). Blood flow velocities were measured in the ophthalmic (OA), central retinal (CRA), and short posterior ciliary arteries (SPCA), with a 7.5 MHz linear probe calculating peak systolic velocity (PSV), end-diastolic velocity (EDV), and resistive index (RI) in each vessel. Vascular RI was originally described by Pourcelot and is calculated as  $RI = (PSV - EDV)/PSV$  [23–26].

All patients' data were collected in the Eye Clinic of Kaunas Medical University (Lithuania). CDI readings were performed by a Reading Center: the Glaucoma Research and Diagnostic Laboratories in the Department of Ophthalmology, Indiana University School of Medicine (USA).

## 3. Statistical Analysis

CDI presents 12 different parameters with a coefficient of variation ranging from 1.7% to 18%, and the majority of parameters present with a coefficient of variation under 10%. The coefficient of variation for total RNFL thickness is 5%. With a sample size of 15 in each group, we have at least 90% power to detect a change as small as 8.5% with alpha level 0.05 in retrobulbar velocities and 4.2% in RNFL thickness. The coefficient of variation for POBF is 15% [24]. In this analysis, we determined our sample size must be greater than 29.17 subjects to detect changes smaller than 9% in blood flow parameters. Changes in visual fields over time were analyzed using Humphrey's STATPAC software as described in Materials and Methods.

Descriptive statistics were obtained for the resulting measurements. In the event that significance was achieved by repeated ANOVA measurements, we applied the Fisher's and Bonferroni models. Changes in individual parameters were examined by paired Student's *t*-test. *P* values of  $P < .05$  were considered statistically significant. To test the hypothesis that the mean difference between two measurements is zero, Wilcoxon signed-ranks test was used. Changes in OBF and glaucomatous optic neuropathy parameters (functional and structural changes) were analyzed by Pearson's correlation analysis. Multivariate regression models were used to evaluate potential risk factors for glaucoma progression: age, IOP, systolic BP, diastolic BP, OPP, DPP, pulse volume, and RI of

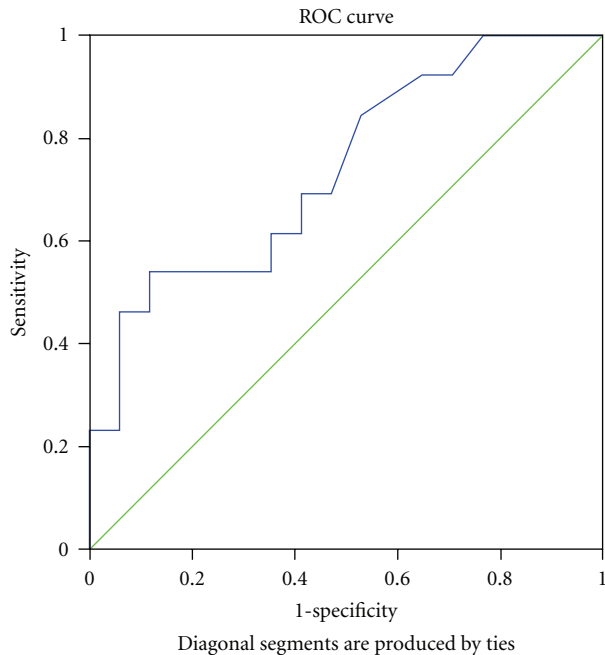


FIGURE 1: ROC curve—DPP at 18-month visit in progressing glaucoma patients. ROC: Receiver operating characteristic.

retrobulbar vessels. Receiver Operating Characteristic (ROC) curves for progressing glaucoma patients were performed to analyze the discriminating ability of possible vascular risk factors.

#### 4. Results

We examined 30 OAG patients (15 patients in each study group) with a mean age of 58.13 (SD 8.6), including 5 males and 25 females. There were no statistically significant differences between baseline parameters of either treatment group.

Both DTFC and LTFC had similar IOP lowering effect over 18 months of observation ( $P = .653$ ;  $t$ -test). Baseline systolic and diastolic BP were comparable between DTFC and LTFC groups ( $P = 0.101$  and  $P = 0.07$ , resp.,  $t$ -test). DTFC showed statistically significantly higher OPP, SPP, and DPP at 1, 6, and 18 months visits (Table 1).

CDI baseline retrobulbar blood flow parameters were similar between the two groups ( $P > .05$ ;  $t$ -test), except for a statistically significantly higher OA-PSV and CRA-EDV in the LTFC group (Table 2). Both combination treatment regimes increased retrobulbar blood flow velocities compared to baseline, though significant changes from baseline at the OA-PSV ( $P = .003$ ), OA-EDV ( $P = .001$ ), and CRA-PSV ( $P = .001$ ) were only seen in the DTFC group at 1- and 12-month followup. Vascular RI were decreased in the DTFC group, showing statistically significantly lower resistivity compared to the LTFC group in the CRA and SPCA during 12- and 18-month visits (Table 2). CRA-PSV correlated with OA-PSV ( $r = 0.505$ ;  $P = .004$ ) and OA-EDV ( $r = 0.450$ ;  $P = .013$ ), and SPCA-EDV correlated with DBP

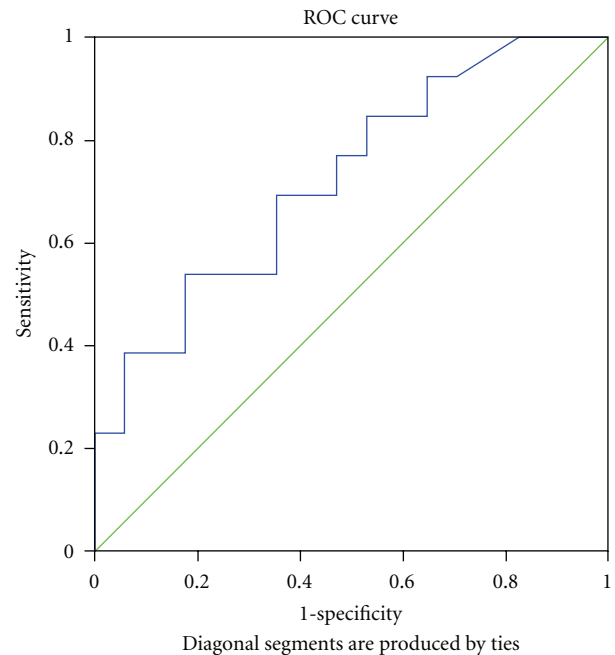


FIGURE 2: ROC curve—OPP at 18-month visit in progressing glaucoma patients. ROC: Receiver operating characteristic.

( $r = 0.454$ ;  $P = .012$ ), DPP ( $r = 0.449$ ;  $P = .013$ ), and OA-RI ( $r = -0.432$ ;  $P = .017$ ).

Average IOP, pulse amplitude, and POBF were not statistically different between treatment arms (Table 3). Pulse volume increases in the DTFC group and differences at the 12- and 18-month visits when compared to the LTFC group were significant ( $P = .025$  and  $P = .054$ , resp.).

Glaucoma progression was identified in 13 eyes (21.7%): 4 (6.7%) exhibiting structural changes, 1 (1.7%) with perimetric changes, and 8 (13.3%) showing both perimetric and structural changes. There were no statistically significant differences in IOP between progressing and stable glaucoma patients at the final visit (Table 4). Progressing glaucoma patients had higher OA RI, lower SPCA-EDV ( $P < .05$ ;  $t$ -test), and decreased pulse volume by 2.68 (SD 0.61)  $\mu\text{L}$  ( $P = .0001$ ;  $t$ -test) as compared to stable glaucoma patients at the 18-month visit. Progressing glaucoma cases had significantly lower SBP, OPP, and DPP (Table 4).

Changes in TSNIT correlated with SBP ( $r = 0.614$ ;  $P = .025$ ) in progressing glaucoma patients. The odds of higher NFI at the final 18-month visit was 13.82 times greater (95% CI 1.32–143.76) in patients with baseline CRA RI  $\geq 0.67$  ( $P = .028$ ) and older age patients (95% CI 0.90–0.99) ( $P = .021$ ).

The area under the Receiver Operating Characteristic (ROC) curve in progressing glaucoma patients with DPP  $< 62$  mmHg was 0.74 (95% CI lower bound 0.56; upper bound 0.919;  $P = .027$ ) (Figure 1); the sensitivity and specificity were 0.385 and 0.941, respectively. Progressing glaucoma patients with OPP  $< 52$  mmHg had an area under the ROC curve of 0.72 (95% CI lower bound 0.54; upper bound 0.907;  $P = .038$ ) (Figure 2); the sensitivity and specificity were

TABLE 1: Comparison of characteristics of patients treated with DTFC and LTFC.

Characteristics	DTFC	LTFC	P value ( <i>t</i> -test)
Age	56.93 (9.54)	59.33 (7.7)	.455
CCT ( $\mu$ )	548.03 (39.86)	549.65 (41.71)	.914
C/D ratio	0.62 (0.14)	0.65 (0.15)	.576
SBP mmHg baseline	157.70 (14.90)	146.70 (20.22)	.101
1 month	152.73 (16.90)	136.00 (13.67)	.006*
6 months	161.80 (18.40)*	146.800 (15.40)*	.022*
12 months	148.500 (11.18)	144.200 (17.41)	.428
18 months	158.63 (14.24)	141.10 (15.21)	.003*
DBP mmHg baseline	92.13 (8.12)	86.80 (7.53)	.073
1 month	93.73 (15.41)	81.10 (7.04)	.009*
6 months	97.43 (12.19)*	86.87 (9.49)*	.013*
12 months	91.07 (8.47)	86.57 (9.10)	.172
18 months	88.80 (5.81)	83.83 (8.41)	.070
IOP mmHg baseline	22.10 (2.69)	20.57 (3.25)	.171
1 month	16.33 (2.11)	14.90 (2.69)	.116
6 months	16.17 (2.81)	14.70 (2.57)	.147
12 months	17.10 (2.42)	15.13 (3.42)	.080
18 months	16.17 (2.08)	15.70 (3.38)	.653
OPP mmHg baseline	53.8933 (5.61)	50.6100 (7.52)	.186
1 month	59.27 (9.70)*	51.47 (4.6)*	.011*
6 months	62.93 (8.98)*	56.33 (5.84)*	.024*
12 months	56.38 (6.19)	55.38 (6.92)	.683
18 months	57.56 (3.81)	52.18 (7.26)	.019*
SPP mmHg baseline	135.60 (7.40)	126.13 (10.51)	.008*
1 month	136.40 (12.1)	121.10 (7.5)	.003*
6 months	145.63 (19.6)	132.10 (8.4)	.020*
12 months	131.4 (8.25)	129.07 (10.24)	.498
18 months	142.46 (7.4)	125.40 (9.34)	.0001*
DPP mmHg baseline	70.03 (7.40)	66.23 (8.11)	.191
1 month	77.20 (15.12)*	66.73 (5.35)*	.021*
6 months	81.33 (12.19)*	71.67 (7.95)*	.016*
12 months	73.97 (8.41)	71.43 (8.90)	.430
18 months	72.97 (6.15)	66.03 (11.03)	.045*

\*  $P < .05$  statistically significant.

DTFC: dorzolamide/timolol fixed combination; LTFC: latanoprost/timolol fixed combination; CCT: central corneal thickness; C/D ratio: clinically determined cup-disc ratio; SBP: systolic blood pressure; DBP: diastolic blood pressure; IOP: intraocular pressure; OPP: ocular perfusion pressure; DPP: diastolic perfusion pressure.

0.385 and 0.941, respectively. In our analysis, we found power 0.88 with type I error of 0.05 and, although sensitivity was low at cut off, the specificity was high.

## 5. Discussion

This observational cohort study showed that despite the IOP lowering effect with different fixed combinations (DTFC and LTFC), 13 eyes (21.7%) were considered as progressing glaucoma during 18 months of observation. Among patients with progressing glaucoma, 6 were with DTFC and 7 with LTFC treatment and showed no statistically significant

hypotensive effect between the two fixed combinations. Evidence shows that despite a wide range of glaucoma therapy options to reduce IOP, it is still difficult in some cases to control slowly progressing optic neuropathy. During our 18-month observation, no cases of intolerance were found and all patients completed the study.

Previously, Siesky et al. [27] reported that DTFC increased ocular blood flow in OAG patients while attaining a similar IOP reduction compared to a treatment of latanoprost plus timolol. Visual function, as expected, was not different in this short-term comparison. Evidence of decreased optic nerve blood flow correlating with visual field

TABLE 2: Color Doppler imaging parameters during 18 months of followup.

Characteristics		DTFC	LTFC	P value ( <i>t</i> -test)
OA_PSV (cm/s)	Baseline	23.79 (8.837)	30.86 (9.30)	.042
	1 month	37.10 (12.33)	36.04 (7.83)	.781
	6 months	38.15 (16.24)	33.87 (8.27)	.371
	12 months	40.66 (15.51)	42.50 (14.01)	.736
	18 months	33.70 (10.05)	28.71 (6.93)	.125
OA_EDV (cm/s)	Baseline	4.82 (2.47)	7.03 (3.60)	.06
	1 month	8.22 (4.22)	8.78 (3.94)	.710
	6 months	8.87 (6.03)	7.66 (2.52)	.479
	12 months	10.59 (4.79)	9.63 (5.11)	.599
	18 months	9.47 (6.19)	7.23 (4.54)	.268
OA_RI	Baseline	0.79 (0.11)	0.76 (0.11)	.437
	1 month	0.79 (0.07)	0.75 (0.11)	.158
	6 months	0.76 (0.11)	0.76 (0.09)	.986
	12 months	0.72 (0.12)	0.82 (0.17)	.046*
	18 months	0.76 (0.10)	0.87 (0.28)	.189
CRA_PSV (cm/s)	Baseline	15.09 (3.78)	17.91 (7.80)	.218
	1 month	17.78 (4.43)	18.59 (7.34)	.716
	6 months	19.08 (7.59)	17.67 (5.95)	.575
	12 months	28.88 (13.40)	22.71 (12.82)	.208
	18 months	18.69 (8.79)	17.46 (5.24)	.645
CRA_EDV (cm/s)	Baseline	4.56 (1.81)	6.33 (2.48)	.034*
	1 month	6.49 (2.22)	5.41 (3.19)	.291
	6 months	6.0 (2.49)	6.16 (2.64)	.868
	12 months	7.56 (3.67)	10.31 (7.34)	.204
	18 months	5.66 (2.80)	6.85 (3.24)	.289
CRA_RI	Baseline	0.80 (0.26)	0.81 (0.25)	.915
	1 months	0.68 (0.08)*	0.80 (0.16)*	.011*
	6 months	0.65 (0.082)	0.72 (0.19)	.192
	12 months	0.74 (0.19)	0.85 (0.19)	.000*
	18 months	0.67 (0.09)	0.93 (0.23)	.000*
SPCA_PSV (cm/s)	Baseline	15.55 (4.70)	14.50 (6.59)	.606
	1 month	15.95 (5.91)	13.38 (3.10)	.147
	6 months	20.03 (6.42)	17.92 (3.68)	.280
	12 months	21.01 (10.40)	19.81 (7.04)	.715
	18 months	13.69 (5.45)	11.03 (2.83)	.104
SPCA_EDV (cm/s)	Baseline	4.42 (2.29)	14.50 (6.59)	.973
	1 month	4.69 (2.28)	3.31 (2.11)	.095
	6 months	6.10 (2.16)	5.47 (2.22)	.442
	12 months	6.04 (2.67)*	3.43 (2.26)*	.007*
	18 months	4.39 (1.85)	3.87 (1.17)	.366
SPCA_RI	Baseline	0.71 (0.06)	0.79 (0.28)	.232
	1 month	0.75 (0.08)	0.79 (0.10)	.229
	6 months	0.69 (0.06)	0.69 (0.11)	.969
	12 months	0.70 (0.07)*	0.90 (0.27)*	.011*
	18 months	0.69 (0.11)*	0.85 (0.30)*	.015*

\*  $P < .05$  statistically significant.

DTFC: dorzolamide/timolol fixed combination; LTFC: latanoprost/timolol fixed combination; OA: ophthalmic artery; CRA: central retinal artery; SPCA: short posterior ciliary artery, PSV: peak systolic velocity; EDV: end diastolic velocity; RI: resistive index.

TABLE 3: Pulsatile ocular blood flow parameters.

Characteristics		DTFC	LTFC	P value
IOP average (mmHg)	baseline	19.58 (3.68)	20.96 (3.78)	.320
	1 month	17.12 (3.25)	18.01 (2.83)	.429
	6 months	17.67 (3.73)	17.71 (3.17)	.975
	12 months	17.87 (3.59)	16.48 (2.56)	.231
	18 months	16.10 (2.78)	15.23 (4.61)	.539
Pulse amplitude	Baseline	4.17 (1.50)	4.73 (1.58)	.335
	1 month	3.91 (0.88)	3.95 (1.18)	.917
	6 months	4.93 (1.88)	4.12 (1.47)	.201
	12 months	4.75 (1.40)	4.67 (1.74)	.891
	18 months	4.73 (2.78)	4.51 (1.42)	.675
Pulse volume ( $\mu\text{L}$ )	Baseline	7.19 (2.36)	7.81 (2.68)	.507
	1 month	7.99 (2.27)	7.60 (2.40)	.648
	6 months	8.91 (2.23)	7.07 (3.26)	.417
	12 months	9.25 (1.95)*	6.93 (3.20)*	.025*
	18 months	9.29 (2.39)*	7.82 (1.55)	.054*
POBF Baseline ( $\mu\text{L/s}$ )	Baseline	16.81 (4.53)	17.57 (6.13)	.702
	1 month	19.12 (4.45)	18.52 (5.48)	.754
	6 months	19.43 (4.54)	18.63 (6.21)	.69
	12 months	20.87 (4.45)	18.43 (6.51)	.242
	18 months	21.33 (2.74)	19.75 (5.61)	.336

\*  $P < .05$  statistically significant.

DTFC: dorzolamide/timolol fixed combination; LTFC: latanoprost/timolol fixed combination; IOP: intraocular pressure; POBF: pulsatile ocular blood flow.

damage has been reported in glaucoma patients [28–33]. In our study, we report differences in OPP and DPP between DTFC and LTFC; however, no significant differences were observed between LTFC and DTFC in terms of glaucoma progression during the 18-month followup.

Previous studies examining ocular blood flow and glaucoma progression reported structural abnormalities [34] preceding visual field damage. Hafez et al. [35] also concluded that rim perfusion might be reduced before manifestation of visual field defects. Several studies have shown abnormal retrobulbar vasculature in eyes with Glaucomatous Optic Neuropathy (GON) [36–40]. Satilmis et al. [41] showed that progression rate of glaucomatous visual field damage correlates with retrobulbar hemodynamic variables. Zeitz et al. [42] further showed that progressive glaucoma is associated with decreased blood flow velocities in the small retrobulbar vessels supplying the optic nerve head. We found increased blood flow velocities with combination treatment as compared to timolol baseline. DTFC arm had statistically significantly lower baseline OA-PSV and CRA-EDV as compared to LTFC baseline. After 1, 6, 12, and 18 months of combination treatment, the velocities in retrobulbar vessels increased as compared to baseline, but differences in velocities between two treatment arms were not statistically significant. In our study, SPCA-EDV was lower in progressing glaucoma patients as compared to stable glaucoma patients. We found statistically significant differences in RIs between the two treatment cohorts. DTFC showed statistically significant decrease in CRA and SPCA

RIs at 12- and 18-month visits as compared to LTFC. Nielsen and Nyborg [43] found that PG F2 $\alpha$  induces constriction in isolated bovine aqueous veins. Remky et al. [44] reported that reduction in retinal vessel diameters may account for an increase in retinal vascular resistance. An increase in vascular resistance might be related to vasoconstriction or vasospasm, vasosclerosis, reduction of the vessel diameters, or rheological factors leading to decreased volumetric flow. In our study, POBF that measures pulse volume was significantly higher in DTFC at 12 and 18-month visits compared to LTFC. Progressing glaucoma patients had 2.675 (SD 0.61)  $\mu\text{L}$  lower pulse volume when compared to stable glaucoma cases ( $P = .0001$ ). Our results indicate DTFC indeed increases markers of ocular blood flow and perfusion compared to LTFC but with no difference in possible markers of glaucoma progression during the followup period. Longer duration studies may be required to differentiate any possible (or lack thereof) ocular blood flow benefits.

The Beaver Dam study reported a positive correlation between systolic BP and IOP [45]. The Los Angeles Latino Eye Study [46] showed high systolic BP, low diastolic BP, and low OPP as risk factors for glaucoma progression. Data from EMGT [3] pointed to low systolic BP as a long-term predictor for glaucoma progression. Further, data from Thessaloniki Eye study [47] suggested BP status as an important independent factor initiating optic disc changes and/or as a contributing factor to glaucoma damage. In our study, we found no fluctuations or rise in IOP, but OPP and DPP at 1, 6, and 18-month visits were statistically

TABLE 4: Comparison of means between progressing and stable glaucoma patients at 18 months visit.

Parameter at 18 month	Mean in stable glaucoma patients (St. deviation)	Mean in progressing glaucoma patients (St. deviation)	P value ( <i>t</i> -test)
IOP	15.32 (2.46)	16.73 (3.04)	.171
IOP/POBF	14.73 (3.5)	16.88 (3.89)	.123
MD (dB)	-1.06 (2.30)	-2.01 (2.13)	.257
PSD (dB)	2.05 (2.53)	2.90 (2.41)	.360
TSNIT ( $\mu$ )	53.59 (5.28)	50.96 (7.10)	.254
NFI	23.82 (2.36)	27.69 (3.29)	.0008*
SBP (mmHg)	151.50 (14.04)	147.73 (20.66)	.55
DBP (mmHg)	88.44 (6.42)	83.53 (8.23)	.077
OPP (mmHg)	57.19 (4.73)	51.84 (7.00)	.019*
DPP (mmHg)	73.06 (6.57)	64.85 (8.82)	.007*
OA_PSV	32.26 (3.15)	29.82 (3.28)	.048
OA_EDV	9.19 (4.98)	7.25 (2.01)	.197
OA_RI	0.74 (0.07)	0.90 (0.07)	<.0001*
CRA_PSV	19.96 (7.36)	15.61 (6.28)	.099
CRA_EDV	6.66 (3.19)	5.73 (2.85)	.415
CRA_RI	0.79 (0.08)	0.815 (0.06)	.35
SPCA_PSV	13.08 (5.11)	11.42 (3.43)	.321
SPCA_EDV	4.73 (1.71)	3.34 (0.83)	.011*
SPCA_RI	0.77 (0.20)	0.76 (0.20)	.893
AMPLITUDE	4.62 (1.48)	4.62 (1.44)	.985
PULSE VOLUME	9.71 (2.01)	7.03 (1.00)	.0001*
POBF	21.25 (4.22)	19.60 (4.60)	.316

DTFC: dorzolamide/timolol fixed combination; LTFC: latanoprost/timolol fixed combination; MD: mean deviation; PSD: pattern standard deviation; TSNIT: temporal, superior, nasal, inferior, temporal average; NFI: nerve fiber index. POBF: pulsatile ocular blood flow.

significantly higher in the DTFC group. The LTFC group had lower SBP at 1, 6, and 18-month visits and diastolic BP at 1 and 6 month visits ( $P < .05$ ; *t*-test). Progressing patients had statistically significantly lower systolic BP, OPP, and DPP when compared to stable glaucoma cases. Calculating the magnitude of changes in OPP and DPP parameters compared to baseline values, we found them to be decreasing in 69.2% of progressing glaucoma cases. Our calculated sensitivity of decreased DPP was 0.7 and specificity 0.8.

BP and ocular perfusion pressure tend to exhibit fluctuations during the day and night. Importantly, Choi et al. [48] reported that mean BP and OPP fluctuations were associated with reduced TSNIT and increased NFI. In our study, BP was measured at the same time of the day during all visits and statistically significant differences in BP and OPP parameters were seen at 1, 6, and 18 months but were not significant at 12 months between the two treatment groups. The LTFC group showed lower OPP and DPP and higher NFI as compared to DTFC at the 18 month visit (mean difference 7.80 (SD 3.69) ( $P = .046$ ). Accordingly, progressing glaucoma patients showed lower OPP and DPP and higher NFI (mean difference 8.87 (SD 3.94));  $P = .056$ ). Yet, despite differences in the nonpressure-related parameters, we found no difference in the percent of progression between the treatment groups. In addition, we also found a strong positive correlation between TSNIT average and BP and OPP

parameters at 18-month visit. Interestingly, low OPP and DPP in progressing glaucoma patients had low sensitivity but rather high specificity. In our analysis, statistically significant Area Under ROC Curve (AUC) values were reported at 0.74 and 0.72. While significant, these values should be further validated with a larger sample allowing for stratification into classified percentile ranges. The odds of higher NFI at the final 18-month visit was nearly 14 times greater in patients with higher than 0.67 baseline CRA RI ( $P = .028$ ) and older age ( $P = .021$ ).

Current glaucoma medications are targeted to decrease the IOP and are not targeted to treat other hemodynamic parameters. In our study, we found some differences in structural outcomes between the two combination treatment regimes and according differences in BP, OPP, CRA, and SPCA RIs. Our study is a preliminary study and the data presented needs to be interpreted with caution. Increased resistance to flow in small retrobulbar vessels supplying the optic nerve is probably related to glaucoma progression, although this requires confirmation in larger longitudinal studies.

Possible limitations of the current study include the difficulty in defining glaucoma progression and specific limitations in each imaging technology used to assess ocular blood flow. We have matched markers of possible glaucoma progression, which may indicate but not actually represent

glaucomatous progression. While the parameters may be associated with progression, they are not necessarily good in predicting progression. A risk factor must be strongly associated with a disorder to be a worthwhile screening test, and it is not unusual for a strong risk factor to fail to be a good screening tool. Larger group studies with longer followup, standardization of measurement techniques for glaucoma progression, and ocular blood flow parameters are required to elicit a clear understanding of vascular risk factors in glaucoma progression.

### Conflict of Interests

The authors have no proprietary interest in any aspect of the products or devices mentioned herein.

### Acknowledgement

This work is supported in part by an unrestricted grant from Research to Prevent Blindness. I. Janulevičienė and A. Harris have each previously received research grants from Merck & Co, Inc., Whitehouse Station, NJ.

### References

- [1] S. Drange, D. R. Anderson, and M. Schulzer, "Risk factors for progression of visual field abnormalities in normal-tension glaucoma," *American Journal of Ophthalmology*, vol. 131, no. 6, pp. 699–708, 2001.
- [2] A. Heijl, M. C. Leske, B. Bengtsson, L. Hyman, B. Bengtsson, and M. Hussein, "Reduction of intraocular pressure and glaucoma progression: results from the Early Manifest Glaucoma Trial," *Archives of Ophthalmology*, vol. 120, no. 10, pp. 1268–1279, 2002.
- [3] M. C. Leske, A. Heijl, L. Hyman, B. Bengtsson, L. Dong, and Z. Yang, "Predictors of long-term progression in the early manifest glaucoma trial," *Ophthalmology*, vol. 114, no. 11, pp. 1965–1972, 2007.
- [4] J. Flammer, "The vascular concept of glaucoma," *Survey of Ophthalmology*, vol. 38, no. 1, pp. S3–S6, 1994.
- [5] S. S. Hayreh, "Progress in the understanding of the vascular etiology of glaucoma," *Current Opinion in Ophthalmology*, vol. 5, no. 2, pp. 26–35, 1994.
- [6] European Glaucoma Society, *Terminology and Guidelines for Glaucoma*, Editrice DOGMA S.r.l., Savona, Italy, 3rd edition, 2008.
- [7] N. N. Osborne, M. Ugarte, M. Chao et al., "Neuroprotection in relation to retinal ischemia and relevance to glaucoma," *Survey of Ophthalmology*, vol. 43, no. 6, pp. S102–S128, 1999.
- [8] B. Siesky, A. Harris, N. Kheradiya, C. Rospigliosi, L. McCranor, and R. Ehrlich, "The clinical significance of vascular factors in glaucoma," *Journal of Current Glaucoma Practice*, vol. 2, pp. 12–17, 2007.
- [9] V. P. Costa, A. Harris, E. Stefánsson et al., "The effects of antiglaucoma and systemic medications on ocular blood flow," *Progress in Retinal and Eye Research*, vol. 22, no. 6, pp. 769–805, 2003.
- [10] A. Harris, O. Arend, S. Arend, and B. Martin, "Effects of topical dorzolamide on retinal and retrobulbar hemodynamics," *Acta Ophthalmologica Scandinavica*, vol. 74, no. 6, pp. 569–572, 1996.
- [11] A. Martinez, F. Gonzalez, C. Capeans, R. Perez, and M. Sanchez-Salorio, "Dorzolamide effect on ocular blood flow," *Investigative Ophthalmology & Visual Science*, vol. 40, no. 6, pp. 1270–1275, 1999.
- [12] A. Harris, O. Arend, L. Kagemann, M. Garrett, H. S. Chung, and B. Martin, "Dorzolamide, visual function and ocular hemodynamics in normal-tension glaucoma," *Journal of Ocular Pharmacology and Therapeutics*, vol. 15, no. 3, pp. 189–197, 1999.
- [13] A. Harris, O. Arend, H. S. Chung, L. Kagemann, L. Cantor, and B. Martin, "A comparative study of betaxolol and dorzolamide effect on ocular circulation in normal-tension glaucoma patients," *Ophthalmology*, vol. 107, no. 3, pp. 430–434, 2000.
- [14] A. Harris, C. P. Jonescu-Cuypers, L. Kagemann et al., "Effect of dorzolamide timolol combination versus timolol 0.5% on ocular bloodflow in patients with primary open-angle glaucoma," *American Journal of Ophthalmology*, vol. 132, no. 4, pp. 490–495, 2001.
- [15] A. M. Avunduk, A. Sari, N. Akyol et al., "The one-month effects of topical betaxolol, dorzolamide and apraclonidine on ocular blood flow velocities in patients with newly diagnosed primary open-angle glaucoma," *Ophthalmologica*, vol. 215, no. 5, pp. 361–365, 2001.
- [16] A. S. Bernd, L. E. Pillunat, A. G. Böhm, K. G. Schmidt, and G. Richard, "Okuläre hämodynamik und Gesichtsfeld beim Glaukom unter Dorzolamid-Therapie," *Ophthalmologe*, vol. 98, no. 5, pp. 451–455, 2001.
- [17] L. E. Pillunat, A. G. Böhm, A. U. Köller, K. G. Schmidt, M. Klemm, and G. Richard, "Effect of topical dorzolamide on optic nerve head blood flow," *Graefes Archive for Clinical and Experimental Ophthalmology*, vol. 237, no. 6, pp. 495–500, 1999.
- [18] I. C. Bergstrand, A. Heijl, and A. Harris, "Dorzolamide and ocular blood flow in previously untreated glaucoma patients: a controlled double-masked study," *Acta Ophthalmologica Scandinavica*, vol. 80, no. 2, pp. 176–182, 2002.
- [19] B. Siesky, A. Harris, E. Brizendine et al., "Literature review and meta-analysis of topical carbonic anhydrase inhibitors and ocular blood flow," *Survey of Ophthalmology*, vol. 54, no. 1, pp. 33–46, 2009.
- [20] F. A. Medeiros, L. M. Alencar, L. M. Zangwill et al., "Detection of progressive retinal nerve fiber layer loss in glaucoma using scanning laser polarimetry with variable corneal compensation," *Investigative Ophthalmology & Visual Science*, vol. 50, no. 4, pp. 1675–1681, 2009.
- [21] L. M. Alencar, L. M. Zangwill, R. N. Weinreb et al., "A comparison of rates of change in neuroretinal rim area and retinal nerve fiber layer thickness in progressive glaucoma," *Investigative Ophthalmology & Visual Science*, vol. 51, no. 7, pp. 3531–3539, 2010.
- [22] I. Janulevičienė, R. Ehrlich, B. Siesky, I. Nedzelskienė, and A. Harris, "Visual function, optic nerve structure, and ocular blood flow parameters after 1 year of glaucoma treatment with fixed combinations," *European Journal of Ophthalmology*, vol. 19, no. 5, pp. 790–797, 2009.
- [23] T. H. Williamson and A. Harris, "Color Doppler ultrasound imaging of the eye and orbit," *Survey of Ophthalmology*, vol. 40, no. 4, pp. 255–267, 1996.
- [24] L. Pourcelot, "Applications of cliniques de l'examen Doppler transcutané," *INSERM*, vol. 34, pp. 213–240, 1974.
- [25] L. Pourcelot, "Indications of Doppler ultrasonography in the study of peripheral vessels," *Revue du Praticien*, vol. 25, no. 59, pp. 4671–4680, 1975.

- [26] T. A. Ciula, C. D. Regillo, and A. Harris, *Retina and Optic Nerve Imaging*, Lippincot Williams Wilkins, Philadelphia, Pa, USA, 2003.
- [27] B. Siesky, A. Harris, D. Sines et al., "A comparative analysis of the effects of the fixed combination of timolol and dorzolamide versus latanoprost plus timolol on ocular hemodynamics and visual function in patients with primary open-angle glaucoma," *Journal of Ocular Pharmacology and Therapeutics*, vol. 22, no. 5, pp. 353–361, 2006.
- [28] J. E. Grunwald, J. Piltz, S. M. Hariprasad, and J. DuPont, "Optic nerve and choroidal circulation in glaucoma," *Investigative Ophthalmology & Visual Science*, vol. 39, no. 12, pp. 2329–2336, 1998.
- [29] G. Michelson, M. J. Langhans, J. Harazny, and A. Dichtl, "Visual field defect and perfusion of the juxtapapillary retina and the neuroretinal rim area in primary open-angle glaucoma," *Graefes Archive for Clinical and Experimental Ophthalmology*, vol. 236, no. 2, pp. 80–85, 1998.
- [30] S. S. Hayreh, I. H. Revie, and J. Edwards, "Vasogenic origin of visual field defects and optic nerve changes in glaucoma," *British Journal of Ophthalmology*, vol. 54, no. 7, pp. 461–472, 1970.
- [31] K. Yaeoda, M. Shirakashi, A. Fukushima et al., "Relationship between optic nerve head microcirculation and visual field loss in glaucoma," *Acta Ophthalmologica Scandinavica*, vol. 81, no. 3, pp. 253–259, 2003.
- [32] M. T. Nicoleta, S. M. Drance, S. J. A. Rankin, A. R. Buckley, and B. E. Walman, "Color Doppler imaging in patients with asymmetric glaucoma and unilateral visual field loss," *American Journal of Ophthalmology*, vol. 121, no. 5, pp. 502–510, 1996.
- [33] Y. Yamazaki and S. M. Drance, "The relationship between progression of visual field defects and retrobulbar circulation in patients with glaucoma," *American Journal of Ophthalmology*, vol. 124, no. 3, pp. 287–295, 1997.
- [34] A. Sommer, J. Katz, H. A. Quigley et al., "Clinically detectable nerve fiber atrophy precedes the onset of glaucomatous field loss," *Archives of Ophthalmology*, vol. 109, no. 1, pp. 77–83, 1991.
- [35] A. S. Hafez, R. L. G. Bizarro, and M. R. Lesk, "Evaluation of optic nerve head and peripapillary retinal blood flow in glaucoma patients, ocular hypertensives, and normal subjects," *American Journal of Ophthalmology*, vol. 136, no. 6, pp. 1022–1031, 2003.
- [36] Y. Yamazaki and F. Hayamizu, "Comparison of flow velocity of ophthalmic artery between primary open angle glaucoma and normal tension glaucoma," *British Journal of Ophthalmology*, vol. 79, no. 8, pp. 732–734, 1995.
- [37] M. T. Nicoleta, B. E. Walman, A. R. Buckley, and S. M. Drance, "Ocular hypertension and primary open-angle glaucoma: a comparative study of their retrobulbar blood flow velocity," *Journal of Glaucoma*, vol. 5, no. 5, pp. 308–310, 1996.
- [38] S. J. A. Rankin, B. E. Walman, A. R. Buckley, and S. M. Drance, "Color Doppler imaging and spectral analysis of the optic nerve vasculature in glaucoma," *American Journal of Ophthalmology*, vol. 119, no. 6, pp. 685–693, 1995.
- [39] P. Rojanapongpun, S. M. Drance, and B. J. Morrison, "Ophthalmic artery flow velocity in glaucomatous and normal subjects," *British Journal of Ophthalmology*, vol. 77, no. 1, pp. 25–29, 1993.
- [40] H. J. Kaiser, A. Schoetzau, D. Stumpfig, and J. Flammer, "Blood-flow velocities of the extraocular vessels in patients with high-tension and normal-tension primary open-angle glaucoma," *American Journal of Ophthalmology*, vol. 123, no. 3, pp. 320–327, 1997.
- [41] M. Satilmis, S. Orgül, B. Doubler, and J. Flammer, "Rate of progression of glaucoma correlates with retrobulbar circulation and intraocular pressure," *American Journal of Ophthalmology*, vol. 135, no. 5, pp. 664–669, 2003.
- [42] O. Zeitz, P. Galambos, L. Wagenfeld et al., "Glaucoma progression is associated with decreased blood flow velocities in the short posterior ciliary artery," *British Journal of Ophthalmology*, vol. 90, no. 10, pp. 1245–1248, 2006.
- [43] P. J. Nielsen and N. C. B. Nyborg, "Effects of prostaglandins in bovine isolated aqueous veins," *Investigative Ophthalmology & Visual Science*, vol. 37, no. 3, p. S843, 1996.
- [44] A. Remky, N. Plange, J. Klok, and O. Arend, "Retinal arterial diameters in patients with glaucoma," *Spektrum der Augenheilkunde*, vol. 18, no. 1, pp. 25–30, 2004.
- [45] B. E. K. Klein, R. Klein, and M. D. Knudtson, "Intraocular pressure and systemic blood pressure: longitudinal perspective: the Beaver Dam Eye Study," *British Journal of Ophthalmology*, vol. 89, no. 3, pp. 284–287, 2005.
- [46] V. Doshi, M. Ying-Lai, S. P. Azen, and R. Varma, "Sociodemographic, family history, and lifestyle risk factors for open-angle glaucoma and ocular hypertension. the Los Angeles Latino eye study," *Ophthalmology*, vol. 115, no. 4, pp. 639–647, 2008.
- [47] F. Topouzis, A. L. Coleman, A. Harris et al., "Association of blood pressure status with the optic disk structure in non-glaucoma subjects: the Thessaloniki Eye Study," *American Journal of Ophthalmology*, vol. 142, no. 1, pp. 60–67, 2006.
- [48] J. Choi, K. H. Kim, J. Jeong, H. S. Cho, C. H. Lee, and M. S. Kook, "Circadian fluctuation of mean ocular perfusion pressure is a consistent risk factor for normal-tension glaucoma," *Investigative Ophthalmology & Visual Science*, vol. 48, no. 1, pp. 104–111, 2007.

## Review Article

# Multiphoton Microscopy for Ophthalmic Imaging

Emily A. Gibson,<sup>1</sup> Omid Masihzadeh,<sup>2,3</sup> Tim C. Lei,<sup>2</sup> David A. Ammar,<sup>3</sup> and Malik Y. Kahook<sup>3</sup>

<sup>1</sup> Department of Bioengineering, University of Colorado Denver, Denver, 12700 E. 19th Ave, Mail Stop 8607, Aurora, CO 80045, USA

<sup>2</sup> Department of Electrical Engineering, University of Colorado Denver, Denver, CO 80217, USA

<sup>3</sup> Department of Ophthalmology, School of Medicine, University of Colorado, 1675 Aurora Ct, Mail Stop F-731, Aurora, CO 80045, USA

Correspondence should be addressed to Malik Y. Kahook, malik.kahook@gmail.com

Received 5 July 2010; Revised 6 September 2010; Accepted 26 October 2010

Academic Editor: Christopher Leung

Copyright © 2011 Emily A. Gibson et al. This is an open access article distributed under the Creative Commons Attribution License, which permits unrestricted use, distribution, and reproduction in any medium, provided the original work is properly cited.

We review multiphoton microscopy (MPM) including two-photon autofluorescence (2PAF), second harmonic generation (SHG), third harmonic generation (THG), fluorescence lifetime (FLIM), and coherent anti-Stokes Raman Scattering (CARS) with relevance to clinical applications in ophthalmology. The different imaging modalities are discussed highlighting the particular strength that each has for functional tissue imaging. MPM is compared with current clinical ophthalmological imaging techniques such as reflectance confocal microscopy, optical coherence tomography, and fluorescence imaging. In addition, we discuss the future prospects for MPM in disease detection and clinical monitoring of disease progression, understanding fundamental disease mechanisms, and real-time monitoring of drug delivery.

## 1. Introduction

Imaging modalities such as digital photography and ultrasound have become integral in the clinical and surgical practice of ophthalmology over the past few decades. More recently, diode laser-based imaging devices such as GDx (Carl Zeiss Meditec, Inc., Dublin, CA), Heidelberg Retinal Tomography (HRT, Heidelberg Engineering, Heidelberg, Germany), and optical coherence tomography (OCT) have become invaluable in the examination and early diagnosis of disease ranging from macular degeneration to glaucoma. Despite these advances, the aforementioned imaging devices are restricted in their ability to image tissue structure while being largely unable to elucidate tissue function. This limitation becomes even more important when noting that the structural normative databases used to delineate abnormal from normal tissue have inherent limitations. Physiologic differences from patient to patient as well as coexisting conditions, such as possible thinning of the retinal nerve fiber layer (RNFL) in high myopia, may alter the structure of tissues but often do not alter actual visual function [1].

An imaging modality that could combine both structural and functional imaging would allow physicians to make more informed decisions that directly relate to disruptions in visual performance.

Multiphoton microscopy (MPM) has found increasing use in laboratory-based biomedical imaging due to its subcellular resolution along with the ability to obtain structural and functional information. These properties make MPM unique compared to other imaging modalities such as ultrasound, magnetic resonance imaging (MRI), or X-ray/computed tomography (CT) imaging. However, to achieve these benefits, there is a drawback in the limited tissue penetration depth as well as the ability to image highly scattering tissues such as sclera. Fortunately, there are opportunities for using optical imaging in the eye because of the transparency of the cornea, lens, and vitreous humor to visible and infrared light. In this paper, we review current research on MPM imaging of the eye and discuss future possibilities for applications to early disease diagnosis and monitoring of patient treatment outcomes.

## 2. Multiphoton Microscopy: Theory and Implementation

*2.1. Overview of Multiphoton Microscopy.* Multiphoton microscopy has been described in depth in many review articles and texts [2–7]. Here, we highlight some of the key features of MPM that would have application in clinical *in vivo* measurements. MPM is an imaging method based on nonlinear optical response of a medium, that is, processes that involve more than one photon interacting simultaneously with a molecule. Since the probability of simultaneous interactions with two (or more) photons is extremely low (cross-sections on order of  $10^{-50}$  cm<sup>4</sup> s or 1 GM), the process only occurs when there is high photon flux (on the order of  $10^6$ – $10^8$  W/cm<sup>2</sup>) [2, 8]. This is typically achieved using a pulsed near-infrared laser with a pulse duration on order of  $\sim 100$  femtoseconds focused with a high numerical aperture objective. As a result, MPM offers intrinsic axial cross-sectioning because the process only occurs at the focus of the microscope objective, where the laser intensity is greatest. MPM imaging offers equivalent resolution as confocal microscopy ( $\sim 200$  nm lateral and  $\sim 1.0$  micron axial) but does not require the use of a pinhole. Image acquisition times are similar to confocal microscopy, with an image of  $256 \times 256$  pixels acquired at video rate. The acquisition time is comparable to OCT with a difference in that MPM provides subcellular resolution within a smaller-imaged region while OCT scans over a larger area with reduced resolution. It is important to realize, for applications in medicine, that MPM can provide contrast without exogenous dye labeling and is a completely noninvasive technique.

An additional advantage of using a near-infrared laser source is deeper tissue penetration due to reduced light scattering with longer wavelengths of light. The imaging depth possible depends upon the type of tissue and the wavelength of the laser. Imaging depths of up to 1 mm have been reported in brain tissue by using higher laser powers from a Ti:sapphire regenerative amplifier at 800 nm [9]. More sophisticated methods for deeper image penetration employ adaptive wavefront correction, similar to the technology used by astronomers in ground-based telescopes. Analogous to the distortion of the image quality due to the atmosphere, in deep tissue MPM, the local inhomogeneities in refractive index in tissue distort the focus of the excitation laser, causing a reduction in signal. A deformable mirror or spatial light modulator can be incorporated before the objective to precompensate for the wavefront distortion leading to a diffraction-limited focal spot size in tissue depths of  $500 \mu\text{m}$  [10–12].

MPM includes two-photon excitation fluorescence (2PEF), second harmonic generation (SHG), and third harmonic generation (THG), as well as coherent anti-Stokes Raman Scattering (CARS) described in a later section. Figure 1 shows a schematic of the different processes that result from nonlinear multiphoton interactions with a molecule. 2PEF is very similar to traditional fluorescence, except that two photons of a lower energy are simultaneously absorbed to excite a fluorophore. When 2PEF is used to excite

TABLE 1: Optimal imaging contrast mechanism for different biological molecules.

Compound	Imaging technique (excitation/emission wavelengths)
NAD(P)H	2PAF/FLIM (excitation 700–730 nm/emission peak 460 nm) [16]
FAD	2PAF/FLIM (excitation 700–900 nm/emission peak 525 nm) [16]
Elastin	2PAF (excitation 700–740 nm/emission peak 400 nm) [15, 19]
Collagen	SHG (SHG excitation is tunable/emission at one-half the excitation wavelength) [15]
Lipids	THG/CARS (THG excitation is tunable with emission at one-third the excitation wavelength) [14]

endogenous fluorophores such as elastin and NAD(P)H, it is typically called two-photon excitation autofluorescence (2PAF). A fluorophore is any molecule that can absorb photons and emit the energy as a photon with a red-shifted wavelength. Another nonlinear process that occurs with two-photon excitation is second harmonic generation (SHG). SHG can only occur when light interacts with noncentrosymmetric (asymmetric) macromolecular structures. Molecules such as collagen fibers can simultaneously “scatter” two lower-energy photons as a single photon of twice the energy. Third harmonic generation is analogous to SHG; however, in this case, three photons of the fundamental are upconverted to a single photon of three times the energy. THG only requires about ten times the photon flux as SHG and, therefore, can be a useful tool for imaging. THG highlights different features of a sample than SHG because it is generated at the interface of media with differing third-order nonlinear susceptibilities,  $\chi^{(3)}$  [13, 14].

Endogenous fluorophores have varying two-photon cross-sections as a function of wavelength and have been measured and reported [15, 16]. The center wavelength of a Ti:sapphire laser can be tuned over a large spectral range from 700 to 1050 nm, making it an extremely useful source for two-photon autofluorescence excitation. In this manner, different compounds in tissue can be highlighted by tuning the excitation wavelength. For example, the two-photon cross-sections of many endogenous fluorophores peak below 700 nm and decrease at higher wavelengths, while SHG emission remains strong at longer wavelengths from 900 to 1000 nm [15]. By tuning the excitation laser to longer wavelengths, collagen structures in tissue can be distinguished from autofluorescence [17, 18]. In another example of the utility of excitation wavelength tuning, NAD(P)H was distinguished from FAD by dual wavelength excitation at 730 nm (where both compounds are excited) and at 900 nm (where FAD is exclusively excited, while NAD(P)H has a negligible two-photon cross-section) [16]. Table 1 gives a list of endogenous fluorophores and tissue structures and the imaging technique that provides the best contrast mechanism.

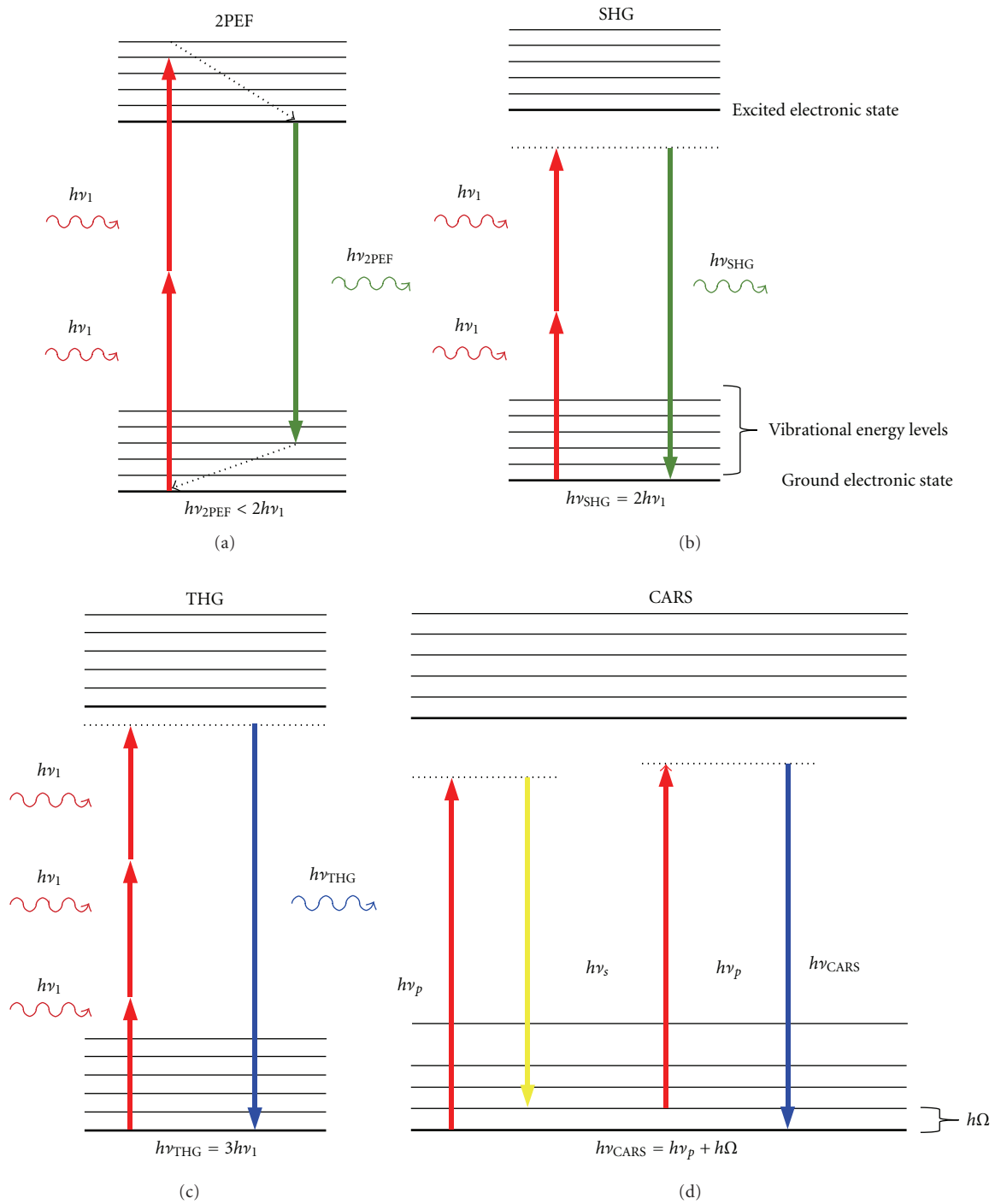


FIGURE 1: Jablonski diagram showing the interaction of multiple infrared photons with the electronic and vibrational energy levels of a molecule. (a) In two-photon excitation fluorescence (2PEF), the molecule absorbs two infrared photons that promote it to the excited electronic state. After relaxation to a lower vibrational level, the molecule emits a lower energy (red-shifted) photon. (b) In second harmonic generation (SHG), two infrared photons are instantaneously upconverted to a single photon of twice the energy. (c) In third harmonic generation (THG), three infrared photons are instantaneously upconverted to a single photon of thrice the energy. (d) In Coherent anti-Stokes Raman Scattering (CARS), two photons with energies  $h\nu_p$  and  $h\nu_s$  coherently excite the vibrational level with energy  $h\Omega = h\nu_p - h\nu_s$ . An additional photon,  $h\nu_p$ , interacts with the vibrationally excited molecule emitting a photon with energy given by the original incident photon energy plus the vibrational energy,  $h\nu_{CARS} = h\nu_p + h\Omega$ , leaving the molecule in its original ground state. (Note that photon energy is given by Planck's constant,  $h$ , multiplied by the frequency of the photon  $\nu$ .)

**2.2. Optical Instrumentation.** Both 2PAF and SHG can be simultaneously measured using the same optical setup since the SHG signal occurs at a distinct wavelength (exactly half the excitation wavelength) and can be separated from autofluorescence using spectral filtering. Figure 2 shows a schematic of a typical setup for performing MPM. The apparatus consists of a pulsed femtosecond infrared laser source, typically Ti:sapphire mode-locked oscillator. The excitation light first passes through a two-axis galvo-scanning mirror stage and is imaged, using a scan lens and a tube lens, on to the back of the microscope objective. The microscope objective focuses the light to a focal volume typically around 200 nm axial and 1.0 microns lateral (depending upon the numerical aperture of the objective). The excitation volume is on order of a femtoliter ( $10^{-15}$  L). The generated two-photon signal is collected back through the same objective and separated from the excitation light using a dichroic mirror and filter. It is then imaged onto the front of a photomultiplier tube (PMT). In descanned detection, the multiphoton emission is relayed back through the galvo mirrors so that the scanning motion is cancelled out and the emitted light is stationary at the detector. In nondescanned detection, the emission light is separated using a dichroic mirror without passing through the scanning mirrors greatly reducing the loss in signal associated with reflections off of the mirrors and the lenses in the optical path. Because the two-photon emission is not passed back through the scanning mirrors, the emission light on the PMT moves during scanning; however, the PMT is typically insensitive to this motion because of its large detection area. Nondescanned detection is available only for multiphoton imaging because, unlike in single-photon confocal imaging, a pinhole is not required to eliminate out-of-focus light from the image.

**2.3. Advanced Multiphoton Microscopy Techniques.** Fluorescence lifetime imaging microscopy (FLIM) is an additional imaging technique that is better able to distinguish between the different endogenous fluorophores in a biological sample. Due to the broad and overlapping emission spectra of many endogenous fluorophores, it is difficult to quantitatively measure the concentrations of these different species contributing to the autofluorescence emission signal by spectral filtering alone. Fluorescence lifetime can also provide information on the surrounding environment of the fluorophore. FLIM is based on the fact that every fluorophore has a characteristic excited-state lifetime,  $\tau$ , or time for the molecule to decay from the excited electronic state to the ground state. This decay is characterized by a single or multiple exponential (in the case of an inhomogeneous environment) of the form  $P(t) = P_0 \sum_{i=1}^n A_i \exp(-t/\tau_i)$ , where  $P(t)$  is the population in the excited state as a function of time. Here,  $P_0$  is the initial population in the excited state, and  $A_i$  is the normalized amplitude of the exponential component with lifetime  $\tau_i$ . Fluorescence lifetime signal from a biological sample containing multiple fluorophores can become further complicated. For multiple exponential lifetimes, the average lifetime value is sometimes reported, given by  $\bar{\tau} = \sum_{i=1}^n A_i \tau_i$ . This lifetime information can be measured either by

time-domain or frequency-domain methods [20–22]. In the time-domain technique, a pulsed excitation source is used to excite the fluorophore of interest in the biological sample. The subsequent time profile of the fluorescence emission is measured using time gating techniques. Figure 3 illustrates the time-domain FLIM process. In frequency-domain FLIM, an amplitude-modulated excitation source is employed. The lifetime of the fluorophore causes the emitted fluorescence signal to be modulated at the same frequency but with a phase shift relative to the excitation light (see Figure 4). Measurement of this phase offset using phase-sensitive detection (such as a lockin amplifier) will then give the value of the lifetime,  $\tau$ , by the relation  $\tan \phi = \omega \tau$ , where  $\phi$  is the phase offset,  $\omega$  is the modulation frequency. If the lifetime is multiexponential, it is necessary to measure the phase offset at several modulation frequencies in order to obtain the different lifetime components [23]. Some advantages of the frequency-domain technique include faster acquisition compared to the time-domain technique and insensitivity to high photon count rates, which is a problem with time-domain techniques as high count rates can skew the time histogram to shorter times. Frequency-domain FLIM has been recently demonstrated using an inexpensive field-programmable gate array and photon-counting detection giving very rapid and highly sensitive measurements [24].

FLIM has found particular use in imaging NADH/NAD(P)H. Bound and unbound NADH have different characteristic fluorescence lifetimes (free NADH  $\sim 0.3$  ns, protein-bound NADH  $\sim 2$  ns), and therefore FLIM can be used to measure the ratios of these populations giving an indication of metabolic activity and oxidative stress [25–27]. For example, several studies have demonstrated differences in NADH lifetime values between cancerous and normal cells. FLIM is being actively researched for clinical screening of the skin for distinguishing between dysplastic nevi, melanoma, and other dermatological disorders [28–30]. Recently, FLIM was employed to study the cornea using autofluorescence lifetime imaging [31]. In ophthalmological applications, FLIM can be potentially utilized in studying oxidative stress in particular due to interaction of tissue with pharmacological agents or due to disease.

An additional multiphoton imaging technique that is fundamentally different from both fluorescence and harmonic generation is coherent anti-Stokes Raman Spectroscopy (CARS). CARS is a nonlinear version of Raman spectroscopy. In the Raman process, a narrow-band laser illuminates the sample, and a portion of the incident photons are scattered by interactions with molecular vibrations, resulting in a shift to higher (anti-Stokes) or lower frequency (Stokes) photons. The signal intensity is very weak because of the extremely low-scattering cross-section ( $\sim 10^{-30}$  cm<sup>2</sup>/molecule) as opposed to the absorption cross-section of a typical fluorophore ( $\sim 10^{-15}$  cm<sup>2</sup>/molecule).

In contrast to traditional Raman spectroscopy, CARS is a nonlinear optical process that selectively and coherently excites vibrational resonances of biomolecules to rapidly obtain the Raman (vibrational) spectrum. Compared to traditional Raman scattering, the CARS process increases the detection sensitivity by up to  $10^7$  to allow rapid data

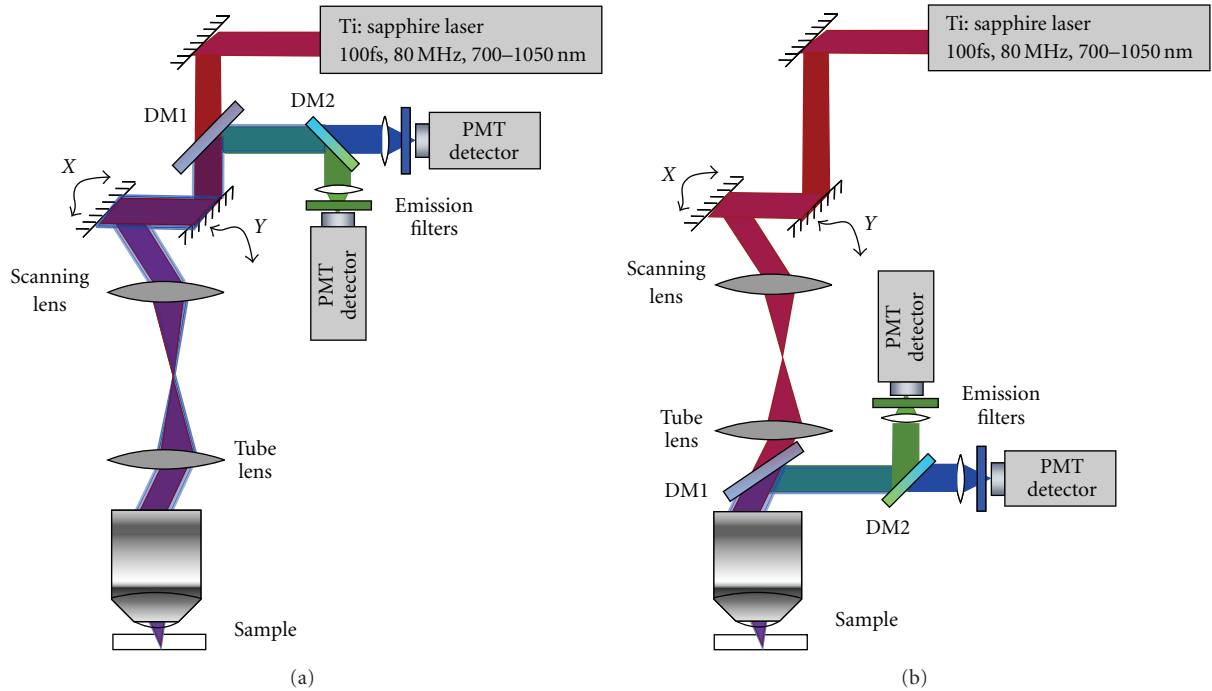


FIGURE 2: Schematic of elements of a multiphoton imaging optical setup. (a) Descanned detection whereby the emitted signal is collected after travelling back through the scanning mirrors. (b) Nondescanned detection. DM indicates dichroic mirror.

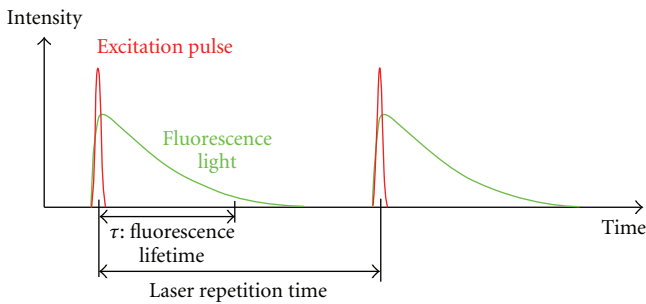


FIGURE 3: Illustration of the fluorescence lifetime principle. The short-pulsed excitation light (red) and the longer time duration fluorescence emission light (green) is shown as a function of time. In FLIM, the time scale of the fluorescence emission,  $\tau$ , is measured.

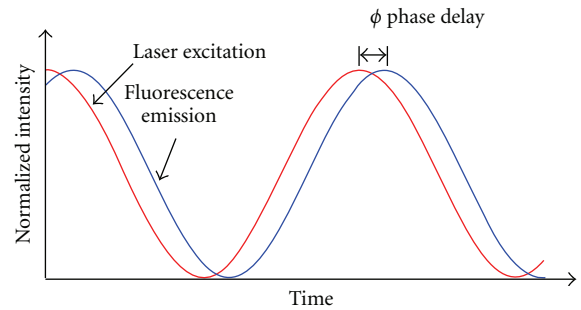


FIGURE 4: Illustration of frequency-domain fluorescence lifetime measurement. The excitation light (red) is modulated in amplitude at a frequency  $\omega$ , while the fluorescence light (blue) is emitted with the same modulation frequency but with a phase shift in time,  $\phi$ . For a single exponential lifetime, the value of the fluorescence lifetime is related by  $\tan \phi = \omega \tau$ .

acquisition [32]. With the associated decrease in measurement times, CARS has been applied in biomedical microscopy to image live cells at video rates without extrinsic fluorescence dye labeling [32–34]. Figure 1 illustrates the CARS process. Two photons (pump and Stokes) excite a specific vibrational resonance coherently. A third photon (probe) subsequently measures the density of the vibrational resonance. The number of emitted anti-Stokes photons that are energy shifted by that vibrational mode is proportional to the square of the density of the vibrational oscillators, thus yielding the molecular concentration of the target [35]. A traditional CARS setup uses two synchronized picosecond lasers or a single picosecond laser with an optical parametric amplifier to generate the two laser beams with different

frequencies matched to one particular vibrational resonance. By tuning the laser frequency difference to a particular vibrational mode, for example,  $2850 \text{ cm}^{-1}$  of the  $\text{CH}_2$  stretch for lipids, chemical-specific imaging can be achieved all without use of endogenous dyes or other labeling techniques. CARS therefore has great potential clinical applications, although it has not yet been applied to imaging in the eye.

**2.4. Microendoscopy.** Due to the limitations in the penetration depth, MPM has so far only been applied in the clinic for screening of the skin [28, 37]. A major step towards extending the applicability of MP imaging for clinically

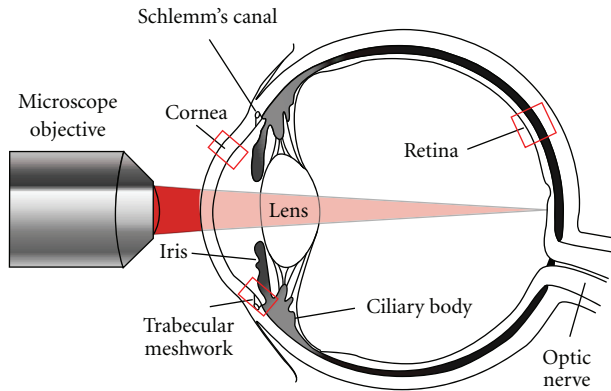


FIGURE 5: Schematic of the eye highlighting the regions of interest for imaging with multiphoton microscopy. Light path for imaging of the retina through the anterior chamber and lens is shown.

relevant applications is the introduction of microendoscopy for intrabody tissue imaging inaccessible to standard bulky optics, [38–43]. Development of microendoscopes or flexible probes for MP imaging can greatly improve the instrumentation for clinical use in ophthalmology. Several demonstrated research applications of microendoscopy include probing of neural activity [39, 40, 44], blood flow measurements [38, 45], and imaging of goblet cells in gastric epithelium [46]. Furthermore, clinical high-resolution microendoscopy has been demonstrated to detect the extracellular matrix proteins collagen and elastin in the human dermis [47, 48]. Imaging of the eye in animal models using a microendoscope has been demonstrated by Wang et al. [18].

The introduction of compound gradient refractive index (GRIN) lenses as focusing optics [44, 49, 50], double-clad photonic crystal fibers [51, 52] for superior detection efficiency and mechanical flexibility, and microelectromechanical systems (MEMS) scanning mirrors [52–54] has been among the most important technological advancements towards microendoscopy. The majority of micro-lenses used in nonlinear imaging, GRIN lenses, have a typical size of 0.2–1 mm in diameter, 1–10 cm in length, and a numerical aperture of less than 0.6. However, due to low numerical aperture and optical aberration, the optical Rayleigh resolution has been limited to  $\sim 1 \mu\text{m}$  in lateral and  $\sim 10 \mu\text{m}$  in axial direction [39, 40]. Recently, aberration-corrected, high-NA planoconvex lenses ( $\text{NA} < 0.85$ ) acting like micro-objectives have been reported to provide on-axis resolution comparable to water-immersion objectives [50]. With further advances, microendoscopy technology can bring the full capabilities of MPM to clinical imaging.

**2.5. Histology.** Another clinical application of MPM is in histology, where there is no requirement for deep tissue penetration as the tissue can easily be sectioned in 10–100  $\mu\text{m}$  thick slices. MPM can have advantages over traditional histological staining techniques by providing more detailed information and highlighting features without perturbing the sample through processing. Preparation of samples for both standard histological staining and electron microscopy

require chemical fixation and dehydration with alcohols. These treatments can cause artifacts and distortions within the tissue due to infusion of fixatives and shrinkage of tissue due to alcohol treatment. In addition, changes to fine tissue morphology can occur with heat infusion of paraffin (for histology) or with polymerization of resin (EM). The application of MPM in histology can be immediately implemented in the clinic and is greatly underutilized. There are opportunities for the development of more accessible MPM systems that would perform imaging on tissue samples with automated analysis routines to aid physicians.

### 3. Multiphoton Imaging of the Eye

**3.1. Comparison of Multiphoton to Current Clinical Imaging Modalities.** Several groups have performed MP imaging of different regions of the eye, *ex vivo*, implicated in a variety of disease pathologies [31, 55–68]. These studies show that MP imaging of the eye for clinical applications has great promise. Current clinical techniques for imaging include optical coherence tomography (OCT) and confocal reflectance microscopy as well as fluorescence imaging. In comparison with MP imaging, OCT imaging has poorer spatial resolution of 2–10  $\mu\text{m}$  lateral and therefore cannot be used to reveal subcellular level structure. While confocal reflectance microscopy does allow subcellular level resolution, its contrast mechanism is due to changes in index of refraction, and therefore it does not have the functional information inherent in MP imaging. Fluorescence imaging uses exogenous dyes to stain the eye in a nonspecific manner typically for looking at the vasculature in the retina. None of these devices are capable of providing functional data for imaged tissues and are thus limited in their ability to direct or influence clinical decision making on a consistent basis.

**3.2. Multiphoton Imaging of Eye Sections.** Figure 5 shows a diagram of the eye highlighting the regions of interest for MPM studies. MP imaging of the cornea is of interest for diagnosis of diseases such as corneal dystrophies and endothelial dysfunction and has been reported by several groups. Steven et al. demonstrated 2PAF, SHG, and autofluorescence lifetime imaging of different ocular surface pathologies on corneal tissue sections using a commercial instrument for clinical MP imaging (DermaInspect, JenLab GmbH, Neuengönna, Germany) [31]. By performing multiple wavelength excitation at 730 nm and 835 nm and resolving different lifetime components by FLIM, they were able to identify and distinguish between epithelial cells, goblet cells, erythrocytes, macrophages, collagen, elastin, vascular structures, and pigmented lesions. Aptel et al. demonstrated SHG, 2PAF, and THG of corneal tissue sections and SHG and 2PAF of the trabecular meshwork. In particular, they demonstrated an additional contrast mechanism by selecting either linear or circularly polarized excitation for THG [55]. Chen et al. demonstrated simultaneous reflectance confocal microscopy, 2PAF, and SHG on corneal sections [56, 57]. Morishige et al. used three-dimensional SHG imaging to characterize structural lamellar organization of the anterior

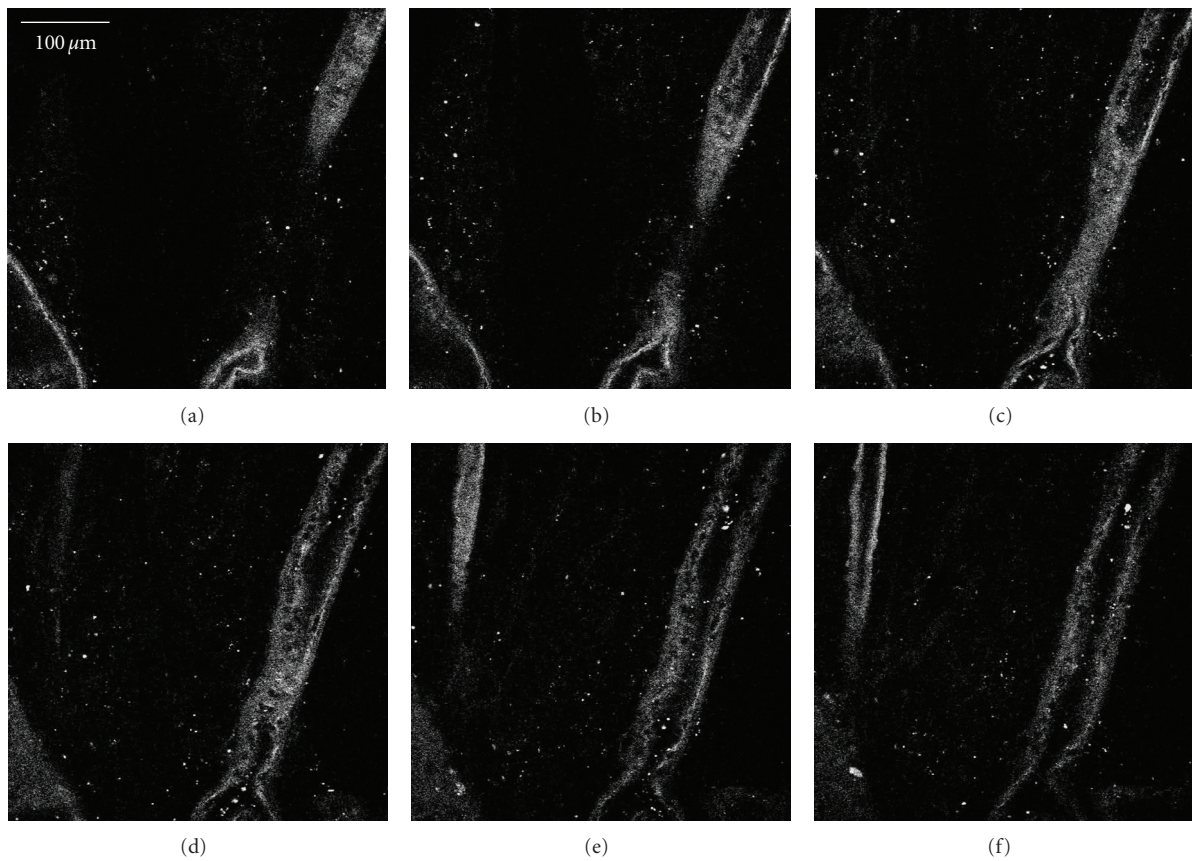


FIGURE 6: Vascular bed of a human retina imaged by second harmonic generation (SHG). Serial  $z$ -sections, spaced  $12\ \mu\text{m}$  apart, of a human retina are shown beginning with (a) through (f). The images shown are collected using the  $800\ \text{nm}$  near infrared laser excitation with a collection window of  $390\text{--}410\ \text{nm}$ . The collagen structure of a large blood vessel is clearly visible through the series, which represents a height of  $60\ \mu\text{m}$ .

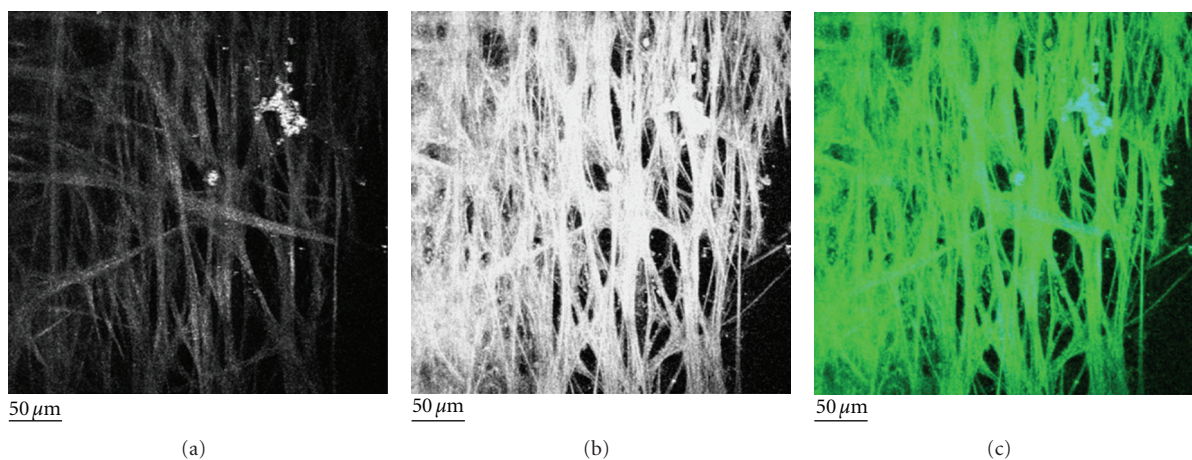


FIGURE 7: Second harmonic generation (SHG) and two-photon autofluorescence (2PAF) of TM region of a human eye from a 73-year-old donor. A section of the eye was flat-mounted with the anterior chamber facing the microscope objective. Images represent a projection of the multiple  $z$ -sections flattened into a single plane. (a) The SHG emission ( $388\ \text{nm}$  to  $409\ \text{nm}$ ) collected from  $800\ \text{nm}$  excitation of TM. (b) The 2PAF emission window ( $452\ \text{nm}$  to  $644\ \text{nm}$ ) collected simultaneously. (c) Merged image of SHG (blue) and AF (green) emission. Black scale bar =  $50\ \mu\text{m}$ . This figure is reprinted from [36].

cornea [58]. Teng et al. demonstrated simultaneous SHG and 2PAF imaging in an intact *ex vivo* porcine eye to identify cellular components of the cornea, limbus, and conjunctiva, as well as imaging corneal and scleral collagen fibers [59]. MP imaging of both cornea and retinal sections was demonstrated by Wang et al. [60, 61].

MP imaging of the retina has also been demonstrated and may find utility in detection of retinal pigment epithelium (RPE) dysfunction and photoreceptor-related dystrophies. To date, no imaging of the human retina has been performed through the anterior chamber, although explants of human retina and RPE have been imaged by the tissue autofluorescence [62–64]. There are additional difficulties in imaging the retina for clinical applications due to the optical constraints posed by the iris that effectively limit the numerical aperture. For example, for an iris opening of 8 mm diameter and typical distance from iris to the retina of 17 mm, the effective numerical aperture, which is indicative of the collection angle of the emitted optical signal, is given by the equation  $NA = n \sin \theta \sim 0.3$ , using the index of refraction of water ( $n = 1.33$ ). The numerical aperture besides limiting the collection efficiency of the emitted signal also limits how tightly the excitation light can be focused, thus determining the achievable resolution of the image. In addition, the aberrations in the lens of the eye can also decrease the obtainable resolution in MP imaging. In order to alleviate this problem, wavefront correction using adaptive optics has been performed for retinal imaging [65, 66].

To our knowledge, MP imaging of a living retina/RPE has only been performed in a rodent eye by imaging through the exterior sclera. In this instance, Imanishi et al. used MPM to view the retina/RPE autofluorescence as well as to localize stores of the visual pigment retinal [67]. The retina itself has no apparent SHG signal, although the overlying retinal vasculature and underlying connective tissue can be imaged via the collagen content. We have demonstrated this in our lab on a Zeiss LSM510 multiphoton confocal microscope, illustrated in Figure 6. In Figure 6(c), one can see the top of the blood vessel followed by the inside of the vessel as the objective moves through the vascular bed. Further optical sectioning past this point yields no further SHG signal.

Recently, we have demonstrated MP imaging of the trabecular meshwork (TM) region of the eye using SHG and 2PAF [68]. Imaging of the TM is important because degeneration of the TM is implicated in glaucoma; therefore, characterizing the cell and collagen structures in the TM may allow early diagnosis, disease monitoring, as well as fundamental studies of the disease mechanism. In our paper, the TM was flat-mounted and visually sectioned by  $0.5 \mu\text{m}$  intervals to a depth of  $50 \mu\text{m}$  and then computer modeled into a single-plane projection (Figure 7). SHG and 2PAF emission windows were collected using the META spectral detector on a Zeiss LSM510 multiphoton confocal system. Figures 7(a) and 7(b) show the SHG and 2PAF fluorescence, respectively. Although the SHG signal is comparatively weaker than the 2PAF, these two signals are qualitatively the same when overlapped in Figure 7(c) (blue = SHG, green = 2PAF). Since collagen is the most common noncentrosymmetric macromolecule in the TM, the SHG signal is highly

suggestive of the fact that the structures seen by 2PAF are in fact collagen fibers. In these images, the majority of collagen fibers of the TM appear as smooth bundles of between 10 and  $20 \mu\text{m}$ , although the occasional  $\sim 1 \mu\text{m}$  collagen fiber is visible. These bundles have a fairly consistent diameter over short distances but over longer distances ( $>250 \mu\text{m}$ ) commonly split or join other bundles. The end result is a meshwork of collagen interwoven with varying-sized regions of nonfluorescent signal, which we assume to be fluid spaces.

**3.3. Transscleral Imaging.** Issues for MPM use in the clinic include accessibility of the different regions of the eye to optical light. Imaging of the trabecular meshwork using MPM would be of great clinical value in particular for early disease diagnosis and monitoring of glaucoma. However, in order to access this region, it would be necessary to image through approximately 600 microns of scleral tissue. For transscleral imaging, in general, only the surface of the sclera can be imaged as the highly scattering scleral tissue greatly limits optical light transmission. Vogel et al. measured the optical properties of human sclera using an integrating sphere. They found a transmission of 6% at 442 nm, 35% at 804 nm, and 53% at 1064 nm [69]. Although the excitation light for MPM ranging from 800 to 1000 nm can likely penetrate the sclera, the shorter wavelength SHG and autofluorescence emission will be greatly reduced upon collection in the epidirection. We continue to research this known limitation of MPM for TM imaging and believe that future advances will lead to greater clinical applicability of this technology.

**3.4. Power and Wavelength Requirements for In Vivo Imaging.** One of the advantages of MPM is the ability to use infrared light illumination, which is much less phototoxic for the eye than visible light. One issue with this technique for clinical use is potential thermal mechanical damage to the tissue during imaging due to absorption of the laser energy and local heating effects. Several studies have shown that the thermal damage due to two-photon absorption in most tissue under imaging conditions is negligible [70]. However, there are potential damage issues associated with pigmented tissue such as those found in the skin or the retina. There are methods to mitigate this including reducing the repetition rate of the laser to allow for thermal diffusion between pulses on the same location in the tissue [71, 72]. The pulse duration of the laser can also have a great impact on thermal damage. Du et al. found a reduction in tissue damage threshold with pulse duration for the same total energy delivered to the tissue sample [73]. The differences in laser system parameters combined with differences in tissue type suggest that, before any clinical use of MPM, photodamage issues must be carefully characterized.

**3.5. Drug Delivery Monitoring.** Finally, one exciting future application of MPM is in monitoring drug delivery *in vivo*. Kek et al. applied two-photon microscopy to monitor the transscleral delivery of tazarotenic acid using its intrinsic fluorescence at 500 nm [74]. The emerging technique of

stimulated Raman scattering (SRS) a similar multiphoton technique to CARS imaging also has great potential for drug delivery monitoring because of its specificity; that is, the generated signal is specific to a single chemical compound, as well as the linear dependence of the signal on concentration [75]. SRS has currently been applied to monitor penetration of dimethyl sulfoxide (DMSO), a skin-penetration enhancer and retinoic acid in the upper dermal layer. There are many opportunities for applying SRS to monitoring drug delivery in the eye due to the transparency of the tissue making deeper penetration depths possible as compared to the skin.

#### 4. Conclusion and Future Prospects

Current imaging techniques, such as ultrasound and OCT, have greatly influenced the standards of clinical and surgical ophthalmic care. Physicians can now detect disease using very sensitive imaging modalities and can also follow the progression of disease, thus shedding light on the efficacy of applied interventions. While availability of fine structural information is increasingly available in the clinical setting, the actual function of the imaged structures remains unknown. MPM offers the potential for obtaining both structural and functional data on a wide range of ophthalmic tissues. For example, it may be possible to image the trabecular meshwork structure while also establishing the metabolism of individual trabecular meshwork cells by quantifying NAD(P)H concentrations in real time. Such information could lead to earlier and more precise disease detection, while also allowing for more insight into the effects of therapeutic interventions aimed at preserving vision.

Future applicability of MPM in practice will require further advances in the ability to penetrate past tissues, such as sclera, that have high scattering properties. The safety of using MPM also requires further studies since some ocular tissues have high melanin content which may lead to greater energy absorption and related tissue damage. Another obstacle that will need to be addressed is the difficulty in obtaining data across the relatively long axial length distance noted between the surface of the cornea and the posterior pole. Fortunately, advances in MPM continue to develop at a rapid pace, and obstacles that existed in the past have been overcome with continued research. With continued advances, the application of MPM in ophthalmic practice promises to yield valuable clinical information that will ultimately result in improved patient care, which is the common goal of researchers and physicians alike.

#### References

- [1] S. H. Kang, S. W. Hong, S. K. Im, S. H. Lee, and M. D. Ahn, "Effect of myopia on the thickness of the retinal nerve fiber layer measured by Cirrus HD optical coherence tomography," *Investigative Ophthalmology & Visual Science*, vol. 51, no. 8, pp. 4075–4083, 2010.
- [2] P. T. C. So, C. Y. Dong, B. R. Masters, and K. M. Berland, "Two-photon excitation fluorescence microscopy," *Annual Review of Biomedical Engineering*, vol. 2, no. 2000, pp. 399–429, 2000.
- [3] K. König, "Multiphoton microscopy in life sciences," *Journal of Microscopy*, vol. 200, no. 2, pp. 83–104, 2000.
- [4] F. Helmchen and W. Denk, "Deep tissue two-photon microscopy," *Nature Methods*, vol. 2, no. 12, pp. 932–940, 2005.
- [5] J. Squier and M. Müller, "High resolution nonlinear microscopy: a review of sources and methods for achieving optimal imaging," *Review of Scientific Instruments*, vol. 72, no. 7, pp. 2855–2867, 2001.
- [6] W. R. Zipfel, R. M. Williams, and W. W. Webb, "Nonlinear magic: multiphoton microscopy in the biosciences," *Nature Biotechnology*, vol. 21, no. 11, pp. 1369–1377, 2003.
- [7] B. R. Masters and P. T. C. So, *Handbook of Biomedical Nonlinear Optical Microscopy*, Oxford University Press, Oxford, UK, 2008.
- [8] W. Denk, J. H. Strickler, and W. W. Webb, "Two-photon laser scanning fluorescence microscopy," *Science*, vol. 248, no. 4951, pp. 73–76, 1990.
- [9] P. Theer, M. T. Hasan, and W. Denk, "Two-photon imaging to a depth of 1000  $\mu\text{m}$  in living brains by use of a Ti:Al<sub>2</sub>O<sub>3</sub> regenerative amplifier," *Optics Letters*, vol. 28, no. 12, pp. 1022–1024, 2003.
- [10] P. N. Marsh, D. Burns, and J. M. Girkin, "Practical implementation of adaptive optics in multiphoton microscopy," *Optics Express*, vol. 11, no. 10, pp. 1123–1130, 2003.
- [11] M. A. A. Neil, R. Juškaitis, M. J. Booth, T. Wilson, T. Tanaka, and S. Kawata, "Adaptive aberration correction in a two-photon microscope," *Journal of Microscopy*, vol. 200, no. 2, pp. 105–108, 2000.
- [12] M. Rueckel, J. A. Mack-Bucher, and W. Denk, "Adaptive wavefront correction in two-photon microscopy using coherence-gated wavefront sensing," *Proceedings of the National Academy of Sciences of the United States of America*, vol. 103, no. 46, pp. 17137–17142, 2006.
- [13] M. Müller, J. Squier, K. R. Wilson, and G. J. Brakenhoff, "3D microscopy of transparent objects using third-harmonic generation," *Journal of Microscopy*, vol. 191, no. 3, pp. 266–274, 1998.
- [14] D. Débarre, W. Supatto, A.-M. Pena et al., "Imaging lipid bodies in cells and tissues using third-harmonic generation microscopy," *Nature Methods*, vol. 3, no. 1, pp. 47–53, 2006.
- [15] W. R. Zipfel, R. M. Williams, R. Christiet, A. Y. Nikitin, B. T. Hyman, and W. W. Webb, "Live tissue intrinsic emission microscopy using multiphoton-excited native fluorescence and second harmonic generation," *Proceedings of the National Academy of Sciences of the United States of America*, vol. 100, no. 12, pp. 7075–7080, 2003.
- [16] S. Huang, A. A. Heikal, and W. W. Webb, "Two-photon fluorescence spectroscopy and microscopy of NAD(P)H and flavoprotein," *Biophysical Journal*, vol. 82, no. 5, pp. 2811–2825, 2002.
- [17] K. König, K. Schenke-Layland, I. Riemann, and U. A. Stock, "Multiphoton autofluorescence imaging of intratissue elastic fibers," *Biomaterials*, vol. 26, no. 5, pp. 495–500, 2005.
- [18] B.-G. Wang, K. König, and K.-J. Halbhauer, "Two-photon microscopy of deep intravital tissues and its merits in clinical research," *Journal of Microscopy*, vol. 238, no. 1, pp. 1–20, 2010.
- [19] R. R. Alfano and A. Katz, "Non invasive fluorescence-based instrumentation for cancer and precancer detection and screening," in *In-Vitro Diagnostic Instrumentation*, Proceedings of SPIE, pp. 223–226, January 2000.
- [20] T. French, P. T. C. So, C. Y. Dong, K. M. Berland, and E. Gratton, "Fluorescence lifetime imaging techniques for

- microscopy,” *Methods in Cell Biology*, no. 56, pp. 277–304, 1998.
- [21] E. Gratton, S. Breusegem, J. Sutin, Q. Ruan, and N. Barry, “Fluorescence lifetime imaging for the two-photon microscope: time-domain and frequency-domain methods,” *Journal of Biomedical Optics*, vol. 8, no. 3, pp. 381–390, 2003.
- [22] J. Lakowicz, *Principles of Fluorescence Spectroscopy*, Springer, New York, NY, USA, 2006.
- [23] J. R. Lakowicz, “Frequency-domain lifetime measurements,” in *Principles of Fluorescence Spectroscopy*, pp. 157–204, Springer, New York, NY, USA, 2006.
- [24] R. A. Colyer, C. Lee, and E. Gratton, “A novel fluorescence lifetime imaging system that optimizes photon efficiency,” *Microscopy Research and Technique*, vol. 71, no. 3, pp. 201–213, 2008.
- [25] Q. Yu and A. A. Heikal, “Two-photon autofluorescence dynamics imaging reveals sensitivity of intracellular NADH concentration and conformation to cell physiology at the single-cell level,” *Journal of Photochemistry and Photobiology B: Biology*, vol. 95, no. 1, pp. 46–57, 2009.
- [26] J. R. Lakowicz, H. Szmajcinski, K. Nowaczyk, and M. L. Johnson, “Fluorescence lifetime imaging of free and protein-bound NADH,” *Proceedings of the National Academy of Sciences of the United States of America*, vol. 89, no. 4, pp. 1271–1275, 1992.
- [27] D. K. Bird, L. Yan, K. M. Vrotsos et al., “Metabolic mapping of MCF10A human breast cells via multiphoton fluorescence lifetime imaging of the coenzyme NADH,” *Cancer Research*, vol. 65, no. 19, pp. 8766–8773, 2005.
- [28] K. König, “Clinical multiphoton tomography,” *Journal of biophotonics*, vol. 1, no. 1, pp. 13–23, 2008.
- [29] P. A. A. De Beule, C. Dunsby, N. P. Galletly et al., “A hyperspectral fluorescence lifetime probe for skin cancer diagnosis,” *Review of Scientific Instruments*, vol. 78, no. 12, Article ID 123101, 2007.
- [30] K. König and I. Riemann, “High-resolution multiphoton tomography of human skin with subcellular spatial resolution and picosecond time resolution,” *Journal of Biomedical Optics*, vol. 8, no. 3, pp. 432–439, 2003.
- [31] P. Steven, M. Müller, N. Koop, C. Rose, and G. Hüttmann, “Comparison of Cornea Module and DermaInspect for noninvasive imaging of ocular surface pathologies,” *Journal of biomedical optics*, vol. 14, no. 6, Article ID 064040, 2009.
- [32] C. L. Evans and X. S. Xie, “Coherent anti-Stokes Raman scattering microscopy: chemical imaging for biology and medicine,” *Annual Review of Analytical Chemistry*, vol. 1, no. 1, pp. 883–909, 2008.
- [33] C. L. Evans, E. O. Potma, M. Puoris’haag, D. Côté, C. P. Lin, and X. S. Xie, “Chemical imaging of tissue in vivo with video-rate coherent anti-Stokes Raman scattering microscopy,” *Proceedings of the National Academy of Sciences of the United States of America*, vol. 102, no. 46, pp. 16807–16812, 2005.
- [34] A. Zumbusch, G. R. Holtom, and X. S. Xie, “Three-dimensional vibrational imaging by coherent anti-Stokes Raman scattering,” *Physical Review Letters*, vol. 82, no. 20, pp. 4142–4145, 1999.
- [35] J.-X. Cheng, A. Volkmer, L. D. Book, and X. S. Xie, “Epi-detected coherent anti-stokes Raman scattering (E-CARS) microscope with high spectral resolution and high sensitivity,” *Journal of Physical Chemistry B*, vol. 105, no. 7, pp. 1277–1280, 2001.
- [36] D. A. Ammar, T. C. Lei, E. A. Gibson, and M. Y. Kahook, “Two-photon imaging of the trabecular meshwork,” *Molecular Vision*, vol. 16, pp. 935–944, 2010.
- [37] K. König, M. Speicher, R. Bückle et al., “Clinical optical coherence tomography combined with multiphoton tomography of patients with skin diseases,” *Journal of Biophotonics*, vol. 2, no. 6-7, pp. 389–397, 2009.
- [38] F. Helmchen, M. S. Fee, D. W. Tank, and W. Denk, “A miniature head-mounted two-photon microscope: high-resolution brain imaging in freely moving animals,” *Neuron*, vol. 31, no. 6, pp. 903–912, 2001.
- [39] J. C. Jung, A. D. Mehta, E. Aksay, R. Stepnoski, and M. J. Schnitzer, “In vivo mammalian brain imaging using one- and two-photon fluorescence microendoscopy,” *Journal of Neurophysiology*, vol. 92, no. 5, pp. 3121–3133, 2004.
- [40] M. J. Levene, D. A. Dombeck, K. A. Kasischke, R. P. Molloy, and W. W. Webb, “In vivo multiphoton microscopy of deep brain tissue,” *Journal of Neurophysiology*, vol. 91, no. 4, pp. 1908–1912, 2004.
- [41] H. Bao, A. Boussioutas, R. Jeremy, S. Russell, and M. Gu, “Second harmonic generation imaging via nonlinear endomicroscopy,” *Optics Express*, vol. 18, no. 2, pp. 1255–1260, 2010.
- [42] D. Bird and M. Gu, “Two-photon fluorescence endoscopy with a micro-optic scanning head,” *Optics Letters*, vol. 28, no. 17, pp. 1552–1554, 2003.
- [43] F. Légaré, C. L. Evans, F. Ganikhanov, and X. S. Xie, “Towards CARS endoscopy,” *Optics Express*, vol. 14, no. 10, pp. 4427–4432, 2006.
- [44] J. C. Jung and M. J. Schnitzer, “Multiphoton endoscopy,” *Optics Letters*, vol. 28, no. 11, pp. 902–904, 2003.
- [45] B. A. Flusberg, J. C. Jung, E. D. Cocker, E. P. Anderson, and M. J. Schnitzer, “In vivo brain imaging using a portable 3.9 gram two-photon fluorescence microendoscope,” *Optics Letters*, vol. 30, no. 17, pp. 2272–2274, 2005.
- [46] H. Bao, A. Boussioutas, J. Reynolds, S. Russell, and M. Gu, “Imaging of goblet cells as a marker for intestinal metaplasia of the stomach by one-photon and two-photon fluorescence endomicroscopy,” *Journal of biomedical optics*, vol. 14, no. 6, Article ID 064031, 2009.
- [47] K. König, M. Weinigel, D. Hoppert et al., “Multiphoton tissue imaging using high-NA microendoscopes and flexible scan heads for clinical studies and small animal research,” *Journal of biophotonics*, vol. 1, no. 6, pp. 506–513, 2008.
- [48] K. König, A. Ehlers, I. Riemann, S. Schenkl, R. Bückle, and M. Kaatz, “Clinical two-photon microendoscopy,” *Microscopy Research and Technique*, vol. 70, no. 5, pp. 398–402, 2007.
- [49] W. Göbel, J. N. D. Kerr, A. Nimmerjahn, and F. Helmchen, “Miniaturized two-photon microscope based on a flexible coherent fiber bundle and a gradient-index lens objective,” *Optics Letters*, vol. 29, no. 21, pp. 2521–2523, 2004.
- [50] R. P. J. Barretto, B. Messerschmidt, and M. J. Schnitzer, “In vivo fluorescence imaging with high-resolution microlenses,” *Nature Methods*, vol. 6, no. 7, pp. 511–512, 2009.
- [51] L. Fu, X. Gan, and M. Gu, “Nonlinear optical microscopy based on double-clad photonic crystal fibers,” *Optics Express*, vol. 13, no. 14, pp. 5528–5534, 2005.
- [52] L. Fu, A. Jain, H. Xie, C. Cranfield, and M. Gu, “Nonlinear optical endoscopy based on a double-clad photonic crystal fiber and a MEMS mirror,” *Optics Express*, vol. 14, no. 3, pp. 1027–1032, 2006.
- [53] L. Fu, A. Jain, C. Cranfield, H. Xie, and M. Gu, “Three-dimensional nonlinear optical endoscopy,” *Journal of Biomedical Optics*, vol. 12, no. 4, Article ID 040501, 2007.
- [54] W. Piyawattanametha, R. P. J. Barretto, T. H. Ko et al., “Fast-scanning two-photon fluorescence imaging based on a microelectromechanical systems two-dimensional scanning mirror,” *Optics Letters*, vol. 31, no. 13, pp. 2018–2020, 2006.

- [55] F. Aptel, N. Olivier, A. Deniset-Besseau et al., "Multimodal nonlinear imaging of the human cornea," *Investigative Ophthalmology & Visual Science*, vol. 51, no. 5, pp. 2459–2465, 2010.
- [56] W. L. Chen, C. K. Chou, M. G. Lin et al., "Single-wavelength reflected confocal and multiphoton microscopy for tissue imaging," *Journal of Biomedical Optics*, vol. 14, no. 5, Article ID 054026, 2009.
- [57] W.-L. Chen, Y. Sun, W. Lo, H.-Y. Tan, and C.-Y. Dong, "Combination of multiphoton and reflective confocal imaging of cornea," *Microscopy Research and Technique*, vol. 71, no. 2, pp. 83–85, 2008.
- [58] N. Morishige, A. J. Wahlert, M. C. Kenney et al., "Second-harmonic imaging microscopy of normal human and keratoconus cornea," *Investigative Ophthalmology and Visual Science*, vol. 48, no. 3, pp. 1087–1094, 2007.
- [59] S.-W. Teng, H.-Y. Tan, J.-L. Peng et al., "Multiphoton autofluorescence and second-harmonic generation imaging of the ex vivo porcine eye," *Investigative Ophthalmology and Visual Science*, vol. 47, no. 3, pp. 1216–1224, 2006.
- [60] B.-G. Wang, A. Eitner, J. Lindenau, and K.-J. Halbhauer, "High-resolution two-photon excitation microscopy of ocular tissues in porcine eye," *Lasers in Surgery and Medicine*, vol. 40, no. 4, pp. 247–256, 2008.
- [61] B.-G. Wang, K. Koenig, I. Riemann, R. Krieg, and K.-J. Halbhauer, "Intraocular multiphoton microscopy with subcellular spatial resolution by infrared femtosecond lasers," *Histochemistry and Cell Biology*, vol. 126, no. 4, pp. 507–515, 2006.
- [62] A. Bindewald-Wittich, M. Han, S. Schmitz-Valckenberg et al., "Two-photon-excited fluorescence imaging of human RPE cells with a femtosecond Ti:sapphire laser," *Investigative Ophthalmology and Visual Science*, vol. 47, no. 10, pp. 4553–4557, 2006.
- [63] M. Han, G. Giese, S. Schmitz-Valckenberg et al., "Age-related structural abnormalities in the human retina-choroid complex revealed by two-photon excited autofluorescence imaging," *Journal of Biomedical Optics*, vol. 12, no. 2, Article ID 024012, 2007.
- [64] M. Han, A. Bindewald-Wittich, F. G. Holz et al., "Two-photon excited autofluorescence imaging of human retinal pigment epithelial cells," *Journal of Biomedical Optics*, vol. 11, no. 1, Article ID 010501, 2006.
- [65] E. J. Gualda, J. M. Bueno, and P. Artal, "Wavefront optimized nonlinear microscopy of ex vivo human retinas," *Journal of biomedical optics*, vol. 15, no. 2, Article ID 026007, 2010.
- [66] S. A. Burns, R. Tumber, A. E. Elsner, D. Ferguson, and D. X. Hammer, "Large-field-of-view, modular, stabilized adaptive-optics-based scanning laser ophthalmoscope," *Journal of the Optical Society of America A: Optics and Image Science, and Vision*, vol. 24, no. 5, pp. 1313–1326, 2007.
- [67] Y. Imanishi, M. L. Batten, D. W. Piston, W. Baehr, and K. Palczewski, "Noninvasive two-photon imaging reveals retinyl ester storage structures in the eye," *Journal of Cell Biology*, vol. 164, no. 3, pp. 373–383, 2004.
- [68] D. A. Ammar, T. C. Lei, E. A. Gibson, and M. Y. Kahook, "Two-photon imaging of the trabecular meshwork," *Molecular Vision*, vol. 16, pp. 935–944, 2010.
- [69] A. Vogel, C. Dlugos, R. Nuffer, and R. Birngruber, "Optical properties of human sclera, and their consequences for transscleral laser applications," *Lasers in Surgery and Medicine*, vol. 11, no. 4, pp. 331–340, 1991.
- [70] A. Hopt and E. Neher, "Highly nonlinear photodamage in two-photon fluorescence microscopy," *Biophysical Journal*, vol. 80, no. 4, pp. 2029–2036, 2001.
- [71] B. R. Masters, P. T. C. So, C. Buehler et al., "Mitigating thermal mechanical damage potential during two-photon dermal imaging," *Journal of Biomedical Optics*, vol. 9, no. 6, pp. 1265–1270, 2004.
- [72] W. Denk, D. Piston, and W. W. Webb, "Two-photon molecular excitation laser-scanning microscopy," in *Handbook of Biological Confocal Microscopy*, J. B. Pawley, Ed., pp. 535–549, Springer, New York, NY, USA, 2006.
- [73] D. Du et al., *Damage Threshold as a Function of Pulse Duration in Biological Tissue*, vol. 60 of *Springer Series in Chemical Physics*, Springer, New York, NY, USA, 1995.
- [74] W. K. Kek et al., "wo-photon fluorescence excitation microscopy to assess trans-scleral diffusional pathways in an isolated perfused bovine eye model," *Investigative Ophthalmology and Visual Science*. In press.
- [75] C. W. Freudiger, W. Min, B. G. Saar et al., "Label-free biomedical imaging with high sensitivity by stimulated raman scattering microscopy," *Science*, vol. 322, no. 5909, pp. 1857–1861, 2008.